The Dissertation Committee for Scott M. Whitney Certifies that this is the approved version of the following dissertation:

NEUTRON DEPTH PROFILING BENCHMARKING AND ANALYSIS OF APPLICATIONS TO LITHIUM ION CELL ELECTRODE AND INTERFACIAL STUDIES RESEARCH

Committee:

Steve Biegalski, Supervisor

Robert G. Downing

Sheldon Landsberger

Donna O'Kelly

Erich Schneider

NEUTRON DEPTH PROFILING BENCHMARKING AND ANALYSIS OF APPLICATIONS TO LITHIUM ION CELL ELECTRODE AND INTERFACIAL STUDIES RESEARCH

by

Scott M. Whitney, B.S.; M.S.E.

Dissertation

Presented to the Faculty of the Graduate School of

The University of Texas at Austin

in Partial Fulfillment

of the Requirements

for the Degree of

Doctor of Philosophy

The University of Texas at Austin

May 2008

Dedication

In memory of my grandfather. A veteran, a father… an inspiration of a man.

Acknowledgements

Above all, I want to first acknowledge the entire faculty and staff of the Nuclear Engineering Teaching Lab. Every piece of innovation and science coming out of NETL is a result of the support and effort given by each person in that building. Whether it be operating the reactor, health physics, or helping somebody find a wrench; there is always somebody there willing to help. This includes Dr. Steve Biegalski, Dr. Sheldon Landsberger, Dr. Erich Schneider, Dr. Donna O'Kelly, and Sean O'Kelly. These people lead the way for the science of NETL that would otherwise grind to a halt if not for the insight and wisdom that each one of them brings to the table.

Also, I will not forget the long days and hard work of Mike Krause and Larry Welch, without whom I could never have completed this research. Besides maintaining and operating the reactor, these two men have seemingly endless knowledge of electrical and mechanical systems that was invaluable to me throughout my research. Many mysteries of mine were solved rather quickly by a quick call to the control room where Mike and Larry sat ready with their experience to fix my own mistakes.

For myself, perhaps the most influential member of my graduate research is my supervisor, Dr. Steve Biegalski. Through his guidance and support, Steve is responsible for the large majority of my experimental prowess that was gained here at NETL. He has been an advisor and friend throughout my entire graduate term in the nuclear graduate program and has taken me through the ups and downs of both computational and experimental nuclear science. I am grateful for the independence that I was allowed here

at NETL, but more importantly, that I had an advisor's wisdom to fall back on when it was needed (and it was needed).

Wisdom could not be mentioned without also mentioning two very important men to this research, Dr. Robert Greg Downing and Dr. John B. Goodenough. They are both men of a million ideas, who still somehow maintain a kindness and modesty about them that make them approachable with any conceivable question. Greg Downing has been the best teacher of Neutron Depth Profiling that I could have asked for. His experience in so many fields of science has brandished him with not only the knowledge, but also the ability to answer every silly question that I put forth to him. I am grateful to Greg for the countless responses to my e-mails and for his time given to me, but primarily for being a teacher to me about a technique that not many could teach. I am also thankful to Greg for allowing me to use his facility at NIST, the data and experience that I gained from my short time there was priceless to this research.

John B. Goodenough and his post-doc, Dr. Yunhui Huang, are a major reason that this research could even be completed. I set out to perform this research without knowing where to get all of the pieces to the puzzle, but Dr. Goodenough and Yunhui were there to fill in the blanks. Both are men of great character and graciousness, and I thank them for teaching me and collaborating with me to help bring together two very important areas of science. I also would like to thank Dr. Goodenough for allowing me to use his lab and his post-doc's time without asking anything more than the pursuit of new science.

I should also mention my peers at NETL. These guys were helpful in too many ways to count, from the sharing of ideas and problem solving, to just taking it easy and letting some of the stress disappear. I would find it hard to believe that anybody has completed such lengthy research as ours without getting some insight from simple

conversations with their friends. And for that insight, the least I can do is give my friends their due credit here.

Finally I would like to acknowledge the support of the DOE INIE program and Sean O'Kelly for their continued support of my research throughout the years. We all know that research takes money, and without INIE or Sean I could not have completed this research. I am grateful to Sean for being there to answer my questions, and also to support my research and trusting the decisions I made for our NDP facility.

NEUTRON DEPTH PROFILING BENCHMARKING AND ANALYSIS OF APPLICATIONS TO LITHIUM ION CELL ELECTRODE AND INTERFACIAL STUDIES RESEARCH

Publication No._____

Scott M. Whitney, Ph.D.

The University of Texas at Austin, 2008

Supervisor: Steve Biegalski

The role of the lithium ion cell is increasing with great intensity due to global concerns for the decreased use of fossil fuels as well as the growing popularity of portable electronics. With the dramatic increase in demand for these cells follows an outbreak of research to optimize the lithium ion cells in terms of safety, cost, and also performance. The work shown in this dissertation sets out to distinguish the role of Neutron Depth Profiling (NDP) in the expanding research of lithium ion cells.

Lithium ions play the primary role in the performance of lithium ion batteries. Moving from anode to cathode, and cathode to anode, the lithium ions are constantly being disturbed during the cell's operation. The ability to accurately determine the lithium's behavior within the electrodes of the cell after different operating conditions is a powerful tool to better understand the faults and advantages of particular electrode compositions and cell designs. NDP has this ability through the profiling of ^{6}Li.

This research first validates the ability of The University of Texas NDP (UT-NDP) facility to accurately profile operated lithium ion cell electrodes to a precision within 2% over 10 μm for concentration values, and with a precision for depth measurements within 77 nm. The validation of the UT-NDP system is performed by comparing UT-NDP profiles to those from the NIST-NDP system, from the Secondary Ion Mass Spectrometry (SIMS) technique, and also from Monte Carlo n-Particle (MCNPX) code simulations. All of the comparisons confirmed that the UT-NDP facility is fully capable of providing accurate depth profiles of lithium ion cell electrodes in terms of depth, shape of distribution, and concentration.

Following the validation studies, this research investigates three different areas of lithium ion cell research and provides analysis based on NDP results. The three areas of investigation include storage of cells at temperature, cycling of cells, and the charging of cells at different current rates. The results conclude that NDP is a valuable asset to the characterization of the Solid Electrolyte Interface (SEI) growth as a function of storage time. The NDP results were able to conclude that $LiFePO_4$ cell anodes have a factor of 21 times slower rate of SEI growth than anodes from $LiFePSO_4$. This indicates that the capacity fade of the $LiFePO_4$ cell will be less than that of the $LiFePSO_4$ cell due to storage at 50ºC.

Furthermore, NDP was able to conclude that cycling of cells had little effect on the lithium concentration within the cathode materials. The lithium concentration was found to be uniform throughout the first 10 μm of the $LiFePO_4$ and $LiNi_{1/3}Mn_{1/3}Co_{1/3}O_2$ cathodes. These measurements agreed with the initial hypothesis. However, NDP analysis of cells charged at different current rates found that lithium was concentrating within the first 2 μm of the cathode's surface at the electrode-electrolyte interface. This

was an unexpected conclusion, but the results also concluded that effect of the lithium concentrating near the surface is amplified by charging the cells at higher current rates.

The ultimate conclusion of this research was that NDP is capable of providing invaluable insight to the behavior of lithium within the electrodes of lithium ion cells. It is the author's conclusion that NDP may be most useful in the investigation of SEI layers and their variation according to electrode composition, electrolyte compositions, and the conditions, such as temperature, to which the cells are exposed.

Table of Contents

List of Tables

List of Figures

Chapter 1: Introduction

The rapid rise of portable electronics along with the global call for more environmentally friendly vehicles has resulted in expansive research into rechargeable, highly portable and dependable batteries. The front-runner in this research is the lithium ion cell, which has proven itself to be invaluable in terms of performance, cost, and safety. The common $LiCoO_2$ cell has claimed the largest portion of the market, but due to new performance needs and safety concerns, the electrochemical community is testing new cathode compositions, and seeking new ways to gain deeper insight into the cell's kinetics.

The active role played by the Li^+ ion in electrochemical cells suggests that Neutron Depth Profiling (NDP) can have powerful implications by determining accurate lithium distribution profiles within cell electrodes with concentration uncertainties below 3.22% and depth resolution ranging from 80 nm to 500 nm. However, the utility of NDP towards this aspect of electrochemical research has been limited to thin-film research and electrochromic materials [1, 2]. NDP of lithium ion cells has likely been limited primarily due to the lack of electrochemists' knowledge of the technique. Another factor may also be that an extensive study to confirm the validity of NDP analysis on electrodes from actual cells (*i.e.* those that have been operated and disassembled) has not been conducted.

Cell electrodes are often analyzed by various techniques including focused ion beam (FIB), scanning electron microscopy (SEM), and X-ray photoelectron spectroscopy (XPS) to name a few (max depth ~100 Å). Generally this analysis focuses on oxidation states of electrode ions, passivation layer thickness, chemical structure, and so on. The analysis of the latter cell characteristics are often performed according to variant charge/discharge methods [3], storage time [4], and charging cycles. However, the above techniques are limited to a much more shallow depth, in the range of nanometers, than is

NDP. With such limitations, it is impossible for these techniques to offer significant information about the lithium distribution within electrode samples that are typically in the range of 30 to 100 μm thick.

The ability to profile lithium distributions within cathodes and anodes of lithium cells up to several microns deep from the electrode-electrolyte interface would enable research into several areas of electrochemical cell research. These include the diffusive behavior of ions within various electrode matrices as well as the variability of the solid electrolyte interface formed on electrodes.

LITERATURE REVIEW

A general overview of the most relevant papers to this research is contained within this section. There are more than 100 papers on the subject of NDP which Downing *et al.* from NIST has compiled in a review manuscript [5]. The corresponding number of papers for lithium ion cell research is much larger, and so only the most important literature to this project will be discussed.

Neutron Depth Profiling

NDP is an analytical technique with publications beginning as early as 1972. Ziegler *et al.* introduced the technique [6] at the time as a way to determine the boron impurity concentration in silicon wafers by neutron bombardment of the sample and analysis of the alpha energies that are emitted. Ziegler wanted to address the problem of accurately determining boron concentrations in silicon by a method other than the typical electrical measurements of the day. The NDP technique that they developed had the ability to profile boron in a material to a depth of a few μm with a resolution of 20 nm. The group's paper introduced the general experimental method that is still adhered to today.

Muller, Henkellmann, and Boroffka introduced the use of silicon surface barrier detector rather than a uniquely designed detector that Ziegler used. They published a paper in 1975 [7] describing their newly developed NDP facility at the high-flux reactor in Grenoble. Having the highest neutron flux of the day the team was able to profile boron concentrations as low as 10^{12} atoms cm^{-2} with a depth resolution of 25 nm. This choice of detector was significant in showing that surface barrier detectors may be utilized for this technique with accuracy. This use of a silicon surface barrier detector is the general standard for NDP systems today and is used at The University of Texas at Austin NDP facility (UT-NDP).

The first to move beyond boron measurements were Biersack and Fink [8]. They extended Ziegler's idea to other light isotopes besides ^{10}B, such as ^{3}He, ^{6}Li, ^{7}Be, and ^{22}Na. Many of these isotopes investigated by Biersack and Fink. were also profiled for implantation in materials other than silicon, which Ziegler focused on, such as niobium and molybdenum. The authors were also the first to describe in considerable detail the origin of uncertainties in NDP techniques. The authors attribute the uncertainties to the finite acceptance angle of the system, the energy resolution of the system, energy straggling, and angular scattering of the emitted particles. Further research into the dependence of depth resolution on detector angle was performed and described by Cervena *et al.* [9] in 1981.

Since Ziegler introduced the NDP technique in 1972, it has been used in various facilities for many different applications. A list of different applications was presented by Downing *et al*. [5] in 1993. Most relevant to this work is the small amount of NDP research into lithium concentrations in thin-films and electrochromic materials. The first investigation of lithium in electrochromic materials was published by Krings *et al.* from The Netherlands in 1998 [10]. In their paper, the authors describe a characterization of WO_3 films by analysis with NDP, Secondary Ion Mass Spectrometry (SIMS), Elastic Recoil Detection (ERD), and X-ray Photoelectron Spectroscopy (XPS). The films that

were studied were 240 nm in thickness. It is important to note that the authors stressed the serious drawback of SIMS analysis was a high-risk of neutron induced Li-migration when analyzing these oxide samples with SIMS. The use of NDP does not contribute this threat, nor does it destroy the sample as SIMS does. In their conclusions, the authors mentioned that the SIMS results might not be reliable due to fast-migration, but that their NDP results were thought to be accurate. Analysis of the WO_3 films by way of ERD and XPS was unsatisfactory to the authors and did not measure accurate results. ERD of the samples caused deterioration of the surface and consequently limited depth resolution. The XPS technique was simply not sensitive enough to the lithium for accurate characterization.

Lamaze and Chen-Mayer also discuss lithium profiling of thin-film materials. The thin-films of their study were created by ion beam assisted deposition (IBAD) to a thickness of ~1 μm [1, 2]. The authors determined profiles of thin lithium phosphorus oxynitride (LiPON) films as well as thin lithium cobalt oxide ($LiCoO_2$) films. However, while analysis of specific electrochromic films was performed *in situ* by the authors, the focus of their studies was on the IBAD creation of the film. The study did not involve $LiCoO_2$, LiPON, or any other films that were both profiled after actually being part of or operated in a lithium ion cell under varying conditions. The latter was the focus of this report, and the author gives credit for the papers previously described as the inspiration.

Lithium Ion Cells

The first commercial lithium ion battery was introduced to the market by Sony in 1990 [11]. Although not the first rechargeable cell by far, the $LiCoO_2$ composition of the cell's cathode was the most commercializable in terms of cost, performance, and safety. The insight to allow the layered structure of CoO_2 to be used for the lithium insertion cathode was the brainchild of Mizushima, Jones, and Goodenough [12]. Since the

commercialization of this cell, its expansive utility in portable electronics has created a substantial interest in its capabilities as well as its faults.

A range of scientists including chemists, physicists, and materials scientists are conducting research towards the development of new materials to satisfy the continuous demand for energy. New applications are arising that bring about limitations of current lithium ion technology. Many applications, such as hybrid electric vehicles (HEV), have safety and power requirements that common cathodes cannot supply.

A major problem within layered lithium ion cathodes is the chemical instability of the cathode after a large amount of the lithium has been removed from the cathode structure [13]. This limits the ability to access the full theoretic potential capacity of the cell. Another issue common to nearly all lithium ion cells is the degradation in cell performance seen over time. This problem is a result of the disparity between the concentration of lithium ions that travel toward the anode during charging and those that return to the cathode during discharge. This problem, capacity fade, is addressed time and time again in the literature. Avery and Black, in their 1997 paper [14], performed a kinetic analysis of capacity fade within lithium/coke half-cells. Their ultimate conclusion was that migration of debris from the solid electrolyte interfacial (SEI) layer, a layer formed at the electrode-electrolyte interface, was the cause of voltage drops that led to capacity fade. While the topic of capacity fade is far from summed up by just the SEI, the formation of the SEI is well accepted.

A comprehensive paper discussing some of the more significant issues with lithium ion cells was published in 1998 by Arora, White and Doyle [11]. The authors discuss capacity fade and side mechanisms within the lithium cells. The paper is a roadmap for the scientific community as to what problems exist and must be solved for the advancement of lithium cells.

Premanand *et al.* researched the capacity fade of lithium ion cells in 2002 [15]. The authors focused on spinel-based lithium cells. They sought to minimize capacity fade

by optimizing the charging protocol of the cells. In the end the group concluded that loss of active materials from the electrodes was a significant cause of capacity fade. Ning *et al.* supplemented the latter results in their publication from 2003 [3]. The group specifically looked at cycled lithium ion batteries that were discharged at high rates. The Ning group concluded that the loss of secondary material within the cell was the leading cause of capacity fade.

Yoshida *et al.* performed extensive analysis on lithium ion cells to investigate degradation mechanisms such as capacity fade's relation to the thickness of the SEI as suggested by Avery and Black. Yoshida *et al* published their conclusions [4] that the capacity of lithium ion cells decreased with increasing thickness of the SEI layer on the anode. This conclusion is not entirely different from that of the latter groups, Ning *et al.* and Premanand *et al.* since the increasing thickness of the SEI would result in a loss of active material from the electrode.

RESEARCH OBJECTIVES

The list of papers that could be described in this section is enormous and steadily growing day by day. Those that have been listed have many more publications that have supplemented their findings and have researched similar phenomena with an array of different materials. However, the papers listed were mentioned because they acted as the primary motivation behind the types of cell conditioning and analysis that were performed for this report. The problems discussed throughout the literature of lithium ion battery research all have a clear need to understand how the lithium is behaving throughout the electrodes. Is it concentrating near the surface? Is the assumption that the Li^+ ions diffuse uniformly throughout the electrode true? Are stabilizing cations preventing phase segregation near the cathode surface? Is the solid electrolyte interface (SEI) breaking down due to storage at temperature?

Some of these questions have been studied through voltammetry, XRD, FIB, SEM and other techniques. But limitations of these techniques including maximum depth capability, fast ion migration, achievable resolution, and others leave many of the latter issues still not fully understood. NDP has the capability to offer a more complete picture of lithium behavior and diffusion within the electrodes of lithium ion cells after they have been exposed to many different conditions. In comparison to other techniques, NDP can see deeper, with sufficient depth resolution, and be less disturbing to the sample during analysis. The ability of NDP to accurately and precisely profile various different electrode types after being operated in a lithium ion battery, and the many areas in which NDP can be cleverly applied is the subject of this dissertation. The four primary objectives of this dissertation that offer new contributions are:

1. Validate the credibility of depth profiles measured with The University of Texas Neutron Depth Profiling facility by benchmarking results against: the NIST NDP facility, SIMS, and MCNPX models.
2. Perform a feasibility study on the ability of NDP to accurately profile the lithium distribution in electrode materials that have been removed from a battery operated under various conditions.
3. Develop a methodology for the separation, preparation, and handling of electrode materials from commercial and lab made lithium ion cells.
4. Analyze significant areas of lithium ion cell research to which NDP may be applied and profile various electrode samples to test existing hypotheses about Li^+ behavior in lithium ion cells. This includes:
    i. Interfacial analysis and profiling of lithium passivation layers formed on graphite anodes.

ii. Analysis of lithium behavior in cathode materials to determine any contrast associated with charge/discharge rate, composition, cell cycling, or state of charge.

Chapter 2: Relevant Theory

This chapter is devoted towards incorporating the predominant theory that will be needed by the reader to understand the experiment and results in the following chapters. While both the subjects of NDP and lithium ion electrochemistry could be broken down into level upon level of complexity, only the major theory will be discussed in hopes of illustrating how well the technique of NDP falls in line with the fundamental ability of a lithium ion cell to function.

PARTICLE INTERACTIONS

Depending on the target that a neutron strikes and the energy with which it strikes it, a large variety of analytical experiments may be devised to utilize neutron reactions. When an incident neutron interacts with nuclei, it may experience elastic or inelastic scattering, radiative capture, it may produce more neutrons, it may fission, or it may undergo many other reaction types.

Elastic scattering is the process where the incident neutron strikes a nucleus and then reappears without transferring energy into the nucleus. If the nucleus is elevated to an excited state as a result of a neutron scatter, then the interaction is considered to be inelastic scattering. Due to the nucleus reaching an excited state, inelastic collision is often followed by a characteristic inelastic γ-ray to return the nucleus to its ground state.

A reaction that has proved quite useful to the nuclear field is the radiative capture reaction. In this reaction the absorption of the neutron followed by the emission of a γ-ray is an exothermic process. This process can occur immediately resulting in a prompt γ-ray or the process may be delayed resulting in a delayed γ-ray.

The most widely known nuclear reaction is that of fission. In this reaction the incident neutron is absorbed into the target nucleus and ultimately results in the nuclei splitting apart. Once fission has occurred, other radiation such as γ-rays and other neutrons may be admitted.

The neutron interaction that has not been mentioned is that which is of the greatest importance to NDP. There are a large variety of particles that may be emitted following a neutron absorption reaction. For the purposes of NDP the most useful particles include protons, alphas, and triton particles. However the heavier recoil nuclei such as ^{7}Li from the ^{10}B(n,α)^{7}Li reaction may also be useful and offer high depth resolution.

NDP relies upon the emission of charged particles after neutron absorption by the isotope being profiled. The non-destructive characteristic of NDP is based on the small rate at which these neutron absorption reactions occur. In the case of the ^{6}Li(n,α)^{3}T reaction that has a cross section of 940 barns, it would take nearly 2250 years of a constant 1.5 x 10^{8} n cm^{-2} s^{-1} neutron flux to react with 1% of the sample. That is to say that a negligible amount of the isotopes being profiled actually take place in the reactions that allow the material to be profiled. NDP's ability to profile materials in light of these conditions is one of its major advantages over other analytical techniques. NDP is most useful for light-element profiling due to the higher microscopic neutron-absorption cross-sections by which many light elements are characterized. Table 2.1 lists a few of the most useful reactions. The research discussed in this paper mainly utilizes the ^{6}Li reaction for analysis of lithium within electrodes. When bombarded with thermal neutrons, the absorption of a neutron by ^{6}Li results in the following reaction.

$$^{6}Li + n \rightarrow {}^{3}H\ (2727.88\ keV) + {}^{4}He\ (2055.12\ keV). \qquad (2.1)$$

Table 2.1: A few of the light-element neutron absorption reactions that may be used for neutron depth profiling [16, 17].

At. No.	Element	Reaction	Cross section (barns)‡	Abundance (or at/mCi)	$T_{1/2}$	Recoil Mass Energy (keV)	Particle Energy (keV)	Branch Ratio
3	He	$^{3}He(n,p)^{3}H$	5331	1.37E-06	-	191.291	572.465	
6	Li	$^{6}Li(n,\alpha)^{3}H$	940.3	0.075	-	2727.877	2055.515	
10	B*	$^{10}B(n,\alpha)^{7}Li$	3837	0.199	-	1013.126	1775.868	6.28%
10	B*	$^{10}B(n,\alpha)^{7}Li$	3837	0.199	-	839.635	1471.763	93.70%
14	N	$^{14}N(n,p)^{14}C$	1.83	0.99634	-	42.02	583.851	
17	O	$^{17}O(n,\alpha)^{14}C$	0.24(?)	3.80E-04	-	404.064	1413.632	
33	S	$^{33}S(n,\alpha)^{30}Si$	0.1686	0.0075	-	411.534	3081.804	
35	Cl	$^{35}Cl(n,p)^{35}S$	0.489	0.7577	-	17.233	597.931	
40	K	$^{40}K(n,p)^{40}Ar$	4.4 (0.39 α)	1.17E-04	1.277 E9 y	56.259	2230.781	
7	Be	$^{7}Be(n,p)^{7}Li$	~ 48000	2.45E+14	53.12 d	206.523	1437.718	
22	Na†	$^{22}Na(n,p)^{22}Ne$	27800	4.38E+15	2.6019 y	158.831	3465.797	0.84%
22	Na†	$^{22}Na(n,p)^{22}Ne$	27800	4.38E+15	2.6019 y	102.979	2247.069	99.10%
59	Ni	$^{59}Ni(n,\alpha)^{56}Fe$	~ 12.3	1.28E+20	76000 y	340.316	4755.791	
210	Po	$^{210}Po->\alpha->^{206}Pb$	---	6.38E+14	138.376 d	103.077	5304.381	

* A 477.595 (3) keV (IAEA) γ emission occurs in 93.9 % of the ^{10}B reactions
† A 1274.58 keV γ emission occurs in XX % of the ^{22}Na reactions

The energies of the products emitted from the reaction are determined according to standard conservation of energy calculations. The small incident kinetic energy of the neutron (in the meV range) is nearly negligible and thus the center of mass from which the products are emitted can be considered to be the original position of the lithium atom.

In order to calculate the rate at which the above reactions occur when subjected to an incident thermal neutron flux of ϕ neutrons sec^{-1} cm^{-2}. We must consider the concentration of ^{6}Li atoms, the cross-section of the neutron absorption reaction that is listed in table 2.1 to be 940 barns, and the neutron flux. The product of these values produces our reaction rate, *RR*, as described by equation 2.2.

$$RR = N\sigma\phi \qquad (2.2)$$

where,

N= ^{6}Li concentration (atoms/ cm^{3}), σ= miscroscopic cross-section (cm^{2})

The value of equation 2.2 will leave us with the number of neutron absorption reactions that occur per second per cubic centimeter. Since the irradiation time and dimensions of the sample are known, the number of reactions that take place may be calculated.

INTERACTIONS OF CHARGED PARTICLES WITH MATTER

Once the light-isotope of interest has absorbed the neutron, it may emit a charged particle and a recoil nucleus. For the case of ^{6}Li, an alpha and a triton are emitted as described in equation 2.1. The energy loss of the charged particle as it exits the sample matrix is the key measurement for NDP to achieve. The charged particle will be monenergetically emitted with energy E_0, and will interact with the electron density in the sample matrix throughout its path out of the sample.

The amount of energy that the particle will lose along its exit path is dependent upon the *stopping power* of the material. The stopping power, *S(E)*, is the average energy loss of the particle per unit path length in the material [18]. The stopping power will depend on both the characteristics of the particle, as well as the properties of the material through which it travels. The particle can lose energy through electronic and nuclear interactions; to describe the amount of energy lost per unit length we use equation 2.3.

$$S(E) = -\frac{dE}{dx} \tag{2.3}$$

Equation 2.3 will maximize near the end of the particle's path length at a point known as Bragg's peak. A depiction of an entire curve, a Bragg Curve, of a particle's stopping power along its range is shown in Figure 2.1.

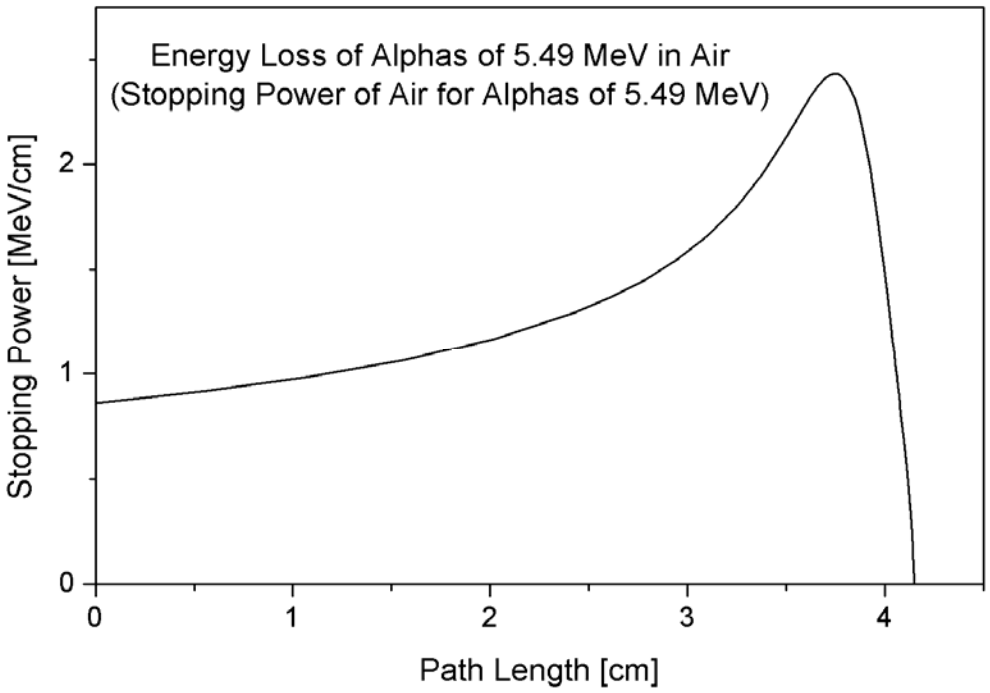

Figure 2.1: A Bragg peak for an alpha particle traveling through air.

As mentioned earlier, the interactions between the particle and the surrounding material include electronic and nuclear reactions. The electronic stopping is the dominant reaction early in the particle's range (*i.e.* when it still has most of its energy). Electronic stopping will consist of inelastic collisions in which the particle will interact with bound electrons in the medium in such a way that the particle may cause excitations to both the bound electron as well as its own electron cloud [19].

Throughout the electronic stopping process the particle will experience a variety of charge states. To track all of these states would be extremely difficult, and consequently an average electronic stopping power, $S_e(E)$, is generally used. Calculation of $S_e(E)$ can theoretically be done with using the Bethe-Bloc formulations [19-21] to an accuracy within a few %. However it is more expedient, as well as accurate, to use numerical methods and codes for these calculations. The primary code used for these

calculations in NDP is *The Stopping and Range of Ions in Matter (SRIM)* code developed by Ziegler, Biersack, and Littmark [22].

Towards the end of a particle's range it will begin to experience higher levels of nuclear stopping interactions. Nuclear stopping, $S_n(E)$, involves energy loss due to elastic collisions between the particle and atoms within the sample. The effect of nuclear stopping at low particle energy will be more dramatic for heavier particles, whereas for light particles the effect may never be significant. As the particle's energy becomes low enough, significant interactions between the particle and nuclei from the material can begin to cause damage to the material. If ions from the material are struck with enough energy they can be dislocated from their lattice structure.

A continuing problem has been to accurately describe the repulsive potential between the charged particle and nuclei within the material. A fundamental description of the repulsive potential, $V(r)$, as a function of radius is given by equation 2.4.

$$V(r) = \frac{1}{4\pi\varepsilon_0}\frac{Z_1 Z_2 e^2}{r}\varphi(r/a) \tag{2.4}$$

Here we have the repulsive potential between two nuclei that are very close where Z represents their corresponding charges, r is the distance between them, and $\varphi(r/a)$ is the screening function that is dependent on the screening parameter, a.

The reason that repulsive potential is mentioned here is because while there are numerous different potentials described over the years, one of the most widely used potentials is the ZBL repulsive potential [22] described by Ziegler, Biersack, and Littmark and also used in their SRIM code. The ZBL potential is defined by its screening function as follows in equation 2.5 [23].

$$\varphi(x) = 0.1818e^{-3.2x} + 0.5099e^{-0.9423x} + 0.2802e^{-0.4029x} + 0.02817e^{-0.2016x}$$

where,

$$x = r/a_u, \tag{2.5}$$

$$a = a_u = \frac{0.8854a_0}{Z_1^{0.23} + Z_2^{0.23}}$$

Here, a_0 is the Bohr atomic radius = 0.529 Å. The ZBL repulsive potential described here is used in the SRIM program along with a binary collision approximation (BCA) for the calculation of ion range. The BCA program works by numerically solving the classical scattering integral for each individual collision simulated for the specified ion and material. While SRIM is the most widely used BCA program for these types of calculations, there are others that try to overcome some of SRIM's shortcomings, such as its lack of accountability for crystal structure. SRIM's failure to account for crystal structure is really most detrimental for those samples that will exhibit large amounts of channeling through crystal planes. For the majority of purposes, however, SRIM is the most readily available, accurate, and user-friendly software for stopping power calculations.

After $S_e(E)$ and $S_n(E)$ have been calculated, either computationally or by hand, then it is straightforward to find the total stopping power. For most particles except those of extremely high energies (>several hundreds of MeV per nucleon) the total stopping power, $S(E)$, is then just the sum of the electronic and nuclear stopping powers as in equation 2.6.

$$S(E) = S_e(E) + S_n(E) \tag{2.6}$$

The particle's complete range traveled in the material until exiting with energy, $E(x)$, can then be determined by the integral relation of equation 2.7.

$$x = \int_{E(x)}^{E_0} \frac{dE}{S(E)} \tag{2.7}$$

The direct relation between energy and path length, *x*, is the foundation of NDP. From a spectrum of measured charged particle energies, *E(x)*, that have emerged from a material with a known stopping function, *S(E)*, it is possible to determine the original depths from which the neutron absorption reaction occurred.

DETECTOR PHYSICS

It is fitting that the interactions between charged particles and the materials they traverse serve not only as the subject of NDP's analysis, but also as the mechanism by which the charged particles are detected. Muller *et al*. [7] were the first to publish NDP work using silicon surface barrier detectors, and since then it has since become the standard for NDP. The sensitive, but resilient, silicon detectors offer a convenient method for charged particle detection without the need for cooling.

Silicon resides in Group IV of the periodic table where, along with carbon, germanium, and tin, it is characterized by its four valance electrons. What truly makes silicon interesting is that the electrons in this valence band have the potential to "jump" into the conduction band. In order to "jump" to the conduction band these electrons must cross an energy gap, E_g, of 1.115 eV. This number is quite important. Any lower, such as the germanium energy gap of 0.7 eV and silicon would produce too many carriers (electrons in the conduction band) at room temperature. Any higher, such as carbon's 6 eV and silicon's electrons would not be able to jump the gap and silicon would instead act as an insulator.

The energy gap of silicon gives it great potential for the accurate detection of charged particles at room temperature. In a detector, a silicon crystal is set between a

positive and negative electrode. The electrodes are present to collect any charge carriers induced by incident ionizing radiation, such as a charged particle. The number of charge carriers produced is proportional to the energy of the incident radiation. Each electron that gains enough energy from the incident charged particle to jump from the valence band to the conduction band of the silicon becomes doubly effective because it also produces a *hole*, the absence of an electron, that acts effectively as a positive charge carrier [24]. The charge carriers are moved towards the electrodes by an electrical bias placed across the detector.

The charge carriers produced by silicon provide it with intrinsic conductivity. The ability of silicon to have this property is referred to as *intrinsic semiconductivity* [25]. Conductivity, σ, can be quantified in the following way. Each electron that jumps into the conduction band is now a negative (*n*-type) carrier. Likewise, each electron hole that is formed in the valence band is a positive (*p*-type) carrier. Each of the carriers is described by their mobility, μ_n and μ_p, within their domain; the conduction band for the electrons, and the valence band for the holes. Adding both of their effects, the total conductivity for an intrinsic semi-conductor is [24],

$$\sigma = n_n q\mu_n + n_p q\mu_p \quad . \tag{2.8}$$

Equation 2.8 may be simplified a bit for intrinsic semiconductors since the number of electrons should equal the number of electron holes so that n_n=n_p. Also the charge, q, is the same 1.6 x 10^{-19} C for both except for the sign difference. Now our knowledge of how conductivity within a semiconductor is derived allows us to discuss the importance of why dopants are used, and how techniques such as NDP take advantage.

The four valence electrons of silicon become quite important due to the crystalline structure of silicon shown in figure 2.2. Like a diamond, silicon has a structure such that each of its four valence electrons is covalently bonded to a neighboring silicon atom.

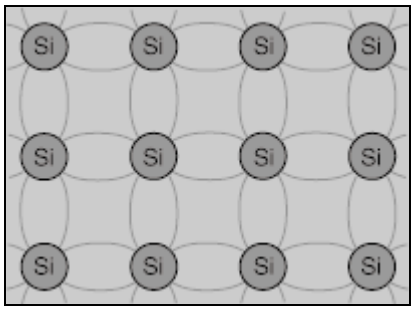

Figure 2.2: Silicon atom structure [26].

The electron sharing that is shown in figure 2.3 gives good insight into why doping of an intrinsic semiconductor can have such profound effects. Consider how the addition or absence of a valence electron to the crystalline structure would occur. In fact this is exactly the effect that doping has. The addition of a pentavalent atom such as antimony, phosphorus, or arsenic leaves an additional valence electron that is not used in the covalent bonding process. On the other hand, the addition of a trivalent atom such as aluminum, boron, gallium, or indium creates a hole in the crystalline structure since there are not enough electrons for the full bonding process [27].

Doping of an intrinsic semiconductor with a pentavalent impurity introduces an excess of negative charge carrying electrons, and is accordingly called an *n*-type material. Doping with a trivalent impurity creates more positively charged electron holes and thus results in a *p*-type material. The semiconductor materials are now considered *extrinsic semiconductors* due to the doping.

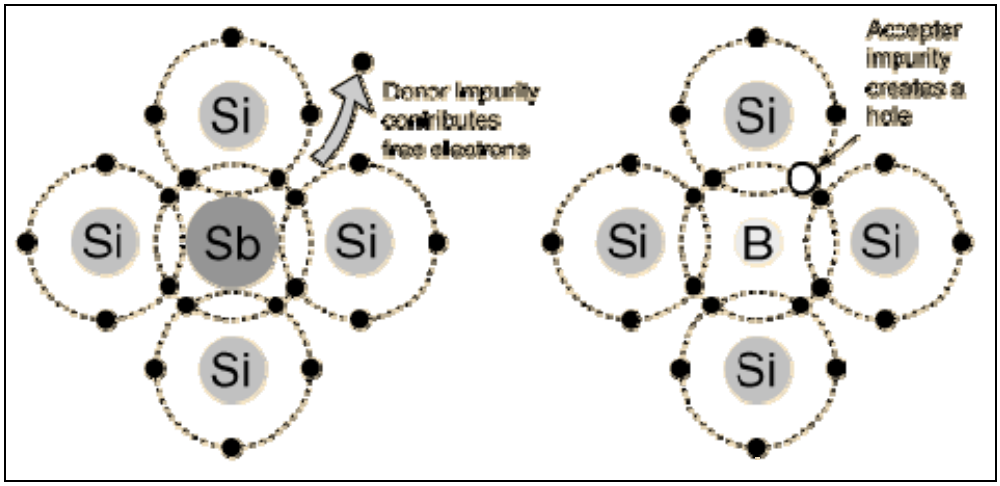

Figure 2.3: Semiconductor doping [26].

The Pauli exclusion principle allows for only two electrons of opposite magnetic spin to exist simultaneously in the same energy level. Consequently, the extra electron provided by the pentavalent impurity resides at an energy level, the *donor* level E_d, closer to the conduction band than the other electrons [24]. This means that only a small amount of energy, relative to the original E_g, must be imparted to free the electron.

Electron holes that are created in *p*-type materials from trivalent atoms allow for electrons to move from the valence band to the *acceptor level*, E_a. The acceptor level is just above the valence band making it more probable for electrons to enter the acceptor level than the conduction band. Each electron that leaves the valence band for the acceptor level leaves a *p*-type carrier behind for semiconduction.

Recalling the conductivity equation discussed earlier it is evident that the doping of intrinsic semiconductors can quickly alter the original characteristics of the material. Doping of semiconductor materials becomes very useful in the field of electronics. Many devices including thermistors, transistors, and LEDs utilize *n*-type, *p*-type, or a combination of the two semiconductors to perform their specific function. However, incorrect doping amounts or distributions of the impurities can have detrimental

consequences to the devices functionality. The high sensitivity of semiconductors to doping is why the ability to analyze the doping distributions of semiconducting materials such as silicon without destroying them is necessary.

The sensitivity of the silicon surface barrier detector is not as resolved as the germanium detectors, however it is common for silicon detectors to have alpha particle resolutions down to 13 keV for the full width at half maximum (FWHM). While not perfect, this resolution is suitable for most needs of NDP, and certainly sufficient the work described in this report.

ELECTROCHEMISTRY AND BATTERY CONCEPTS

Lithium ion cells are very common in the technological age at hand. The current global market for batteries exceeds $30 billion per year [28]. Lithium ion cells are no longer relegated to menial purposes such as running calculators. Today lithium ion cells are seen in a variety of portable electronics, and recent regulation changes for air-quality control are a strong impetus to bring lithium ion cells to the forefront of hybrid electric vehicles (HEV).

Today, the motivation behind lithium ion cell research is to develop new cell compositions or processes to solve many of the present issues with cost, performance, and safety [29]. Many new cathode compositions are being researched beyond the most common $LiCoO_2$. Some groups have focused on various processes to substitute alternate transition metals into the layered structure, while others work on more complicated spinel and olivine compositions.

The common link is that all of those mentioned utilize the movement of Li^+ ions. The use of various analytical techniques is involved with the improvements that are

sought for lithium ion cells, and every new perspective is an advantage. There are only limited methods to determine the shape of the lithium distribution throughout the electrodes, and those that rely on ion sputtering or recoil such as SIMS or ERD, are often too destructive to the sample to allow for accurate analysis [10]. The following section will describe simple theory of lithium ion cells so that the reader may fully grasp the results of this report and the advantage of NDP for analysis of these cells.

Electrochemical Cells

Lithium ion cells are a type of electrochemical cell. Simply described, an electrochemical cell is a system with two electrodes separated by an electrolyte phase [30]. The electrodes are defined as the anode or the cathode depending upon their role in the cell. The anode (negative electrode) is characterized as the electrode that is oxidized and therefore releases electrons into the external circuit. The cathode (the positive electrode) is the electrode that is reduced and receives electrons from the external circuit. The electrolyte may be solid or liquid and it acts as the medium of charge transfer between the anode and cathode through the transfer of ions.

A battery is a system of electrochemical cells that are connected in series or parallel dependent upon the needs of voltage or current. The ability of a battery to be recharged is the defining characteristic of whether a battery is of the primary type, which cannot be recharged, or of the secondary type, which may be recharged. The recharging of these cells is actually the case of reversing the oxidation-reduction (redox) reactions in the cells through which they discharged in the first place.

During the electrochemical reaction of the cell, the anode, *M*, is oxidized according to equation 2.9.

$$M \rightarrow M^{n+} + ne^{-} \tag{2.9}$$

The electrons given up by the anode are transferred via charge collectors so that the cathode, *X*, may accept them as in equation 2.10.

$$X + ne^{-} \rightarrow X^{n-} \tag{2.10}$$

Although the electrons are transferred across a circuit, the ions are transferred through the electrolyte phase that is specifically designed to allow for strong ionic conductivity while inhibiting the flow of electrons. When equations 2.9 and 2.10 are summed, the overall reaction is as shown in equation 2.11.

$$X + M \rightarrow X^{n-} + M^{n+} \tag{2.11}$$

The overall reaction is useful when seeking to determine the amount of a particular substance that will be needed to produce a particular amount of electricity. As stated by Faraday, the amount of electricity passed in the cell is directly related to the masses of the reactants involved and the products formed [28]. To calculate the number of moles, N_m, of reactants needed to pass a current I amperes for a time of t seconds

across the cell, Faraday's law relates the total charge transferred, It, to N_m by equation 2.12.

$$N_m = \frac{It}{nN_A e} \tag{2.12}$$

Where n is the number of electrons given up, e is the electron charge, and N_A is Avogadro's number. Substituting the Faraday constant, F, for the product of $N_A e$, where F= 96,487 C mol^{-1} then equation 2.12 becomes equation 2.13.

$$N_m = \frac{It}{nF} \tag{2.13}$$

From equation 2.13 it is simple to then determine the theoretical capacity of charge, Q, which can be given by the cell as,

$$Q = It = N_m nF \tag{2.14}$$

By then defining the *equivalent weight* of a material as the molecular weight divided by the number of electrons involved in the reaction, we can understand the major result of equation 2.14. For every gram equivalent weight of electrode, there is a theoretical capacity of 26.8 Ah.

Lithium Ion Cells

Lithium ion cells undergo simple redox reaction as described by equation 2.11. They can deliver almost 4 volts with specific energies near 120 Whr kg^{-1} [29]. The energy, E in Wh kg^{-1}, of the cell is calculated as the product of the cell voltage, V in volts, times the specific capacity, Q in Ah kg^{-1}, of the cell as in equation 2.15 [30],

$$E = (V) \text{ x } (Q) \tag{2.15}$$

Lithium ion cells are particularly important because of their higher energy density relative to other rechargeable systems such as nickel-metal hydride (NMH) or nickel-cadmium batteries. The most common cells today are composed of a lithium transition metal oxide ($LiMO_2$) for the cathode material and a carbonaceous material for the anode. These electrodes are intercalation compounds, meaning that they are solids that can reversibly incorporate and release guest atoms into their crystal lattice without much structural change. Figure 2.4 below is a diagram of the common $LiCoO_2$ cell.

When lithium ion cells are charged, the electric field causes lithium ions and electrons to move towards the anode where the lithium ions are intercalated into the carbon anode. Design of these batteries takes care to insure that while the electrodes have good conductivity for both the ions and electrons, this is not the case for the electrolyte. The electrolyte's role is to allow for conduction of the ions from the cathode to the anode, and vice versa, but to prevent the conduction of electrons. If this were not the case, the cell would simply be shorted out.

In the charged state the cathode is considered delithiated and is generally described as $Li_{1-x}MO_2$ while the anode is now Li_xC_6 such that *x* may describe the stoichiometric amounts of lithium in each electrode. Upon discharge, the reaction is reversed as seen in figure 2.4.

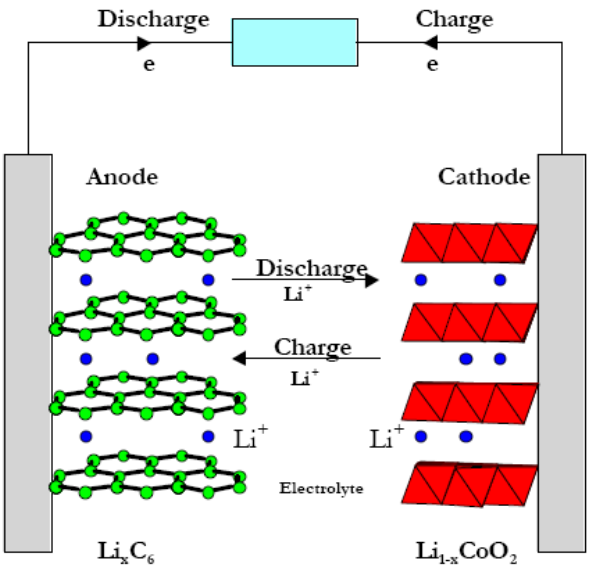

Figure 2.4: Diagram of the intercalation mechanisms within $LiCoO_2$ cells with a carbon anode [30].

INTERCALATION MATERIALS AND LITHIUM BEHAVIOR

The most widely used anode material for lithium ion cells is graphite along with a lithium-containing oxide material for the cathode. Lithium ion cells are different from common electrochemical cells in that the electrolyte is non-aqueous in many of them. The nonaqueous electrolytes are all compounds based on organic solvents including ethylene carbonate (EC), propylene carbonate (PC), dimethyl carbonate (DMC), dimethoxyethane (DMX), and diethyl carbonate (DEC). Use of these nonaqueous electrolytes allow for a wide range of operating temperatures, between –40˚ to 70˚ C for

the cells. To allow for ionic conduction, $LiPF_6$ complex salts are dissolved into organic solvents, however the concentration of Li within the electrolyte must be optimized to prevent solvation of the Li^+ ions [31].

The lithium ion cell system allows for lithium ions to be reversibly intercalated into both electrodes. An open circuit voltage (OCV) is created in the cell since the electrodes in this system are competing for electrons and have different reduction potentials. The OCV is the difference in electrochemical potential between the electrodes of a circuit system when no load is on the system.

The OCV of a $LiCoO_2$ cell is approximately 4.0 V [29]. OCV is a defining characteristic of any electrochemical cell. For lithium ion cells it represents the difference in electrochemical potential created by the difference in lithium ions between the anode and the cathode. The OCV is calculated from the difference of electrochemical potentials of the anode and cathode. To calculate the electrochemical potential of lithium ions while accounting for the electrostatic effect [32] of the ion the calculation is [30],

$$\overline{\mu}_{Li}^{\alpha} = \mu_{Li}^{\alpha} + zF\phi$$

where,

$\overline{\mu}_{Li}^{\alpha}$ = electrochemical potential of lithium ion in the α phase

μ_{Li}^{α} = chemical potential of lithium ion in the α phase

z = number of electrons

F = Faraday constant

ϕ = potential in the α phase

In the above equation the chemical potential is calculated as,

$$\mu_{Li}^{\alpha} = (\mu_{Li}^{0})^{\alpha} + RT\ln(a_{Li}^{\alpha})$$

where,

$(\mu_{Li}^{0})^{\alpha}$ = standard chemical potential of lithium in the α phase

R = gas constant,

T = temperature in Kelvin,

a_{Li}^{α} = activity of lithium ion in the α phase

With the electrochemical potentials known, we may then calculate the OCV of the cell as:

$$V_{OC} = -(\overline{\mu}_{Li}^{anode} - \overline{\mu}_{Li}^{cathode}) \Big/ nF \tag{2.16}$$

Equation 2.16 is significant in that it describes a direct relation between the cathode and anode materials. The electrochemical potentials of each will determine the voltage of the cell. However, there are many other properties of the electrodes that will affect the cell's performance and ability to be commercialized as well [33]. These include,

- Degree of available lithium insertion
- High electronic conductivity
- High ionic conductivity (*i.e.* 1-D diffusion, 2-D diffusion, 3-D diffusion)
- Location of ion (*i.e.* octahedral, tetrahedral)
- Good reversibility (no structural damage)
- Ease of synthesis
- Light weight
- Low cost

- Environmentally benign

The points listed above are just a few of the important aspects that are considered when developing new electrodes, primarily cathodes, for lithium ion cells. The anodes of lab made lithium ion cells are typically always pure lithium. Lithium has a high standard oxidation potential and it the lightest solid in the periodic table. Electrochemical potentials for cathode materials are always determined relative to a lithium potential of zero. Commercially manufactured cells generally use graphitic anodes that have lower electrode potentials <1V vs. lithium [28]. Often this graphite is highly ordered pyrolytic graphite (HOPG) or mesocarbon microbeads (MCMB).

While anodes are still researched, the cathode composition is more often the topic of research. Too many compositions have been researched to list here, however many are simple substitutions of transition metals within the common layered $LiMO_2$ structure [34]. Other compositions often take advantage of more complicated lattice structures for their diffusive capabilities or other material properties. A few of these include [31],

Layered ($Li^{+}M^{3+}O_2$)	Spinel	Olivine
$LiCoO_2$	$LiMn_2O_4$	$LiFePO_4$
$LiNiO_2$	$LiMn_{1.8}Li_{0.1}Ti_{0.1}O_4$	
$LiMnO_2$	$LiMn_{1.8}Li_{0.1}Ti_{0.1}O_{3.9}F_{0.1}$	
$LiNi_{1/3}Mn_{1/3}Co_{1/3}O_2$		
$LiNi_xMn_yCo_{1-x-y}O_2$		
Li_xTiS_2		

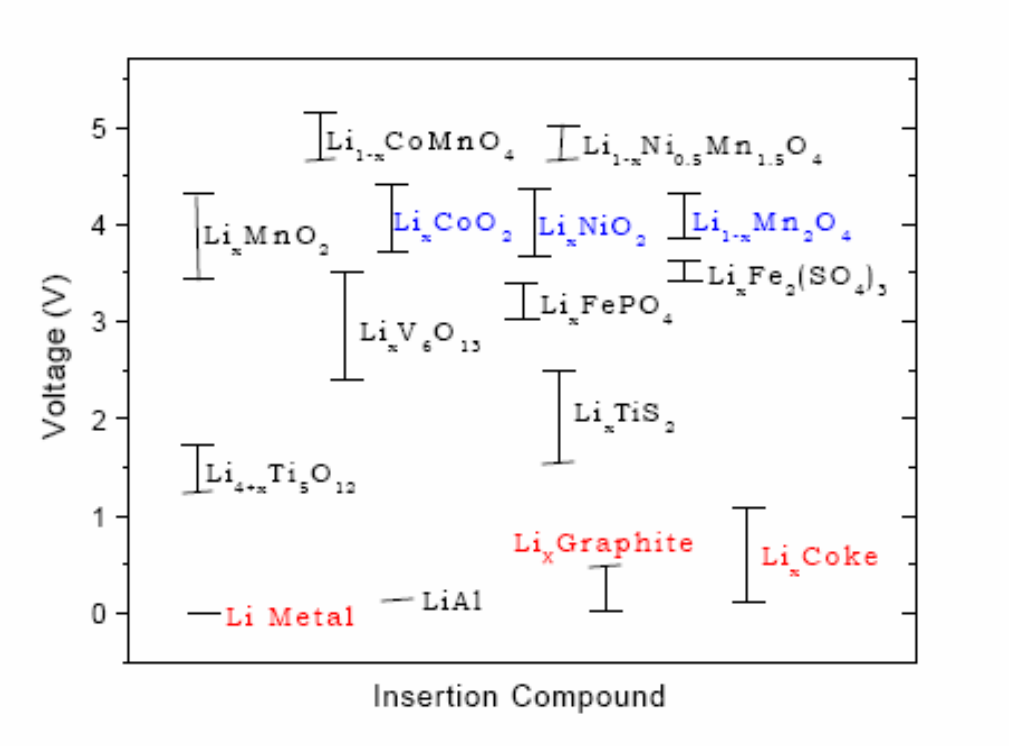

Figure 2.5: A comparison of cathode voltages vs. lithium [30].

A few of the listed compositions are shown in figure 2.5 for a quick comparison of the voltages they offer vs. lithium [30].

Layered $Li^{+}M^{3+}O_2$

The layered $Li^{+}M^{3+}O_2$ structure has a face centered cubic structure (FCC). The FCC structure is often described by the example of sodium chloride, NaCl. The Cl^{-} ions occupy the sites that form the centered cubic arrangement, these are the larger (green) ions represented in figure 2.6. The Na^{+} ions occupy all of the octahedral interstitial sites, represented by the smaller (blue) ions in figure 2.6. Octahedral sites are simply the sites

between 6 regular atoms that form octahedra. The atoms occupying these sites will be an equal distance from the body center and face centers of the unit cell.

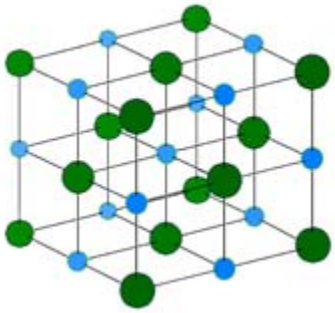

Figure 2.6: Unit cell of FCC structure of NaCl. Cl^- are the larger, green spheres. Na^+ are the small blue spheres [26].

The FCC structure of NaCl, also know as cubic close packing (CCP), as shown in figure 2.6 is the structure of the layered $Li^+M^{3+}O_2$. Figure 2.7 illustrates how the atoms for the $Li^+M^{3+}O_2$ are arranged. The Li^+ and M^{3+} atoms order along the alternate planes of the sodium chloride lattice due to charge and size differences. For $LiCoO_2$, the layer sequence is –O-Li-O-Co-O- along the c axis. The Li^+ occupies octahedral interstitial sites. As a bias voltage is applied to the cell and it begins to charge, the Li^+ ions will move out of the octahedral sites and towards the anode. The Li^+ ion will move 2-demensionally from octahedral site to tetrahedral site, and then to another tetrahedral site and so on. The 2-demensional motion allows for fast Li^+ diffusion and a corresponding high σ_{Li}. However, the tetrahedral sites will share faces with 3 neighboring octahedra in the lithium layer and this can act to slow diffusion of the Li^+ ions due to electrostatic repulsion with the $M^{3+/4+}$ ions across the shared face. Figure 2.7 illustrates the lattice structure.

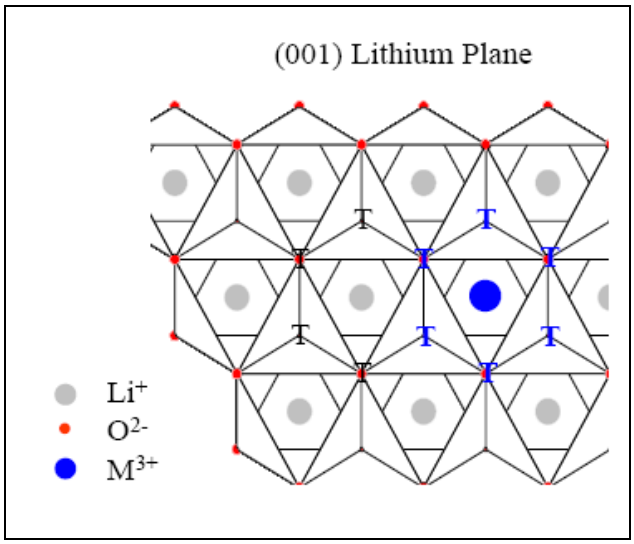

Figure 2.7: The lithium plane showing tetrahedral locations (T) used for Li^+ diffusion [31].

As the cell is charged, the cathode is delithiated as $Li_{1-x}MO_2$ and the valence of the transition metal, M, changes and electrons are released to the charge collectors. At this point Li^+ ions are intercalating into the anode structure. The amount, x, of Li^+ that can be removed from the $Li_{1-x}MO_2$ cathode is dependent upon the transition metal(s) in the compositions as well as their valence states. For the case of $LiCoO_2$, only 50% of the lithium may be removed so that x=0.5. This value corresponds to a capacity of 140 mAh g^{-1} [34]. The reaction with a carbon anode is,

$$LiCo^{3+}O_2 + C_6 \rightarrow Li^+_{0.5}Co^{3.5+}O^{2-}_2 + Li_{0.5}C_6$$

After the point of x=0.5, electrons begin to be removed from the O^{2-}:2p band as opposed to just the transition metal, $Co^{3+/4+}$:t_{2g} band, and the cathode becomes chemically

unstable. If the cell is charged beyond 0.5 lithium atoms per cobalt atom, the reversible capacity of the cell will be significantly diminished. To avoid the latter problem, other transition metals from the first row are often substituted for Co due to their low mass and ability to stabilize higher oxidation states. Substituting in one or a combination of these other transition metals can lead to a higher limit of lithium extraction that can be achieved without chemical instability.

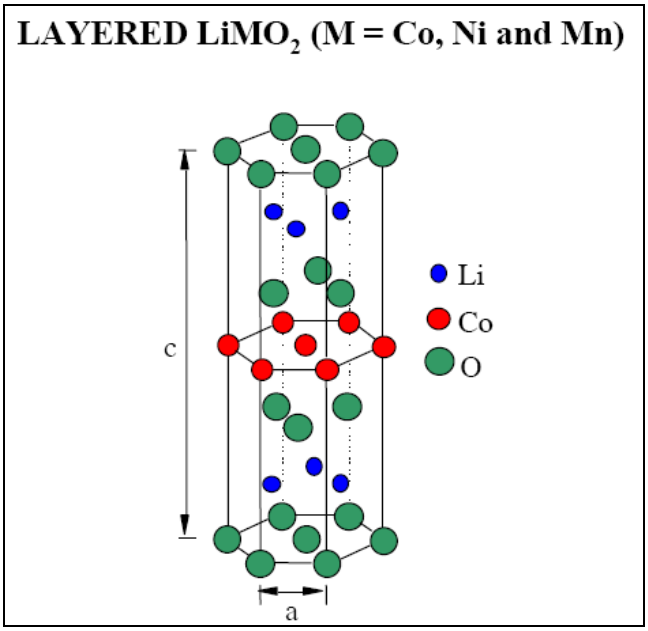

Figure 2.8: O3 structure of layered $LiCoO_2$ [31].

Of particular interest to this study was the $LiNi_{1/3}Mn_{1/3}Co_{1/3}O_2$ composition in which Ni and Mn were substituted for 2/3 of the Co presence. The presence of the Ni and Mn allow for the cell to achieve 65% of its theoretical capacity, as opposed to the 50% of $LiCoO_2$. This corresponds to a reversible capacity of 180 mAh g^{-1} for

$LiNi_{1/3}Mn_{1/3}Co_{1/3}O_2$ and 140 mAh g^{-1} for $LiCoO_2$. The range of intercalation for $LiNi_{1/3}Mn_{1/3}Co_{1/3}O_2$ is $0.35 \leq (1\text{-}x) \leq 1.0$.

Olivine $LiFePO_4$

This study includes analysis of $LiFePO_4$ cathodes and corresponding graphite anodes. The $LiFePO_4$ structure is an orthorhombic crystal (*i.e.* lattice parameters $a \neq b \neq c$) comprised of edge shared LiO_6 and FeO_6 octahedra along with PO_4 tetrahedra. The edge shared LiO_6 octahedra form chains along the b axis that result in 1-demensional Li^+ conduction [31]. When compared to the 2-demensional diffusion of the layered structure, the $LiFePO_4$ structure offers poor Li^+ ion conduction. However, the covalently bonded PO_4 groups and lower valence $Fe^{2+/3+}$ ions give the cathode good chemical stability and safety.

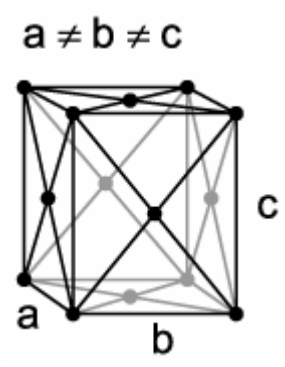

Figure 2.9: Orthorhombic structure of $LiFePO_4$ [26].

SOLID ELECTROLYTE INTERFACE

Many factors stemming from the physical design down to the chemistry of a cell can affect its performance. The best cells are those that can achieve an optimal balance of

cost, safety, and performance. The performance issues that will be discussed here are those that are most relevant to this study

The surface where the electrode and the electrolyte meet is called the electrode-electrolyte interface, or sometimes just the interface. At the interface there is lithium that is not stable when in contact with the nonaqueous propylene and ethylene carbonate solvents that are used. The result of this is a thin film of lithium-solvent reaction products that form over the surface of the material to passivate the lithium. The reactions will continue until a point where electron tunneling through the surface is no longer possible [29]. This surface is called the solid electrolyte interfacial (SEI) layer and forms because the electrolyte may conduct the lithium ions but is an electronic insulator.

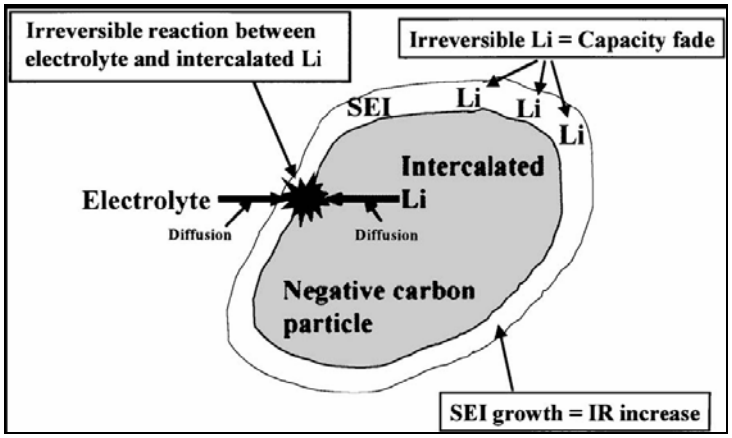

Figure 2.10: Illustration of the SEI presence at the anode [4].

Typical discussions in literature of the SEI speak more often of the SEI layer formed at the graphite anode [35], as in figure 2.2, than at the cathode. Truth be told, the graphite anode needs the SEI. Continuous side reactions can easily affect the layered structure of the graphite and cause such effects as exfoliation of the graphene planes and ultimately the deactivation of the anode [13]. The SEI prevents continuous reactions such

as cointercalation of electrolyte species with Li^+ ions into the graphite. Therefore the SEI is an important stability mechanism for the anode that allows for proper operation of the cell. It is well accepted that the SEI is a necessity for the proper intercalation/deintercalation of the Li^+ ions into the anode, and that the SEI must be stable for this to properly occur [36].

SEI formation begins at the first charge of the cell since the potential of LiC_6 is within 0.1 V of lithium metal. Its formation continues over various stages as a function of the anode potential. It is not clear when it stabilizes. The composition of the SEI is also a source of controversy, however it is generally accepted that the components of the SEI include LiF, Li_2CO_3, or lithium alkyl carbonates $ROCO_2Li$ [37, 38].

The thickness of an SEI layer varies, but has been approximated at 0.04 μm for a fresh battery, and then as high as 0.45 μm for a battery that had been in storage [4]. Yoshida's research into the SEI in connection with battery degradation attempted FIB and XPS analysis to find the thickness of the SEI but found that the methods were not very suitable; therefore the latter values of thickness are approximate. However, the group was able to conclude that the SEI thickness was closely related to the capacity loss of the cell as one would expect.

It is thought that the formation of an SEI on the carbon anode surface is primarily the result of the following three processes [4]:

1. Electrolyte diffusion from electrolyte to carbon surface
2. Intercalated Li diffusion to the negative carbon surface
3. The reaction of the electrolyte with the intercalated Li

The ions that are lost to the formation of the layer are lost and will not be recovered. This irreversible capacity is a capacity loss of the cell as shown in figure 2.11.

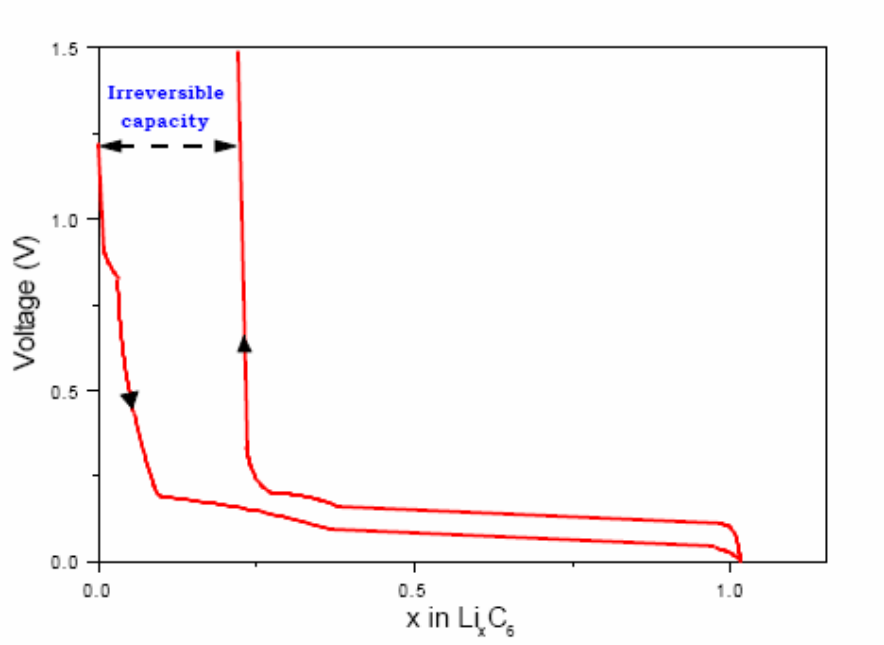

Figure 2.11: Discharge/Charge Cycling potential of a graphite anode [30].

The consequences of capacity loss are ultimately that the cell cannot deliver the full energy capacity that exists as calculated by the chemistry of the situation. One option to help alleviate this problem is to produce cathodes with excess lithium. The main point of mentioning the latter topics, however, is to illustrate the importance of the SEI to cell performance. It is clear that the presence of the SEI is a necessary mechanism that has the consequence of reducing the capacity of the cell.

One topic of this research is the evaluation of how the SEI is altered over time in an environment of 50ºC. Due to this necessity of the SEI presence on the anode, it is of

great interest to understand how it behaves under higher temperatures such as those it may experience when used for a hybrid electric vehicle (HEV).

Chapter 3: Experimental Apparatus

REACTOR FACILITY

The thermal neutron source for the NDP facility at The University of Texas at Austin is a 1.1 MW TRIGA Mark II research reactor. The reactor core consists of Uranium Zirconium Hydride fuel with 19.7% enrichment. A 2 Ci AmBe neutron source that produces 10^6 neutrons per second is utilized to begin the fission chain reaction for the reactor.

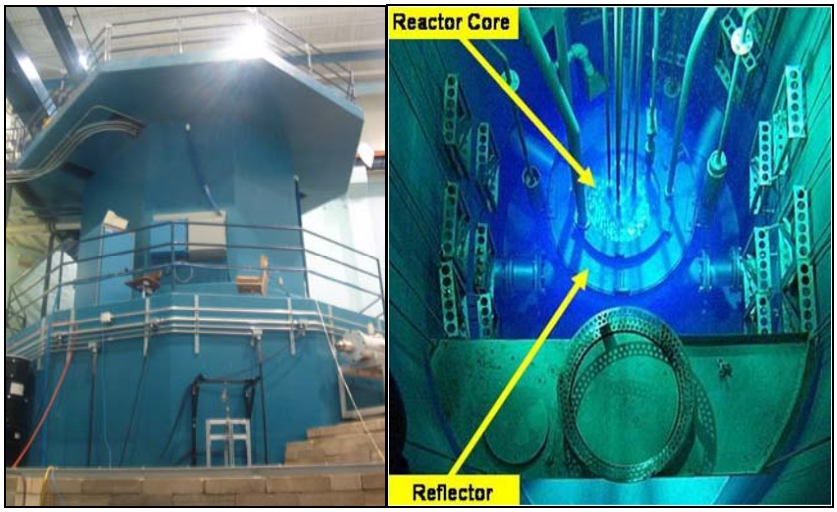

Figure 3.1: Mark II TRIGA research reactor.

The reactor core and surrounding pool are within the containment bay at the Nuclear Engineering Teaching Laboratory at the J.J. Pickle Research Campus of The University of Texas at Austin. The UT-NDP facility is located at beam port 2 of the reactor facility. Beam port 2 is a tangential beam to the reactor core. This helps to ensure a more thermalized neutron spectrum than if the beam was directed radially into the core.

The total length of beam port 2 is 300 cm. The beam port consists of two different stages with different inner diameters. The first stage of the beam port extends 160 cm from the reactor core to the beginning of the second stage. The second stage of the beam port begins at the end of the first stage and extends 140 cm to the beam port exit.

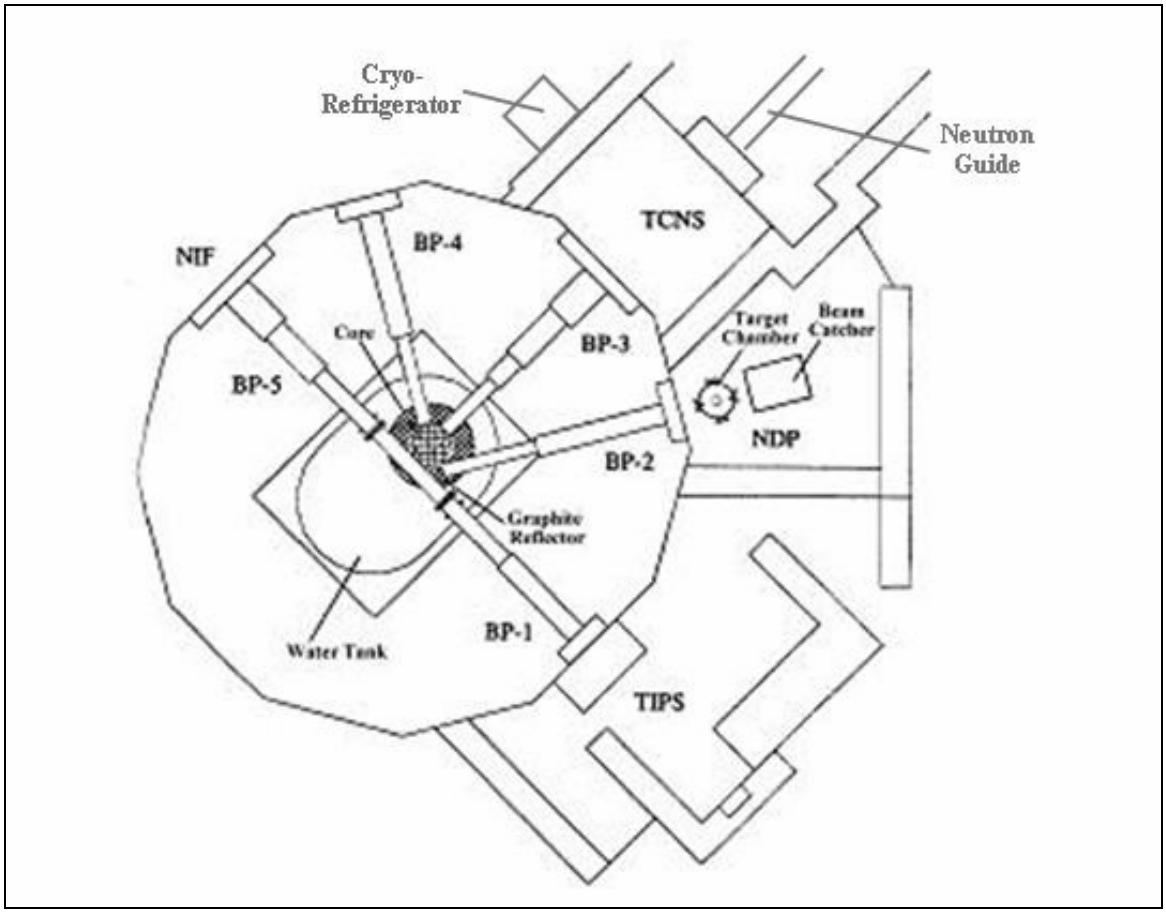

Figure 3.2: Beam port diagram for TRIGA reactor.

Neutron Beam Collimation

The neutrons exiting beam port 2 of the reactor facility are collimated to ensure proper sample irradiation and to decrease the gamma and fast neutron flux. The

collimation system for the beam begins at the beginning of the second stage of the beam port and extends the entire 140 cm of that stage.

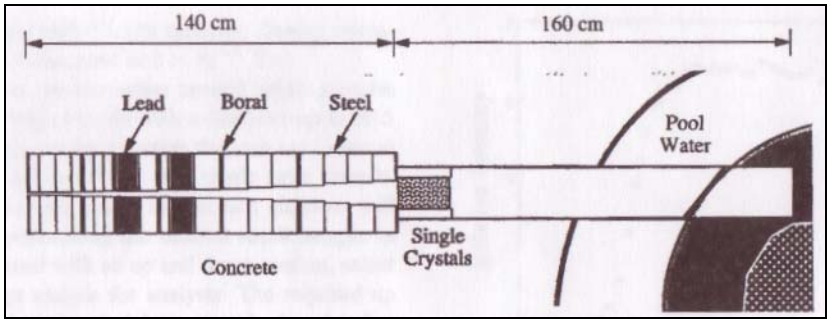

Figure 3.3: Two-stage design of beam port 2 [39].

The neutron beam from the reactor core is collimated using a system of annuli composed of lead and steel [39]. The inner diameters of the annuli vary from 6.5 cm to 1.6 cm. Sheets of Boral have been set in between some of the steel annuli. At the exit of the collimation system there is a steel aperture that determines the size of the exiting neutron beam. A 1.9 cm aperture was used for the NDP experiments relevant to this paper.

A sapphire crystal located at the end of the first stage of beam port 2 is used to decrease the fast neutron and gamma flux that passes through the beam port. The total neutron cross-section, σ_t, of the sapphire (Al_2O_3) is in the range of a few barns for incident neutrons with energies higher than about 1 eV. However, neutrons at energies less than 0.1 eV see a much lower total cross section from the sapphire since coherent Bragg scattering is disallowed in this energy range [40]. Consequently, while a large majority of the thermal neutron flux is able to pass unaffected, the fast neutron flux is significantly reduced through the sapphire.

The thermal equivalent neutron flux from beam port 2 of the UT-TRIGA reactor at 950 kW is 1.24×10^8 neutrons cm^{-2} s^{-1}. The fast neutron flux at the same reactor power

is 4.23 x 10^5 neutrons cm^{-2} s^{-1}. Calculations and details to the experimental determination of these flux values may be found in a previous report by the author [25].

UT-NEUTRON DEPTH PROFILING FACILITY

NDP at The University of Texas was started in 1994 by Unlu and Wehring [39]. The facility was established and operational until beam port difficulties occurred in 1999 that prevented any further operation of the facility. The UT-NDP facility was then disassembled while maintenance of the reactor was being performed.

The UT-NDP system was restored in 2005 and test analysis of boron doped silicon and borosilicate glass samples were performed. New components to the system since its original debut in 1994 include silicon surface barrier detectors, the turbomolecular vacuum pump, ion gauge, convection gauge, high voltage bias supply, pre-amplifier, amplifier, electronic vacuum feed-through, and the motorized sample holder. Additional modifications added to the system during this research include a new sample mounting system, neutron beam shutter, an additional detector mount, a ^{3}He neutron monitor, and a gas purge system.

Target Chamber

The target chamber for the UT-NDP facility is shown in figure 3.4. The chamber is constructed from aluminum. The diameter of the entire chamber is 41.5 cm. The chamber consists of four identical flanges with each pair of flanges creating perpendicular pathways through the target chamber. The inner diameter of these upper flanges is 8.9 cm. The windows of these pathways are covered in 0.13 mm thick aluminum so that the chamber may be evacuated without causing noticeable neutron

interference. The other two large flanges that are not in use for the NDP facility are sealed off with thick aluminum caps. The caps are removable if necessary.

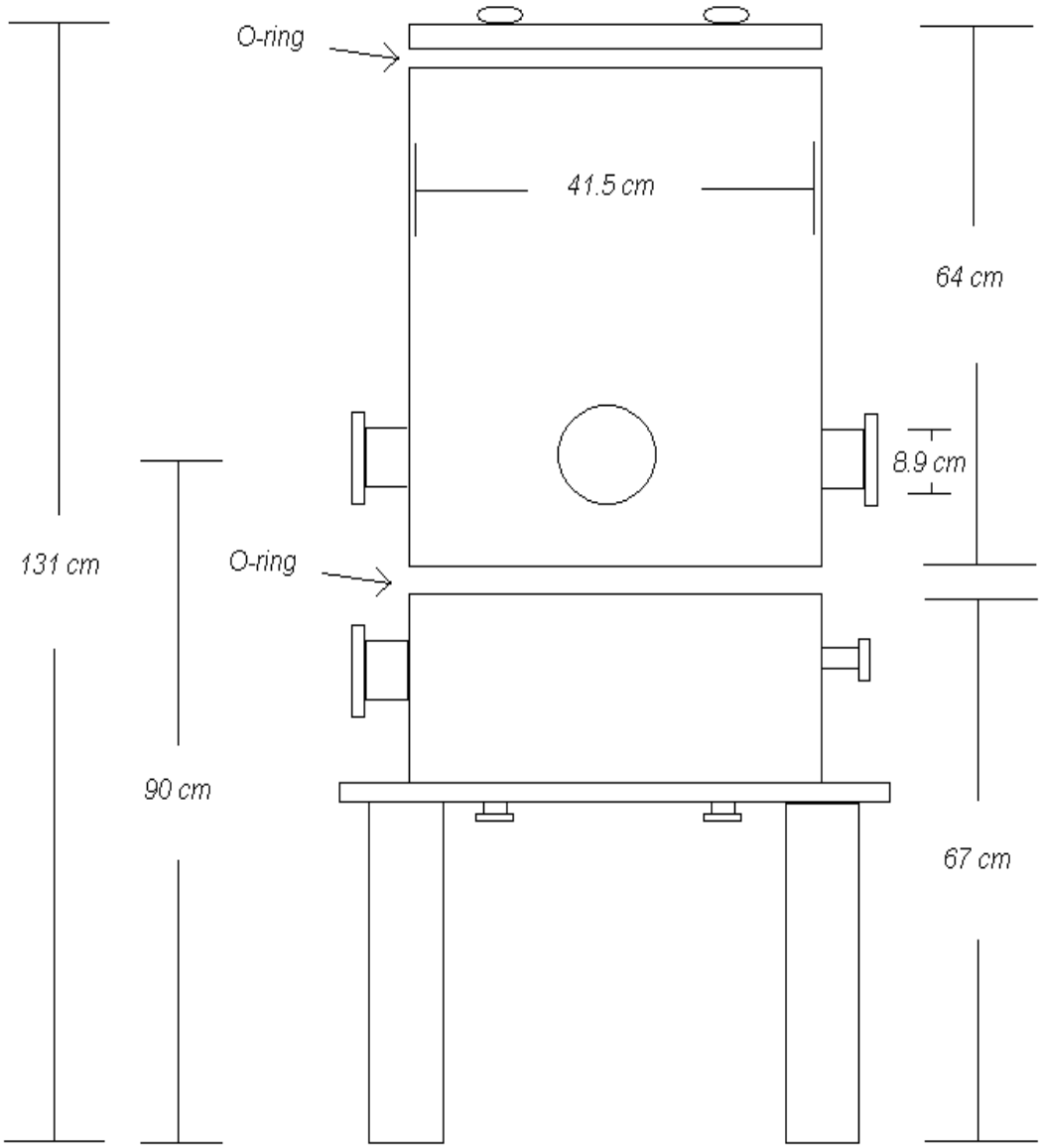

Figure 3.4: NDP target chamber diagram.

Two other small flanges are opposite one another below the neutron beam flanges. The ion gauge utilizes the smaller of these flanges. The turbomolecular vacuum

pump is connected to the opposite larger flange via a bellows. The walls of the target chamber are 0.64 cm thick. The top of the chamber is covered with an aluminum lid that has a 6.4 cm inner diameter quartz viewing window in its center. The lid to the chamber is not connected to the chamber in any way other than the force of vacuum and gravity. The ion gauge, turbopump, top cover, and bottom electronic feedthroughs are all joined to the chamber with O-rings that help to allow a vacuum seal to be reached.

The bottom of the chamber has a series of small flanges that allow for electronic feedthroughs, gas purging, and a convection gauge. The total height of the target chamber from the base to the top cover is 131 cm.

Figure 3.5: Picture of NDP Chamber Lid.

Vacuum System

The vacuum system for the UT-NDP facility pumps down the pressure of the entire target chamber to 5 x 10^{-6} torr. It is often necessary to maintain this pressure for extended periods of time such as two or three weeks. The seals to the target chamber where the cover and pumps meet with the chamber are simple O-rings. In order to achieve the desired vacuum the O-rings must be properly greased and extremely clean. It is also necessary to ensure that materials inside of the chamber while being evacuated are clean and not highly susceptible to out-gassing.

The facility uses a Leybold Trivac roughing pump to pump the target chamber to a pressure of approximately 10^{-3} torr. Pressures at this magnitude are measured with a convection gauge attached to a flange on the bottom of the chamber. The convection gauge is monitored with a 275 Granville-Phillips convection gauge controller.

After the roughing pump brings the chamber to a pressure below 13 mtorr, the Turbotronik NT10 Turbopump is turned on to begin pumping the system to 5 x 10^{-6} torr. An ion gauge that is connected to the small, lower flange on the target chamber monitors the pressure of the facility. The ion gauge is controlled and monitored by a 307 Granville-Phillips vacuum gauge controller.

When in operation the turbopump can generate microphonic noise that is spread over the entire system and can be seen with an oscilloscope to influence the detector signal. To eliminate this problem the turbopump was separated from the system by a bellows. Additionally the bellows is weighted by lead. The bellows helps to dampen the microphonic noise and reduce the signal deterioration to a reasonable level.

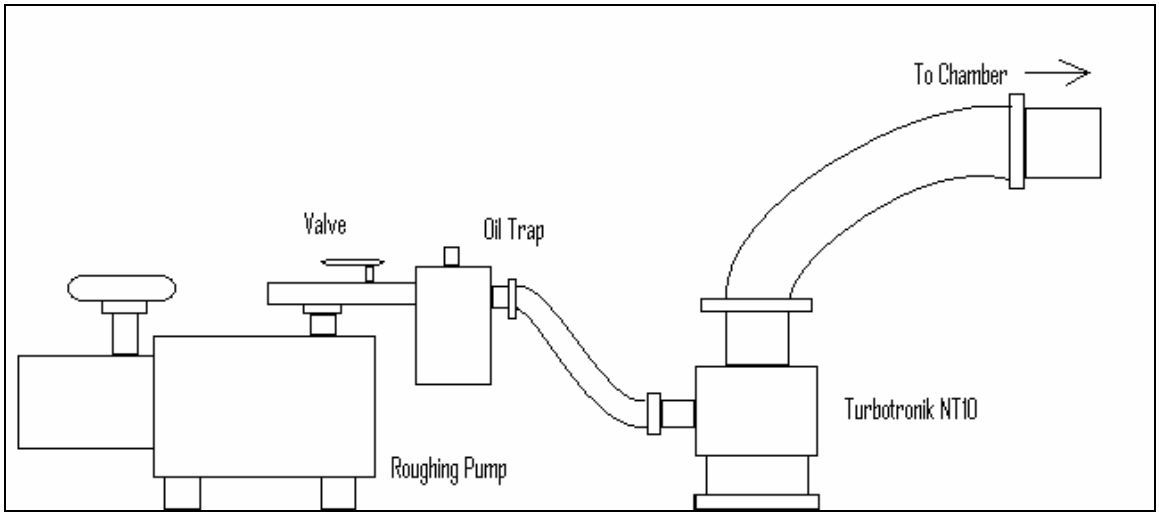

Figure 3.6: Diagram of NDP vacuum system.

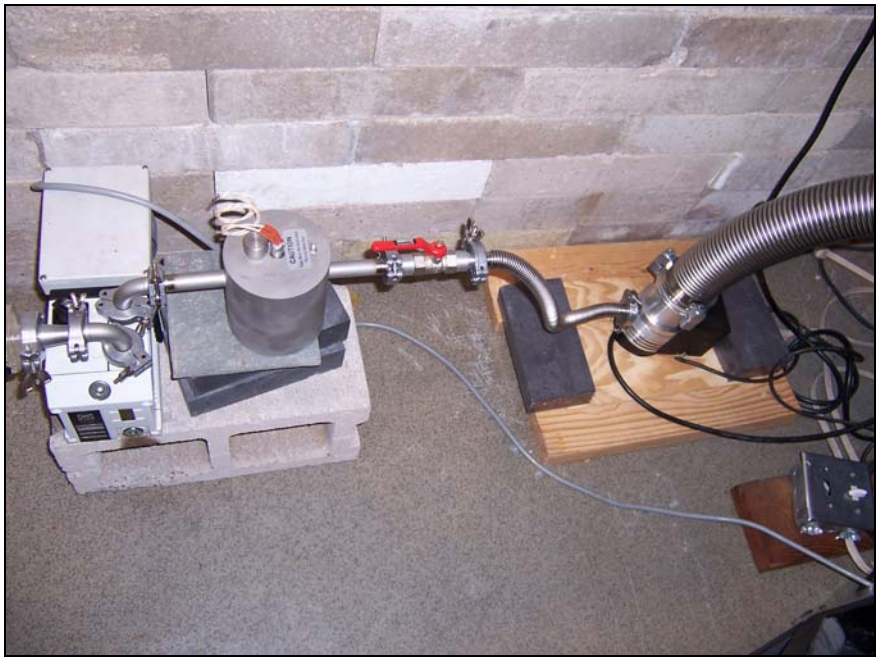

Figure 3.7: Picture of NDP vacuum system.

Electronics

Accurate profiling of low energy charge particles (< 1000 keV) requires that the low energy background noise be minimized to prevent signal interference and large dead

times. This requires that the counting system not amplify unnecessary noise from the detector more than necessary or introduce any extra noise from the electronics.

The alpha counting system for the UT-NDP facility is shown in figure 3.8. The silicon surface-barrier detector is operated within the chamber to record the pulse spectrum of the incident charged particles. The signal is transferred to the pre-amplifier through a microdot cable that exits the vacuum chamber via a shielded electronic feed-through. It was determined that an unshielded feed-through was prone to picking up excessive electronic noise due to its close proximity to the aluminum target chamber. The problem was solved by purchasing a coaxial feed-through that had a Faraday shield surrounding the coaxial cable and a ceramic joint to the chamber. Transmission from the feed-through to the pre-amp is through a RG-62, 93 Ω coaxial cable no longer than 6 inches in length.

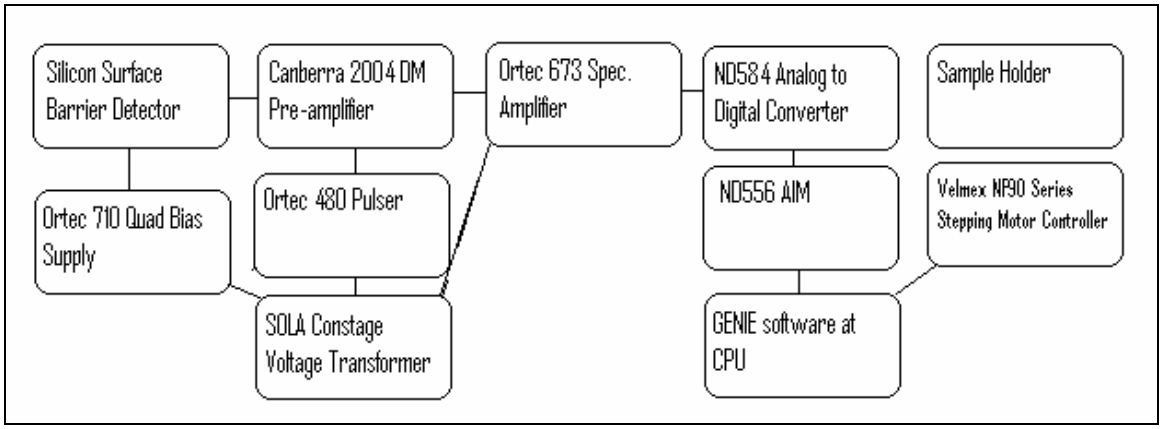

Figure 3.8: Diagram of the NDP electronics.

The system electronics are powered with a constant voltage supply that helps to eliminate a large portion of the noise from outside electrical sources. A pulser is used during experimentation to check the linearity of the ADC, ensure that no energy shifting is taking place, and to observe the integrity of the signal.

The Canberra pre-amplifier is operated at the low-gain setting to minimize any amplification of low-level noise that may occur from the detector or cable between the detector and pre-amp. The signal is transferred from the pre-amplifier to the amplifier and then to the analog to digital converter (ADC). The ADC converts the signal so it can be digitally read. The AIM buffers the signal until the CPU can process it. The ADC also monitors the dead time of the system.

GENIE software is used to interpret the incoming digital signal and record an alpha spectrum. The CPU is also utilized to run a terminal that feeds commands to the Velmex Stepping motor controller. The controller is used to choose the sample and the sample's position.

Sample Holder and Detector Mount

The sample holder for the system shown in figure 3.9 is capable of holding up to 8 samples at a time. The main advantage of this mount is that analysis of 8 separate samples may be performed without having to break the vacuum of the target chamber. Changing the sample itself is not time consuming, however having to release the vacuum and then pump the chamber down again to 10^{-6} torr can take approximately 6 to 8 hours. Therefore, there is a considerable advantage to loading all of the samples to be analyzed at the same time.

The sample holder is circular as seen in the figure below. It is made of aluminum alloy 6061 and has eight circles lining the perimeter of the circle and one in the center. Each circle has a small aluminum clamp above it. The clamp is used to hold the thin aluminum plates that the sample are mounted on. The sample holder can be rotated to move the samples up or down vertically as little as one-thousandth of an inch along the circumference of the mount. The reproducibility of sample positioning was analyzed with neutron radiography to ensure that accurate alignment with the neutron beam could be

relied upon. It was found that the stepping motor was accurate to one-thousandth of an inch within its movement of the sample. The holder was controlled via command code input to the computer that would talk to the Velmex controller already mentioned. The motor and mount are shown in figure 3.10.

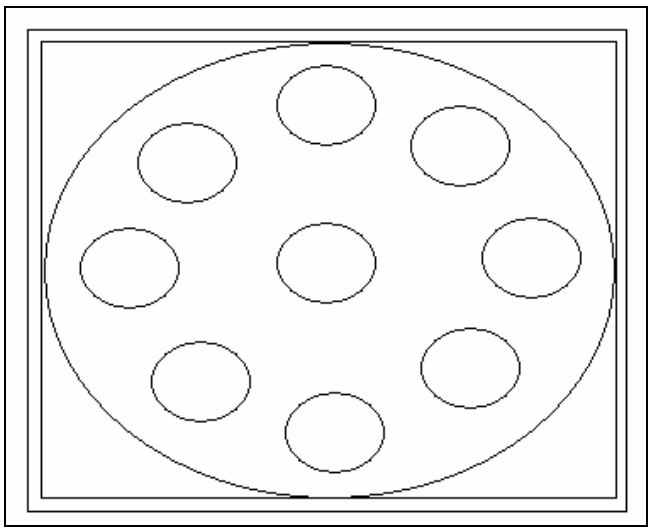

Figure 3.9: Diagram of sample mount.

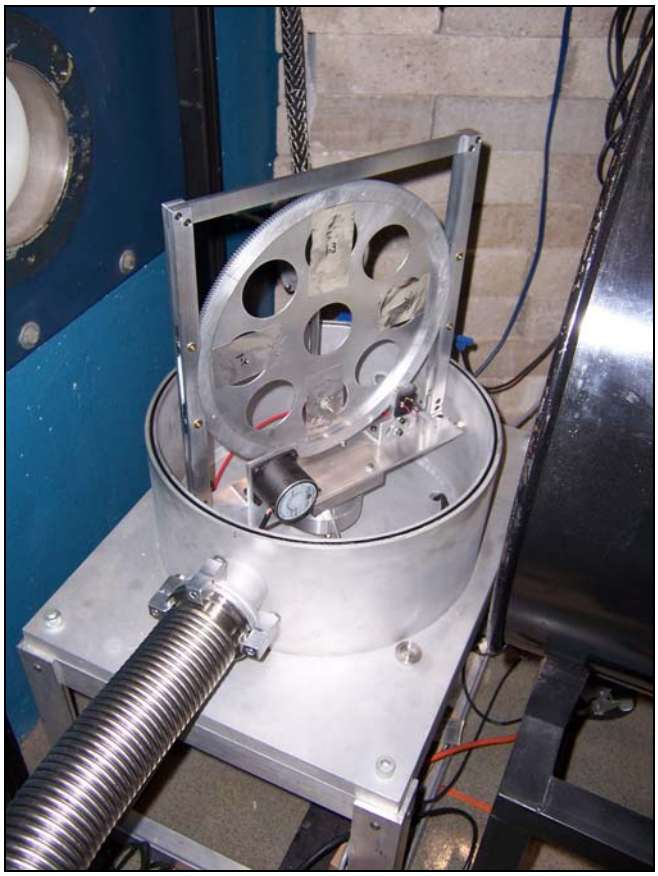

Figure 3.10: Picture of sample mount.

The detector mount is comprised of three main pieces: the detector holder, the stand, and the mobile platform. The mobile platform is the base of the mount that holds the stand. It is designed so that it can be moved in the radial direction from the sample to increase or decrease the distance from the detector to the sample. The mount may also be swiveled angularly with respect to the sample to increase or decrease the angle between the detector and the sample normal.

The sample stand is simply a set of two aluminum rods set together in such a manner that the height of the detector may be adjusted. The detector holder is machined from a non-conducting material to allow the ground of the detector to exit through the microdot cable and not ground itself to the mount. The holder has three set-screws to accommodate a tight fit to different size detectors that may be used.

Initially the detector holder was constructed of aluminum, however grounding issues with the surface barrier detector required that we design a new mount. The redesigned detector mount shown in figure 3.11 is fabricated from plastic to prevent any ground loops between the detector and the chamber.

Figure 3.11: Picture of detector mount.

GENIE Software

The GENIE software was used for interpreting the digital signal from the ADC. GENIE bins the incident signal into a selected number of channels. These channels are later calibrated so they can be transformed to energy. The software also allows for real time analysis of alpha peak FWHM and also can be preset for specific acquisition times while accounting for system dead time.

FACILITIES AND NDP MODIFICATIONS FOR BATTERY RESEARCH

Specific facilities and modifications to the UT-NDP facility were required to complete the lithium ion battery research of this report. Much of the research performed was done at the lab of the John B. Goodenough research group. This lab contained the proper instrumentation and materials for the preparation of the cathode films and fabrication of the lithium ion cells.

The primary tools used at the Goodenough lab were,

- MIG welder for tacking mesh to cathode can
- Lithium ion battery materials
    - Cathode, anode cans
    - Lithium ribbon and spacers
    - Oxides and carbon black
    - PTFE, PVDF binders and separators
    - Titanium mesh
    - DEC and lithium salt electrolyte
- Engraving tool - for battery labeling
- Mortar and pestle - for mixing oxide, binder, and carbon
- Argon glovebox – argon environment for working with lithium and assembling cells. Was also equipped with specialized punch tool for sealing cells.
- Arbin battery cycler – used for charging/discharging cells with precision current. A CPU was used to control the Arbin cycler while also monitoring and recording data such as current, voltage, capacity, and energy of the cell.

Modifications to the UT-NDP facility were necessary to be installed to better accommodate the electrode samples. These modifications include,

- Gas purge system – A gas purge system was installed that allows for the NDP chamber to be filled with a gas rather than air. The system installed allows for a gas

cylinder to be kept outside of the beam port 2 radiation area while still being connected to the chamber. There is a ball valve connected to one of the small flanges beneath the NDP chamber that can be opened before purging the system. The gas purge system was installed to minimize the type spent by the anode materials exposed to oxygen. While the cathode materials are stable, the anode materials contain lithium that can form oxide layers. The preferred gas to be used for chamber purging in this case is argon since nitrogen could lead to nitride layers forming on the anode as well.

- Additional detector mount – A second detector mount was fabricated and installed to allow for the use of more than one detector at a time. This allows for profiling of two different surfaces simultaneously, or for profiling of the same surface at different angles. The low ^{6}Li concentrations of the anode samples profiled for this research were the motivation for the installation of this component.
- Aluminum sample mount plates – Plates of aluminum alloy 6061 that are 1 mm thick were used as sample mounting plates for this research. The plates had holes drilled through the middle where the sample would be placed to reduce the mass seen by the neutron beam and to allow suction to be applied that can flatten the samples. The plates were attached to the aluminum rotating sample holder by small clamps that are riveted to the sample holder. The primary need for the sample plates and clamps was to ease the process of sample changing and to produce a method with more repeatable geometry.
- Neutron shutter – A mechanical neutron shutter was installed to increase the radiation safety of the beam port 2 area. The neutron shutter consists of polyethylene, boral (boron between 2 aluminum plates), cadmium, and Lithoflex material. The shutter is controlled by a switch outside of the beam port 2 area that vertically brings the shutter into the open or closed position. A linear actuator moves the shutter. If the user needs to enter the beam port 2 facility during reactor operation, an additional beam port plug may be installed prior to reactor start-up. If the lead shutter, the beam port plug,

and the neutron shutter are all in the path of the neutron beam then the beam port 2 area has been found to meet health physics standards to enter the area for short durations (<10 minutes).

The entire UT-NDP facility is shown in figure 3.12. Cement blocks surround the NDP facility to meet standard health physics regulations during reactor operation.

Figure 3.12: Picture of NDP facility.

Chapter 4: Experimental Methods

NDP analysis of the lithium ion cell electrodes involved three primary steps for the lab cells. After being taught the correct method for the cell preparation by post-doctoral students in the Goodenough lab, I personally performed each of the steps in the following process either at the Goodenough lab or at the Nuclear Engineering Teaching Facility.

The first step was to make the cathode compositions and the actual lithium ion cells. Secondly, the cells needed to be exposed to various conditions including cell cycling, charging variations, and different aging lengths at temperature. Finally, the cells were disassembled and electrode samples were removed and prepared for NDP analysis. The fabrication and exposure of the cells took a duration of anywhere from 3 days to 3 weeks per cell depending on the charging rate and availability of the cycling machine. NDP of the cell, including cell disassembly, required an additional 4 to 60 hours excluding data analysis.

The commercially manufactured cells only required the final two steps of those mentioned. Commercial cells, while more readily available and easier to analyze, were not the primary focus of this research for two primary reasons. The first is that these cells cannot be accurately cycled with precision current due to limitations of the Arbin battery cycler used. Secondly, these commercially manufactured cells use compositions such as $LiCoO_2$, $LiFePO_4$, or $LiFePSO_4$ that are highly researched and were not of particular interest to the John B. Goodenough research group.

ELECTRODE PREPARATION AND CONDITIONING

The first step to prepare the entire cell was to make the cathode films. The compositions of the cathode films made and analyzed for this research are as listed in table 4.1. The mixture from which the film is made is 75% oxide material, 20% carbon black, and 5% PTFE. The oxide material is pre-made in larger amounts for consistency throughout experimentation. The carbon black is used mainly for electrical conductivity throughout the electrode. The PTFE, poly(tetrafluoroethylene), is a synthetic fluoropolymer that acts as a binder for the composition.

Table 4.1: Breakdown of cathode composition.

Composition	**$LiCoO_2$**	**$LiNi_{1/3}Mn_{1/3}Co_{1/3}O_2$**	**$LiFePO_4$**
75%	$LiCoO_2$	$LiNi_{1/3}Mn_{1/3}Co_{1/3}O_2$	$LiFePO_4$
20%	Carbon black	Carbon black	Carbon black
5%	PTFE	PTFE	PTFE

To prepare the films, the oxide and the carbon black are weighed out and combined with a mortar and pestle. After being well mixed, the binder (PTFE) is added and the mixing process is repeated. Then it is necessary to add two to three drops of isopropyl alcohol to the mixture. This helps to turn the powdered mixture into a slurry that can be continuously folded and flattened with the mortar and pestle until the entire product is a tight rectangular block.

Then the combination is flattened and placed between two thin pieces of parchment paper. The block is rolled very flat with a heavy rolling tool. The block should be flattened until it is a film thin enough such that small circles of less than 0.008 g may be punched out without any visible defects. The punch used to cut out the cathode films

is 8 mm in diameter. The resulting cathode films are circles 8 mm in diameter, approximately 0.008 g in weight or less, and approximately 80 μm thick. The prepared films are cut and left to dry in an 110ºC oven for a minimum of overnight to allow for them to dry. The next step is to prepare the cell.

CELL PREPARATION

Preparation of the coin cell lithium ion batteries begins by inscribing the cathode can of each battery to be made. Each battery will have an anode can that is in contact with the anode, and a cathode can that is in contact with the cathode. The cathode can is inscribed in order to keep track of the exact cathode film that it contains.

The next step is to weigh the cathode films that were dried in the oven. Each cathode weight must be recorded in order to calculate the cell capacity. Once each weight is recorded, it is typical to tack on a titanium charge collector to the inside of the cathode can. Then the cathode film would be set onto this titanium charge collector. However, it was necessary to eliminate the titanium charge collector from the cell since the nature of this study is to form depth profiles of the cathode films, and the titanium charge collector is a fine mesh. The mesh would not have allowed for a flat sample in the end. Instead, the cathode film is placed in direct contact with the cathode can. There has been no noticeable effect on cell performance due to this measure.

At this point the cathode cans along with the films are ready to be placed in the argon glove box where the remainder of the assembly will take place. The glove box is a complete argon environment and is required due to the pure lithium anodes that are used in the cells. Once the glove box is sealed then assembly can begin.

First, lithium circles nearly equal to the size of the anode can are punched out; these will be the anodes for the cells. The anodes are approximately 18 mm in diameter.

One should then flatten the anodes with a non-stick surface. Generally Teflon is used since it does not adhere to the lithium. The flattened anodes are set aside.

Next, several drops of electrolyte solution should be dropped into the cathode can until the entire cathode film is covered. The electrolyte solution is diethyl carbonate (DEC) with dissolved lithium salts. Once the electrolyte has covered the cathode then two PTFE separators can be dipped in electrolyte solution and then placed over the cathode. The separators are similar in thickness to the cathode in the range of 70 to 100 μm. The separators act to prevent any contact between the cathode and anode that would result in a short circuit of the cell.

After the separators have been carefully placed into the cathode can to where they cover the cathode film without having moved it towards the cathode can walls, then more electrolyte solution may be added. The next step is perhaps the most critical. One should place one of the lithium anodes on top of the separators while taking care not to let the anode touch the cathode can walls. This can also result in a short circuit if it is not fixed before the cell is sealed.

After the anode has been placed on top of the separators then two lithium spacers need to be placed on top of the anode. The lithium spacers help to ensure sound electrical conductivity between the anode and the anode chamber. More electrolyte solution may be added once the spacers are in place. The solution should be added to a level near the top of the cathode can.

The next step is to carefully place the anode can on top of the entire assembly. The anode can should fit snugly into the cathode can. This can be tedious, as it needs to be achieved without disturbing the structure of the assembly. After the anode can is in place, the entire cell should be moved to the punch with the anode facing up.

The punch is also located within the argon glove box. Its use is to seal the cell to prevent any oxygen from reaching the contents within the anode and cathode cans. The contacts of the punch should be cleaned before use to prevent any grease or dirt from

coming into contact with the cell. Once the punch is clean, the cell is placed on the center contact and the punch is lowered very quickly to seal the cell. After this step is repeated for each cell, the area may be cleaned and the cells may be taken outside of the argon environment.

The final step in the cell preparation is to measure each cell voltage with a multimeter. If a reasonable voltage above ~1.3 V is not found then the cell was not prepared correctly and the process must be repeated. The process of making the cathode film takes about 2 to 3 hours, and then it must be dried overnight. To prepare the cells I had to wait for the glove box to become available, as it could only be used once per day. Once I had use of the glove box, cell assembly takes about 2 to 3 hours as well. Typically, the entire process of making the cells was a 2-day procedure.

METHODS OF CELL CONDITIONING

The cells of this study, either commercial or lab made, were conditioned by various methods in order to determine if any variation in lithium distributions within the anode or cathode may be seen and to what degree. The methods of cell conditioning include:

- Storage of cells at temperature.
    - Commercially manufactured cells are stored at a temperature of 50ºC, and removed for analysis after specific storage times.
- Cell cycling
    - Lab cells are charged/discharged a specified number of times varying from 1 cycle to 100 cycles.
- Variable charging rates and states of charge
    - Lab cells are charged/discharged at various currents and left in states of charge or full discharge.

For the convenience of the reader, each method of cell conditioning will be described in detail preceding the experimental results of that method.

The latter conditions were chosen because,

- They are the focus of other studies in electrochemical research [3, 4, 36, 41].
- They represent conditions that may have the greatest effect on the lithium distribution within the cathode, and are therefore most important to NDP.
- They were reasonably achievable with the instrumentation available at The University of Texas at Austin.

SAMPLE PREPARATION

The cells were conditioned according to one of the methods listed in the previous section. In particular, the lab cells were conditioned by variable charging rates and state of charge, as well as cell cycling. The commercial cells were conditioned by the storage of cells at temperature. Disassembly of the cells varied by the type of cell. The lab cells were all of the coin cell variety, whereas the commercial cells were of both the coin cell and cylindrical cell type. Both varieties are shown in figure 4.1.

Figure 4.1: Lithium ion coin cell (left). Lithium ion cylindrical cell (right).

Disassembly of both varieties of cells was done in a glove box in an argon environment. The argon environment is necessary due to the oxide layers that may be formed with unstable lithium on the anode. The only time when the argon environment was not necessary was when the anode was not to be used for analysis. It is not problematic to expose the cathode to air since the lithium within the cathode structure is stable.

The coin cells were easily opened with pincers and a pair of pliers. If the cell was charged then it was necessary to cover the anode can with electrical tape to prevent short-circuiting the cell and causing discharge. This was not necessary for the discharged cells.

Once opened, one may see that the commercial cells have a roll of electrode and separator material inside the cell can as shown in figure 4.2. The roll is used to maximize available electrode surface area, thereby decreasing the internal resistance of the cell and increasing capacity. The lab made cells simply have a single cathode film as previously described.

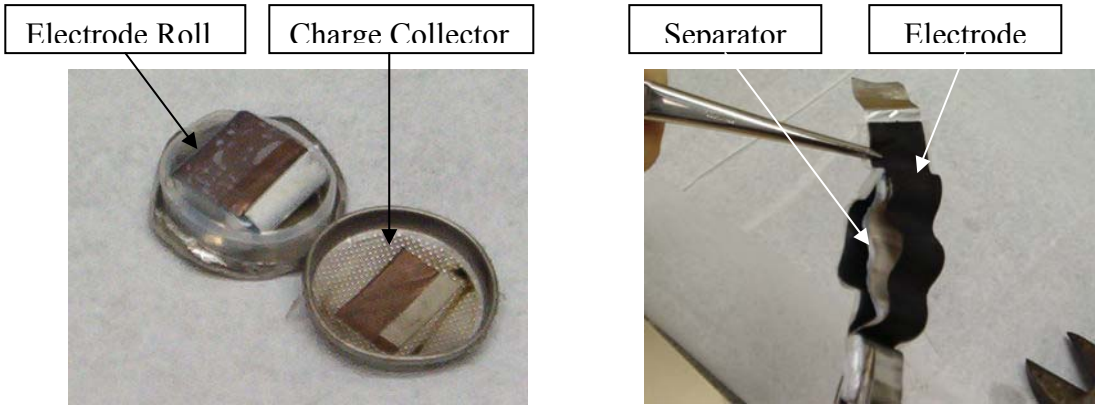

Figure 4.2: Opened commercial coin cell (left). Layers of electrode and separator inside the cell (right).

To retrieve the electrode materials from the commercial coin cells, the roll can be unwound, and the layers of anode, separator, and cathode can be separated. Distinguishing the anode from the cathode is quite simple; the anode is plated onto a copper charge collector while the cathode is plated onto an aluminum charge collector. The charge collector is coated on both sides with the electrode material, but they should still be easily distinguishable. Small sections of each electrode are then cut from an inside layer of the cell, making sure that the anode and cathode sections were directly opposite one another in the cell. This helps to ensure that the electrodes were effectively sharing the same lithium ions.

The cathodes that were removed from the coin cells were rinsed with diethyl carbonate (DEC) to remove any remaining salts and electrolyte solution [3]. Then the films were dried overnight. Once the films were dry, the commercial cathodes were cut into sections. This was not necessary for the lab-made cathodes due to their small size. Similar treatment was performed for the carbon anodes of the commercially made cells.

Opening the cylindrical cells was much more difficult and required a pipe cutter and hacksaw. Each end of the cell was cut off with the pipe cutter, and then the exterior casing of the cell was removed using the hacksaw. After this point is reached, the procedure for removing and rinsing sections of electrodes is the same as that just described.

SAMPLE MOUNTING

The electrodes were mounted onto thin aluminum plates that were 1 mm in thickness. Each plate has a grid of 3 mm diameter holes. After mounting the samples, light suction is applied to the back of the plate to flatten the samples against the plate without direct contact to the sample surface. Thin strips of scotch tape are used to secure the sample against the plate. The samples are secured over a previously marked spot on

each plate that will be in the center of the neutron beam. A Teflon mask with a 6.35 mm (0.25 inch) diameter aperture is secured over the sample with small strips of double-sided tape. The area of electrode being analyzed is limited to 0.32 cm^2.

Each plate is labeled, recorded, and then mounted onto the large aluminum sample holder for the NDP system. The plates are mounted to the sample holder by small aluminum fasteners. Outlines of each plane are drawn onto the sample holder to ensure that the same geometry is used each time. This method is used so that individual samples may be replaced without disturbing the geometry of the entire system by removing the sample holder each time.

NEUTRON DEPTH PROFILING OF ELECTRODES

Before beginning a charged particle count, the NDP chamber that contains the samples and the detector must be at a pressure of approximately 5 x 10^{-6} torr before analysis may begin. The vacuum is necessary in order to prevent energy loss of the charged particles in the air between the sample and the detector. Also, the vacuum is required before the high voltage bias supply may be applied to the surface barrier detector in order to prevent damage. It is generally necessary to turn on the turbopump for at least 1 to 2 hours before proper vacuum levels can be achieved.

The vacuum level within the chamber is monitored with the ion gauge mounted beneath the target chamber. The ion gauge controller mentioned in the earlier electronics section displays the pressure within the chamber. The ion gauge should not be powered on until the turbopump has been in operation for at least 30 minutes and the convection gauge controller displays its minimum pressure of 0 mtorr.

Sample Mount

The stepping motor responsible for rotation of the sample mount is controlled through an interface on the CPU. The interface is the online edition of the Velmex 90 controller. It is user-friendly and is equipped with a help manual. To control the motor the controller interface must be opened on the CPU. Set the rotational motor to "motor 1" of the Velmex system and bring the controller online. The motor's movement can be set in units of length or "steps". For the purposes in the NDP chamber, it is set to steps. The number of rotational steps from one sample position to another is 1037. The precision of this rotation is to one thousand of an inch. A full rotation of the sample mount is 8300 steps.

Charged Particle Counting

Once the correct vacuum level is achieved and the sample positioning is correct, the neutron shutter is raised and the lead shutter is opened. The bias voltage to the surface barrier detector can then be increased to the specified voltage of that detector in table 4.2.

Table 4.2: Detectors and supplied bias voltage.

Detector	Voltage (V)	Specific Capacitance (pF/mm^2)	Active Area (mm^2)	Sensitive Depth (μm)
TB-015-50-150	11	0.75	50	105
TU-013-100-100	25	1.1	100	100

Sample analysis for the electrodes can require up to 60 hours depending on the sample type. Anode samples typically had lithium concentrations in the range of 2×10^{15} to 3.5×10^{16} atoms cm^{-2} and required longer counting times. Cathode samples had lithium concentrations of 1×10^{17} to 3.0×10^{17} atoms cm^{-2}. The low neutron cross-section, 940

barns, and the small atomic abundance of ^{6}Li (7.5 %), resulted in low count rates for the samples. It was not unusual to have on average 40 to 80 counts per channel for an 8-hour analysis at the UT-NDP facility. Count rates for the different electrode samples ranged from 0.001 to 0.007 counts sec^{-1} $channel^{-1}$ when the 100 mm^2 active area detector was being used.

The geometry of the detector was always set such that the detector was directly facing the sample. No angle was set between the detector normal and the sample normal since maximum depth resolution was not the objective. The detector was set at 7 cm from the sample surface. The gain was held constant at 50x throughout the experimentation for this study. Timing constants for the amplifiers were set to 1.0 μs for the Ortec ULTRA detector, TU-013-100-100. The timing constant on the amplifier was changed to 0.5 μs for the Ortec Series B detector, TB-015-50-150. Dead-time for the system was not a significant factor

Each energy spectrum was counted over 4096 channels set by the ADC and the GENIE counting software. The GENIE software forms an energy spectrum in real time according to the incident signal from the detector. Recording the spectrum at this low-energy/channel allows for different binning of the channel data during data analysis so that it may be optimized. In retrospect, it would be advantageous to operate the NDP system using 2048 channels to optimize statistics.

Preceding any other sample measurements, an energy and concentration calibration of the NDP system should be performed as described in the energy calibration section. At any point before changes to the experimental setup is made, a background spectrum must also be recorded.

Once the calibrations have been performed then sample analysis may begin. Start and stop the spectrum acquisition and the ^{3}He neutron monitor at the same time. The neutron monitor gives a better measure of neutron flux seen by the sample than assuming

a constant flux for a specific duration of time. The neutron flux was not seen to vary by more than 2%.

Spectrum Analysis

Details of routine analysis performed on each energy spectrum are delineated in the following sections. These include the energy and concentration calibrations, profile formation, and error analysis.

Energy Calibration

The SRM 93a sample with uniform ^{10}B (B_2O_3) distribution throughout a 6 mm thick Borosilicate was used for alpha energy calibration. This sample provides 2 points of alpha calibration and is also useful for resolution measurement of the system for alphas.

A separate energy calibration must be performed for the triton particles since the detectors have thin surface deposits on their faces and the alphas and tritons will lose non-equivalent amounts of energy passing through them.

To perform the ^{6}Li energy calibration a $LiNbO_3$ optical grade crystal is analyzed. The 5 mm thick crystal has a step-wise energy spectrum with one point for triton energy calibration at 2727.88 keV. The second point of calibration for the triton is performed with a saran wrap sample. The saran wrap contains ^{35}Cl that undergoes a $^{35}Cl(n,p)^{35}S$ reaction when in the neutron beam. The proton from this reaction can be used for energy calibration of the triton since the stopping power of the triton is three times that of the proton. The energy of the proton from the ^{35}Cl reaction is 597.93 keV. Due to the low energy of the proton, and low reaction rate of the ^{35}Cl, this calibration is difficult and very time intensive for the UT-NDP system. A better source for a similar type of calibration may be the $^{3}He(n,p)^{3}T$ reaction although it will also require an extremely long count time.

The thick samples that were used for energy calibration standards provided step-wise energy spectra as in figure 4.3.

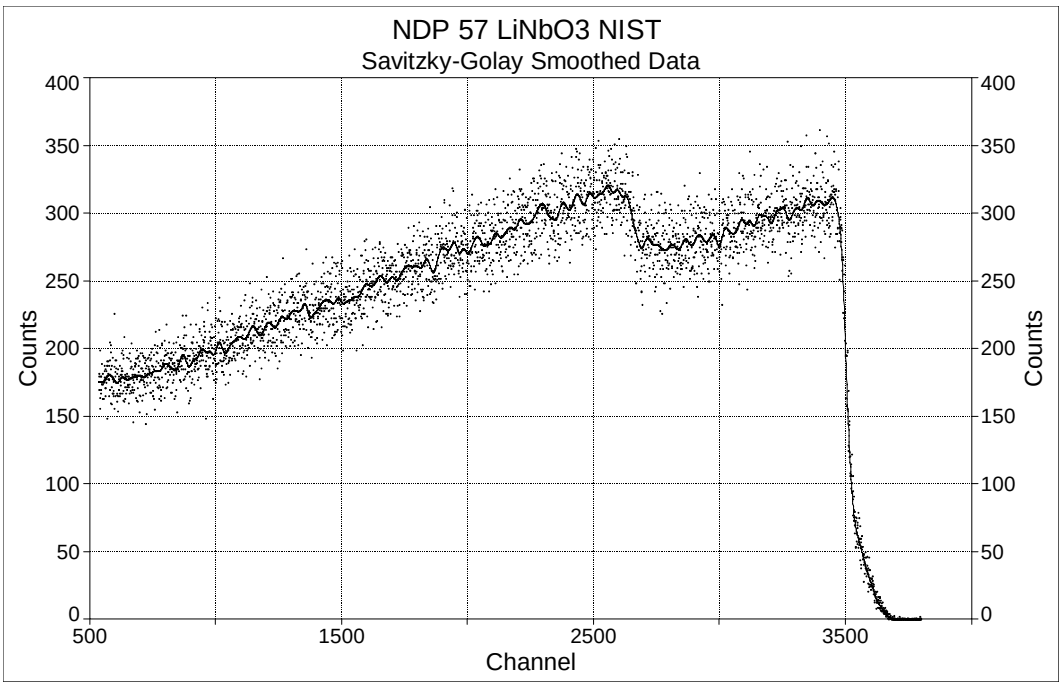

Figure 4.3: A step-wise energy spectrum from a $LiNbO_3$ crystal analyzed at NIST. The leading edge in the spectrum at channel ~3500 is the triton particle with energy 2727.88 keV.

The spectrum from figure 4.3 is from an energy calibration performed with the $LiNbO_3$ crystal. The leading edge of the spectrum at channel ~3500 is created by the counting of the triton particles. Each triton particle from that edge has originated from the surface of the sample and has energy 2727.88 keV. The spread of energies created by the detector response function and the system energy broadening creates the effect of the leading edge being spread over a number of channels. Once the data from the leading edge is smoothed, the absolute value of the first derivative of the smoothed data is taken.

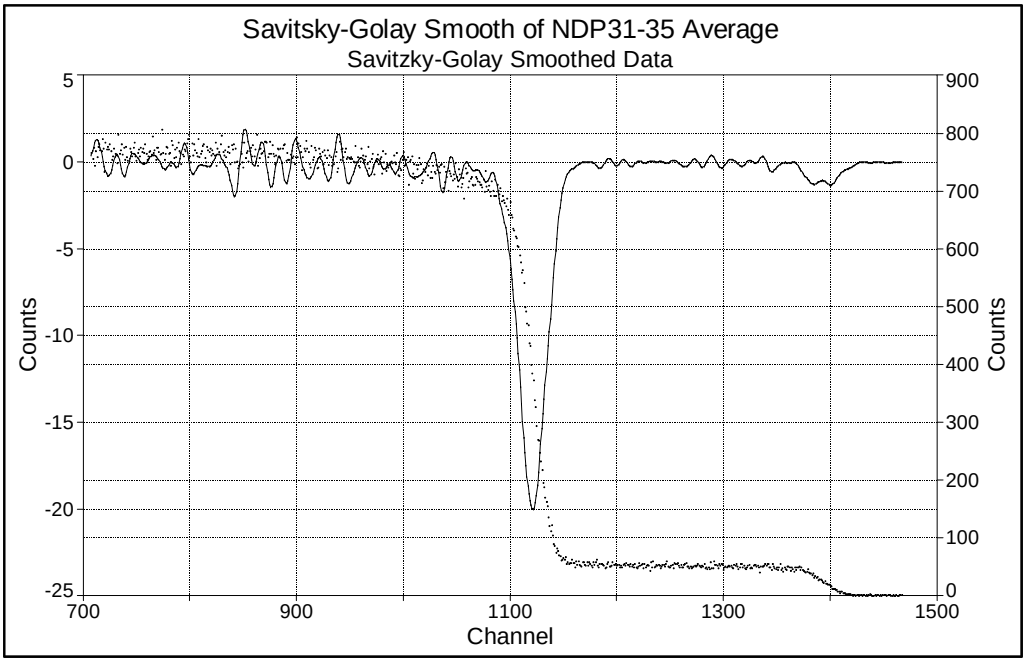

Figure 4.4: The first derivative (smooth line) of the smoothed leading edge (dotted line) for an energy calibration is shown. The spectrum here is from an alpha energy calibration.

Figure 4.4 shows an example of a differentiated leading edge. The curve of the differentiated edge is fit to a distribution using the Tablecurve 2D fitting software. A Pearson IV distribution is generally the best fit for this case. The centroid of the peak is a fractional channel number that corresponds to the energy calibration for the particle of interest. Two points of this type will provide a two-point energy calibration that should be sufficient.

The FWHM of the peak gives the energy broadening of the entire system. One can then determine the depth resolution for charged particles near the surface by using the information from the energy broadening of the system.

Concentration Calibration

The SRM 2137 is used for concentration calibration of the UT-NDP system. The SRM 2137 has retained dose of ^{10}B equivalent to 1.018 ± 0.035 x 10^{15} atoms cm^{-2}. The low concentration of the sample requires that counting times be extremely long for an accurate calibration.

To calibrate the system, the number of atoms per count in an energy spectrum needs to be determined. This is determined by dividing the atom concentration of ^{10}B in the SRM 2137 by the integrated number of counts in both alpha peaks (1471.76 keV and 1775.87 keV). One can then adjust this value by cross-section, neutron fluence and solid angle when necessary to determine the sample concentration according to equation 4.1.

$$C_{sample} = \left(\frac{atoms}{count \cdot cm^2} \right)_{std} \left(\frac{\Phi_{std.}}{\Phi_{sample}} \right) \left(\frac{\Omega_{std.}}{\Omega_{sample}} \right) \left(\frac{\sigma_{std.}}{\sigma_{sample}} \right) \sum_{i=1}^{N} (Counts_{sample})_i \ . \qquad (4.1)$$

Data Smoothing

Recorded energy spectra were smoothed with Savitzky-Golay (SG) smoothing algorithms prior to formation of the depth profiles. The SG algorithm was first described in 1964 [42] as an alternative to other smoothing techniques such as a moving average. The algorithm performs a local polynomial regression, typically least squares, on the distribution to determine a smoothed value for each point. The SG method chooses coefficients that preserve the higher moments in the data. In this manner, SG smoothing is superior to other moving average methods because it preserves special features of the original distribution such as peak height and width that are generally lost.

For this study, the SG method is performed by Tablecurve 2D across the entire distribution with a moving window that is specified according to the detector resolution.

The width, in number of channels, of the moving window is found by dividing the detector resolution (keV) by the number of keV channel^{-1} in the spectrum.

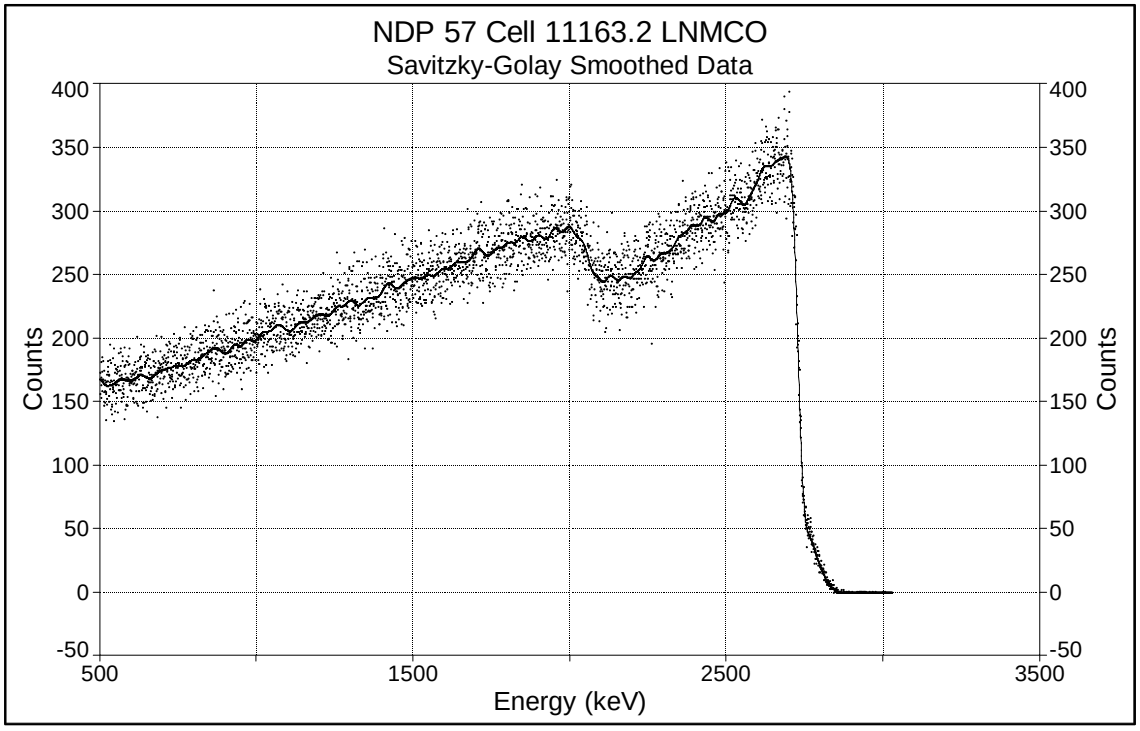

Figure 4.5: The smoothed line that cuts through the data (dots) is the SG smoothed data. The specified width of the moving window helps to preserve special features such as the peak near the leading edge.

An example of SG smoothed data is shown in figure 4.5. To verify the validity of this smoothing method a short study was performed early in this research. By comparing smoothed data against a raw spectrum from a very long count (45 hours) and a normal count (8 hours), the percent difference between each data set was computed. This method assumes the data set from the very long count to be the ideal set since the statistics are very good.

Figure 4.6 shows that both the moving average smoothing method and the SG method maintain a percent difference from the ideal data of 5% or less. In contrast, the

unsmoothed data from a normal 8-hour count has much larger percent differences from the ideal set, up to as high as 19%.

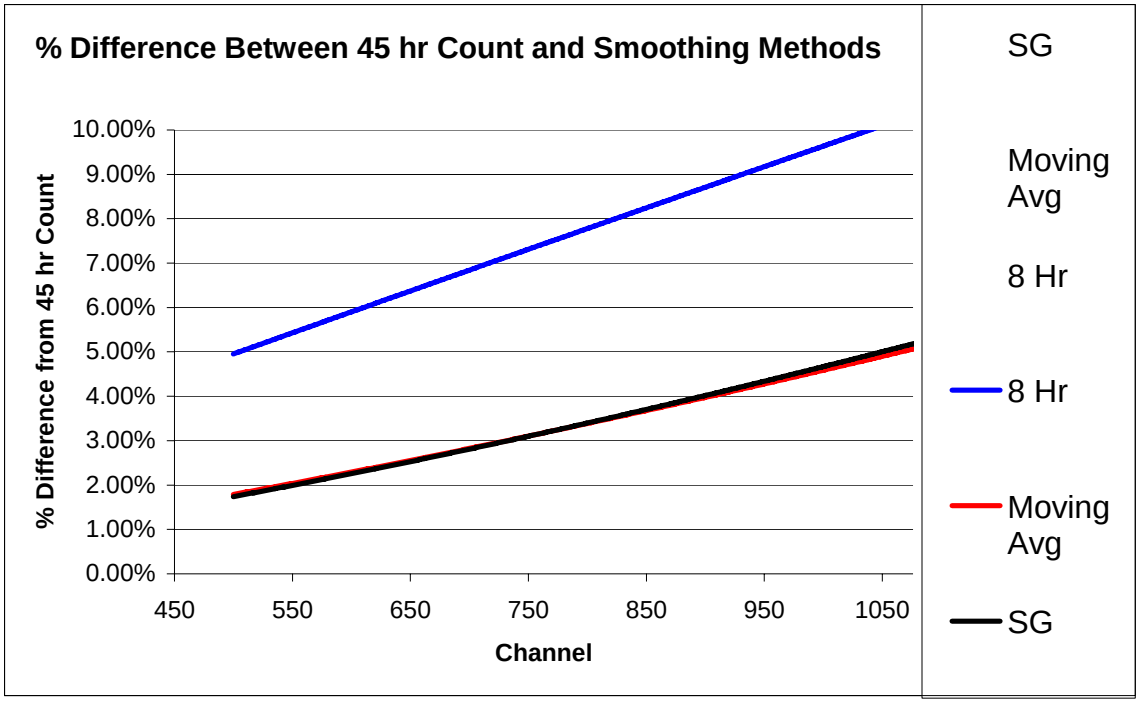

Figure 4.6: Trends of data sets' percent differences from the ideal data set. The moving average smoothed data and SG data are not distinguishable, but both have lower percent differences than the 8 hr data.

The trends of figure 4.6 validate the SG method of smoothing in the following ways:

- SG smoothing provides significantly more accurate data than the raw data from a normal 8 hr count when compared to an ideal data set. Deviation from the ideal set was 4.1% higher on average for the 8 hr count than for the SG smoothed data.
- SG smoothing is as accurate as typical moving average smoothing methods, but has the added advantage of maintaining special features of the data.

Concentration and Depth Profiling

The charged particle energy spectra such as that seen in figure 4.5 are analyzed to determine the depths from which charged particles in each energy channel have been emitted. The low energy, 0.025 eV, of the incident neutron and the small mass ratio of the charged particles to the original nuclei allow for the assumption that the reaction occurs at the same location that the charged particle is emitted [22]. The neutron absorption reaction being used for profiling of the lithium ion battery electrodes is,

$$^{6}Li + n \rightarrow {}^{3}H\ (2727.88\ keV) + {}^{4}He\ (2055.12\ keV).$$

Accurate determination of a depth profile from the charged particle energy spectrum is dependent upon the following:

- An accurate energy spectrum with no shifts during counting.
- Accurate energy calibrations for each particle of interest.
- Knowledge of sample composition and density for the determination of an accurate stopping power function, *S(E)*.
- Knowledge of detector resolution for data smoothing.
- Homogeneous sample with no unknown large spatial density fluctuations or hidden layers.

The SRIM 2006 code developed by Ziegler *et al* has been previously discussed in the theory section of this report. SRIM was used to determine stopping power functions, *S(E)*, for each of the cathode and anode compositions analyzed in this research. Atomic compositions of each sample type were well known since each sample was either made by the author, or was described in detail by the manufacturer. Following the assumption of the Goodenough Research group, each sample was assumed to have a homogeneous

density distribution. Ensuring homogeneity throughout the electrode is of great importance to the cell's performance for both lab and commercially made samples.

Stopping power functions were found for the following sample types:

Table 4.3: Primary chemical components of electrode samples from both lab and commercially mad cells.

Commercial Sample	**Lab Made Sample**
$Li_{1-x}FePO_4$	$Li_{1-x}CoO_2$
$Li_{1-x}FePSO_4$	$Li_{1-x}FePO_4$
$Li_{1-x}CoO_2$	$Li_{1-x}Ni_{1/3}Mn_{1/3}Co_{1/3}O_2$
Li_xC_6	

Chemical components to the sample other than oxide materials were also included in the calculation of the stopping power for each sample. The specific components for each sample are described in the experimental section involving those samples. The variable amount of lithium in each sample described by the 1-x subscript is a result of the ion mobility throughout the cell. The range of value for x was between 0 and 0.65, however much more precise estimates can be made with knowledge of the state of charge of the cell. However, the stopping power of each sample changes by an insignificant amount with the value of x due to the small relative electron density offered by lithium when compared to the other chemical components.

Sample and charged particle descriptions are input into the SRIM code for it to calculate a data array describing the stopping power, *S(E)*, of each sample for each charged particle. The array is fit to a function with Tablecurve 2D that accurately describes, *S(E)*, over the significant energy range of the charged particle. An example of a stopping power, *S(E)*, plot and fitted function are shown in figure 4.7.

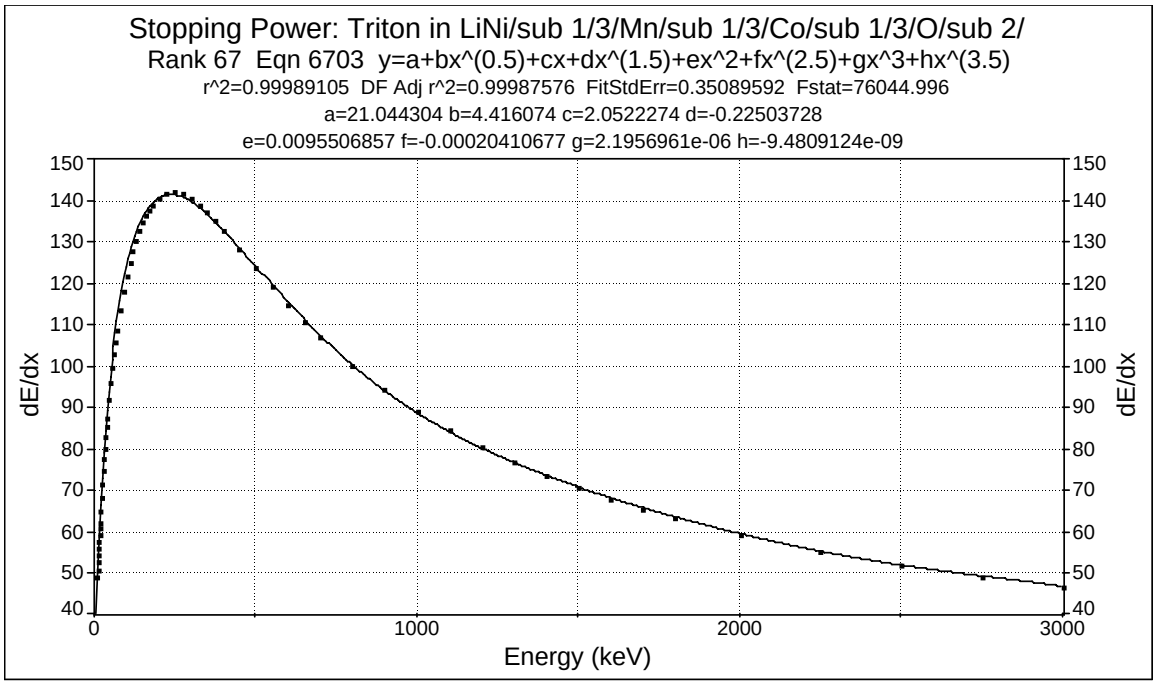

Figure 4.7: The data array describing the stopping power of a sample is fit to a function that can be integrated for the determination of a depth profile. The function in this figure describes the stopping power of a triton particle in a $Li_{1-x}Ni_{1/3}Mn_{1/3}Co_{1/3}O_2$ cathode.

Determining the depth profile is straightforward after the stopping power function and energy spectrum have been found. Equation 4.2 describes the relationship between the energy channels of the spectrum and the stopping power function, *S(E)*.

$$x = \int_{E(x)}^{E_0} \frac{dE}{S(E)} \tag{4.2}$$

Integration of each energy channel from the energy of that channel, *E(x)*, to the original energy of the particle, E_0, determines the path length, *x*, from which particles counted in that channel originated. Since there was no angle between the detector and the

sample in this experimentation, the path length, *x*, is also the depth in the sample that the particle was originally emitted.

Profiling the concentration of a sample is performed by comparison with the standard concentration used for calibration that was described earlier. Calibration produces a value of counts related to the total specified concentration of atoms per square centimeter profiled in the standard. The total concentration is divided by the number of counts to produce a value in units of atoms cm^{-2} $counts^{-1}$ for that neutron fluence and geometry.

The determined value of atoms $count^{-1}$ is multiplied by the number of counts in each channel to determine an area concentration in atoms cm^{-2} represented by that channel. Any difference in neutron fluence or cross-section of the particle being counted must be accounted for via a ratio to those with which the standard was recorded. This is shown in equation 4.3 for the concentration determination of a channel *i*.

$$(C_{sample})_i = \left(\frac{atoms}{count}\right)_{std} (Counts_{sample})_i \left(\frac{\Phi_{std.}}{\Phi_{sample}}\right)\left(\frac{\Omega_{std.}}{\Omega_{sample}}\right)\left(\frac{\sigma_{std.}}{\sigma_{sample}}\right) \tag{4.3}$$

The efficiency for detection will cancel if the system is calibrated with the same geometrical and electrical setup as is used for sample analysis. However, one final adjustment to the concentrations for each channel is required. The depth interval represented by higher energy channels is larger than those of lower energy channels since particles with more kinetic energy will travel a farther distance within the energy width of a channel. Therefore the depth increments represented by the higher energy channels are larger than those of the lower energy channels. This is the reason that a uniform sample will produce energy spectra with the counts vs. channel having a positive slope rather than no slope at all. As a result, the number of counts related to the channels across the energy spectrum cannot be given equal weight.

The concentration corresponding to each channel is adjusted by the ratio of the largest depth increment, correlating to the highest energy channel, to the depth increment represented by the channel being analyzed. The concentration in the channel, C_i, is given by equation 4.4.

$$(C_i)_{adjusted} = C_i\left(\frac{\lambda_{\max}}{\lambda_i}\right) \tag{4.4}$$

Equation 4.4 includes the value of the depth increment, λ, represented by a channel.

Error Analysis

Uncertainty in Depth

The energy distribution of the incident charge particles to the detector is measured so that a depth distribution may be gained from this information. The incident energy distribution is perturbed by the energy broadening of the monoenergetically emitted particles. Three main contributions result in the energy broadening seen in detection; 1.) the system resolution, 2.) energy straggling, and 3.) geometric acceptance angles [43].

System Resolution- The system resolution can be determined by differentiation of the energy spectrum step from surface particles recorded from a thick sample. This process has been described in the energy calibration section. The total system energy resolution of the UT-NDP system for the detectors used is described in table 4.4. The Tennelec TP-150-75-30-NH-S surface barrier detector that was used at NIST has a detector resolution of 35.84 keV off of the $LiNbO_3$ surface.

Table 4.4. Total energy resolution of the UT-NDP system with corresponding detectors.

Detector	TB-015-50-150	TU-013-100-100
Energy Resolution (keV)	29.74	26.89

Values from table 4.4 indicate that the UT-NDP system is approximately doubling the independently verified 5.486 MeV alpha energy resolution of each detector. Reasons for this additional noise can include [44]: statistical fluctuation in ionization processes associated with specific particles, choice of pulse shaping time constants, imperfect capacitance matches between detector and preamplifier, extraneous RF and gamma noise picked up by the detector, vibrations from vacuum equipment surrounding detector, imperfect filtration and amplification of low-level noise by pre-amp and amplifier, voltage variation in bias supply and supply to system electronics. The system resolution is a function of the detector noise, σ_D, and the electronic noise, σ_E, which is predominantly a result of the pre-amplifier. The resolution is found by equation 4.5.

$$\sigma_{Sys} = \sqrt{\sigma_D^2 + \sigma_E^2} \tag{4.5}$$

Energy straggling- Energy straggling is an effect of small-angle scattering of the charged particle within the matrix material. The theory of energy straggling is most often associated with Bohr [45] who described the interactions of a particle with no electrons moving through a material. However it would be erroneous to describe the movement of recoil nuclei and the majority of charged particles observed in NDP by this model [46]. The velocities required to suit the Bohr model are much higher than those of most particles observed with NDP. To account for energy straggling, it is more accurate to estimate the effect with SRIM simulations.

Geometric Broadening- Particles emitted from the same depth in a material will still have a range of path lengths that they will subtend on their trajectory from reaction origin to the detector. This is because the detector subtends a finite solid angle. The difference in path lengths contributes to the overall energy broadening of the system [47]. The effect of geometric energy broadening is enhanced to a much greater degree at larger depths.

The total energy broadening for detection is derived from the summation of the 3 broadening contributions in quadrature as shown in equation 4.6.

$$\Delta E = \sqrt{\partial E_{Sys}^2 + \partial E_{stragg}^2 + \partial E_{geom}^2} \tag{4.6}$$

The energy resolution, ΔE, however, is often taken to be only derived from the energy broadening of the system as determined from the differentiation of a thick sample energy spectrum step. This approximation is not unreasonable at shallow depths. For a dense sample such as borosilicate glass the energy broadening becomes quite large within the first 2.5 μm as shown in figure 4.8. However, the lower density of this study's samples as well as the lower charge of the triton particle allow for depths of approximately 11 μm to be profiled before the total energy broadening (excluding broadening from electronics, σ_E) becomes greater than 15 keV. The figures below compare the energy broadening mechanisms for the alpha in borosilicate glass and the triton in an electrode material.

The energy resolution, ΔE, will vary with depth in the material. Since the depth resolution of profiling is dependent upon ΔE, then the depth resolution also varies with depth according to the equation 4.7.

$$\Delta d = \frac{\Delta E}{\bar{S}} \tag{4.7}$$

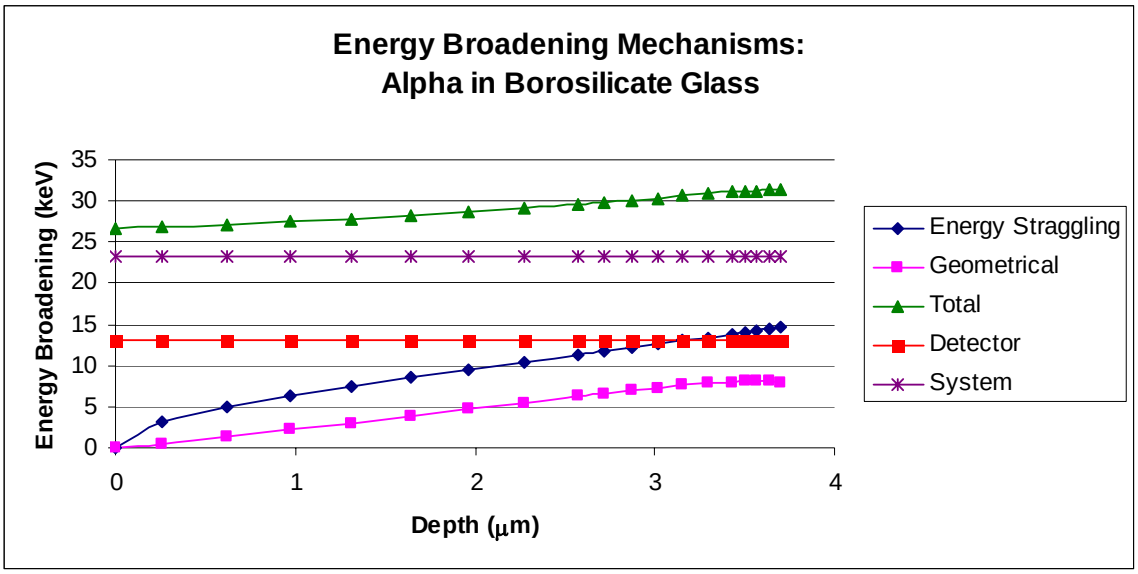

Figure 4.8: Energy broadening mechanisms for an alpha particle in borosilicate glass limit the reasonable depth for profiling to ~3 μm.

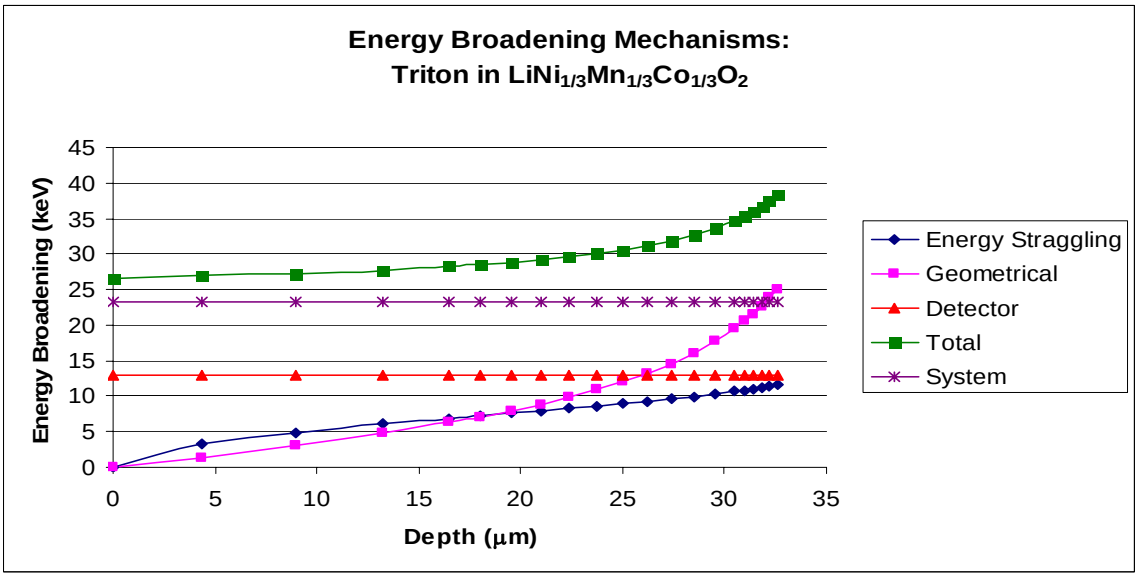

Figure 4.9: The lower density of the electrode materials and lower charge of the triton result in the energy broadening mechanisms being less substantial at larger depths than that for the alpha in a denser sample.

$\bar{S}$ in the depth resolution equation is the average stopping power value, and ΔE is the energy resolution for the relevant depth for which the depth resolution is being derived.

The lower density of the samples in this study corresponds to lower electron densities and therefore a lower average value for the stopping power. The charge of only +1 on the triton also contributes to the lower stopping power in comparison to an alpha particle. The lower stopping power, as seen from equation 4.7, means that the depth resolution for electrode samples will not be excellent. Depth resolution for the triton near the surface in a $Li_{1-x}Ni_{1/3}Mn_{1/3}Co_{1/3}O_2$ cathode sample is 0.463 μm. The depth resolution for an alpha particle near the surface of the same cathode sample is 81.5 nm.

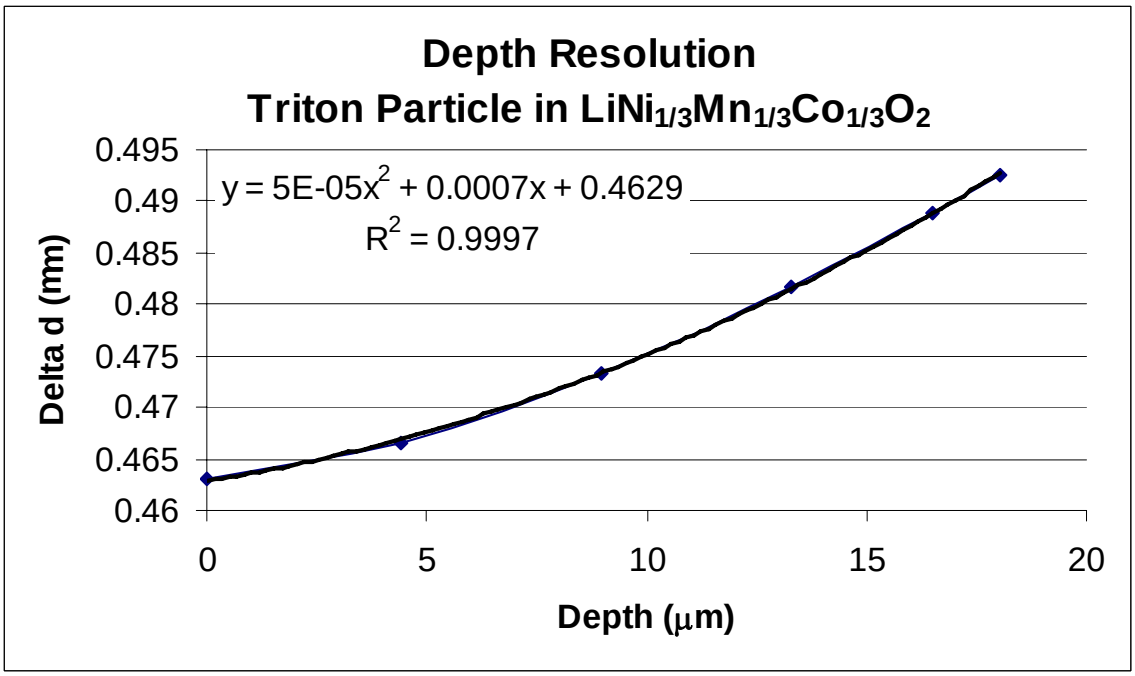

Figure 4.10: An example of how the depth resolution varies throughout a sample.

Figure 4.10 shows an example of how the depth resolution can change depending on the depth of the particle. The increase in Δd is a result of the increasing energy broadening associated with depth. In order to calculate how the depth resolution varies

within the sample, one must fit a function to the ratio of the total energy broadening as a function of depth to the average stopping power.

With the latter resolutions, it is easy to understand why analysis that requires higher depth resolution, such as investigating the SEI layer in anodes, will use the energy spectrum of the alpha particle although the alpha can only profile as deep as ~4 μm. The majority of this research, however, takes advantage of the 11 μm depths that can be analyzed with the triton. The objective of analyzing samples such as the cathodes was to determine a depth distribution of the lithium to understand if it was collecting near the surface, and this objective was not hampered by the poor resolution of the triton.

At this point in the report, it should be noted that the former discussion of depth resolution will be important for the reader to remember when considering the depth profiles of samples. Typical depth profiles have concentration values that extend seemingly beyond the surface into "negative depth". This is a consequence of the energy broadening of the system. The counts extending into negative depth are counts that belong to the surface, but have been shifted to higher energies by the detection system.

Uncertainty in Concentration

Uncertainty in the concentration measurements of this study has two sources: the uncertainty in the concentration standards used for calibration, and the statistical uncertainty associated with the counts per channel of an energy spectrum. The latter uncertainty was empirically determined for this study by repetitive analysis of the same sample.

A lab made $LiFePO_4$ cathode that was cycled 100 times was profiled three times for the same neutron fluence to achieve similar counting statistics. The depth profiles of the spectra were compared to determine the variation between the concentration measurements. The spectra recorded were profiled to achieve the same counting statistics as the other profiled samples in this research so that the determined variation in

concentration can be used as one aspect of the error for concentration. The spectra along with associated error bars can be seen in figure 4.11.

The average number of counts per channel in the data sets is 44.95. This represents a count time of 6 hours. Both values of count time and counts per channel are typical results for this research. The percent difference between the data sets varies by channel but does not vary in correlation to depth. The average percent deviation over the spectra is 2.24%. In terms of counts and concentration, this correlates to 1.01 counts per channel, and approximately 4.31 x 10^{11} atoms cm^{-2}.

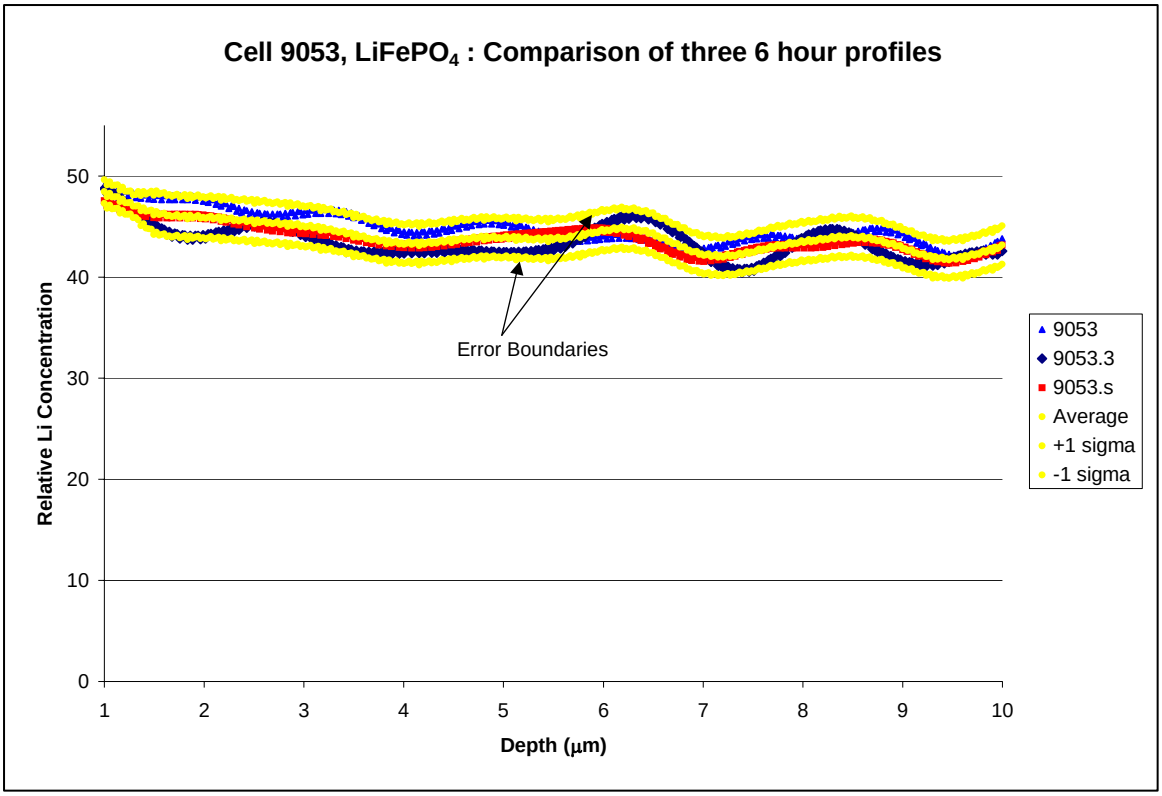

Figure 4.11: An LFP cathode was profiled three times to determine a value for concentration error as well as to distinguish between statistical and real features of the profile.

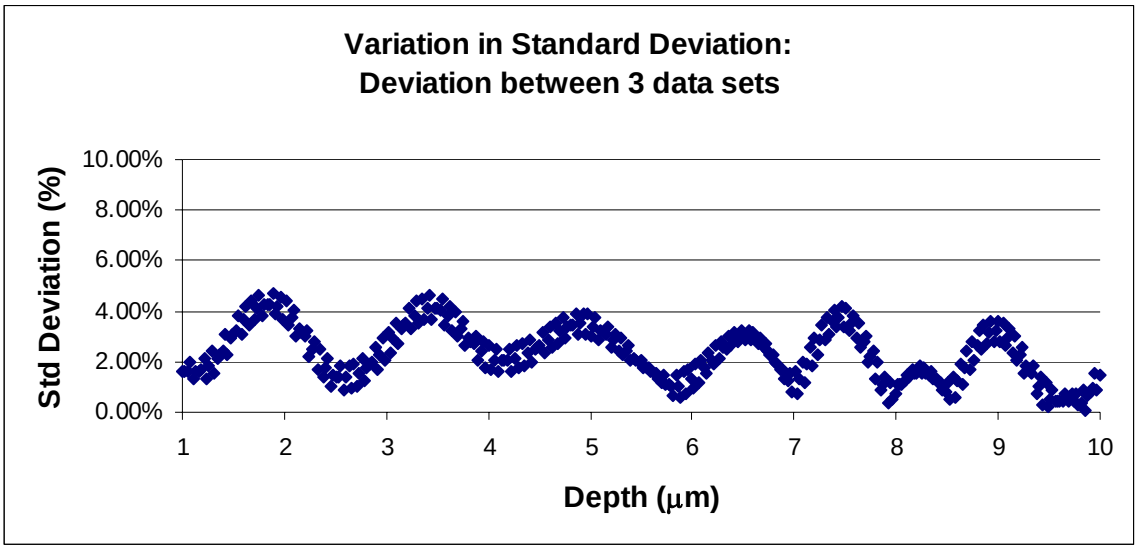

Figure 4.12: Variation of percent difference between the two data profiled for error determination.

The correlation slope between the data sets is 0.9985. To ensure that the data sets and the associated uncertainty are within control, a β statistic test was performed [48]. For the test, a 95% confidence level (α=0.05) was used. Results from the test show the value of p=0.1464 is higher than α=0.05.

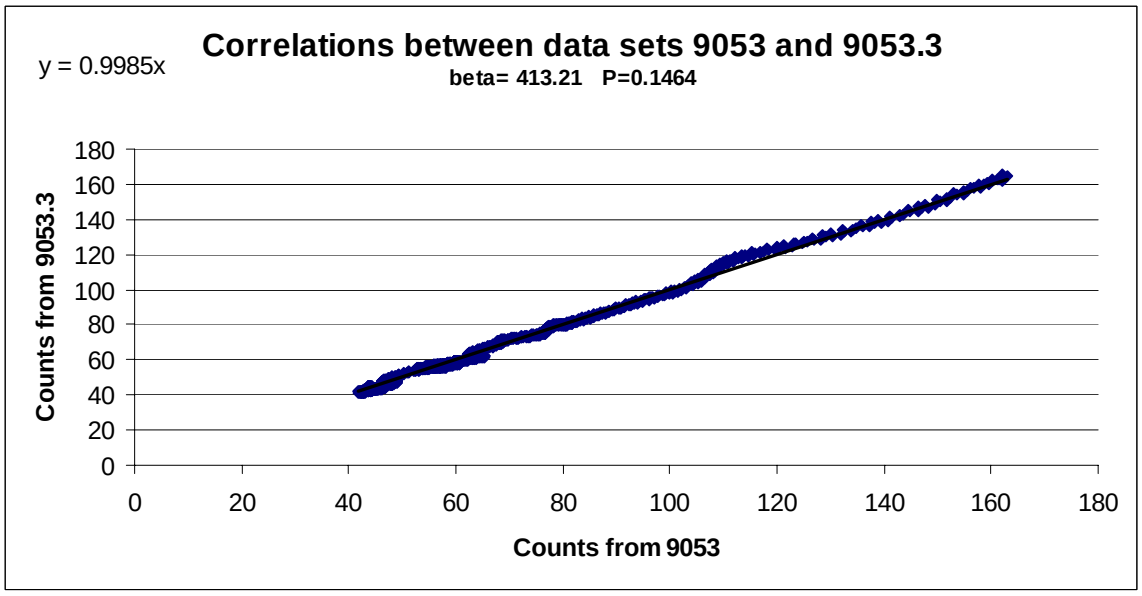

Figure 4.13: A β statistic test was performed to show that the data sets and their associated error were in control.

The value of p being higher than α indicates that the data sets along with the empirically derived error are in statistical control. This validates the error derived from this method.

For depth profiles with specific concentrations assigned to each channel rather than only relative lithium concentration, a total error in concentration must be found. This error includes the empirically derived error associated with charged particle counting as well as the error associated with the standard material used for concentration calibration. The uncertainty in the concentration of the standard material used for concentration calibration is 0.57%. The error associated with the standard value, *S*, of atoms count^{-1} cm^{-2} that is found by counting the concentration standard is,

$$\sigma_S^2 = \frac{\alpha^2}{c^2}(\sigma_c^2) + \frac{1}{c^2}(\sigma_\alpha^2) \tag{4.8}$$

For equation 4.8, α represents the concentration value of the standard, and *c* is the value of the counts in the spectrum. Ignoring any adjustments for neutron fluence and depth intervals, the concentration value, *C*, assigned to a channel is found by equation 4.9.

$$C = (S)(c) \tag{4.9}$$

Therefore the percent error in concentration is given by equation 4.10.

$$\frac{\sigma_C}{C} = \sqrt{\frac{\sigma_c^2}{c^2} + \frac{\sigma_\alpha^2}{S^2}} \tag{4.10}$$

The error associated with concentration measurements arising from particle counting has been empirically determined to be 2.24%. The percent uncertainty in *S* is then 2.31% from equation 4.8. Finally, the total percent uncertainty associated with a concentration value is the result of taking the percent errors associated with *S* and with the counting statistics in quadrature as in equation 4.10. The total percent uncertainty for concentration measurements in this report is 3.22%.

Chapter 5: Benchmarking and Feasibility of Electrode Neutron Depth Profiling

Aside from analytical investigations of lithium ion cells under varying conditions, this research also had the objective to thoroughly validate the use of NDP towards lithium ion cell electrode research. This includes benchmarking results of NDP electrode profiles as well as analyzing any specific applications of lithium ion research that NDP may not be suitable for.

Since its reestablishment in 2005, the UT-NDP facility has not been benchmarked to another facility for depth and concentration. This chapter includes validation for the results produced at the UT-NDP facility by comparison to the following: profiles of the same samples measured at the NDP facility of the National Institute of Standards and Technology (NIST), profile determined by Secondary Ion Mass Spectrometry (SIMS), and to profiles produced by MCNPX modeling.

UT-NDP PROFILES AND NIST PROFILES

Two samples were profiled with NDP at the NIST-NDP facility and the UT-NDP facility. The two samples profiled were a graphite anode from a commercially made $LiFePSO_4$ (LFPS) cell and a lab made $LiNi_{1/3}Mn_{1/3}Co_{1/3}O_2$ cathode. Since NDP is a non-destructive technique, the samples analyzed on both systems were the exact same sample, not just similar types. The objective of repeating this analysis on both systems was both to benchmark the UT-NDP facility and also to investigate the precision of analyzing electrode samples with NDP.

The LFPS graphite anode was profiled at NIST with a Tennelec surface barrier detector. The detector has a 75 μm active depth and a 150 mm^2 active area for detection.

The detector was operated at a 30 V positive bias during the charged particle measurement. The graphite sample was covered with a Teflon mask with a 10 mm diameter aperture to select the area to be profiled. The sample was then set 9.5 cm from the detector face. The geometry of the set-up had the sample facing directly to the detector (*i.e.* the detector was not at an angle to the sample normal). This same set-up was used for the UT-NDP measurements except that the detector was the TU-013-100-100 detector previously described and the distance between sample and detector was 7 cm.

The profiles of the graphite anode from each system are shown in figure 5.1.

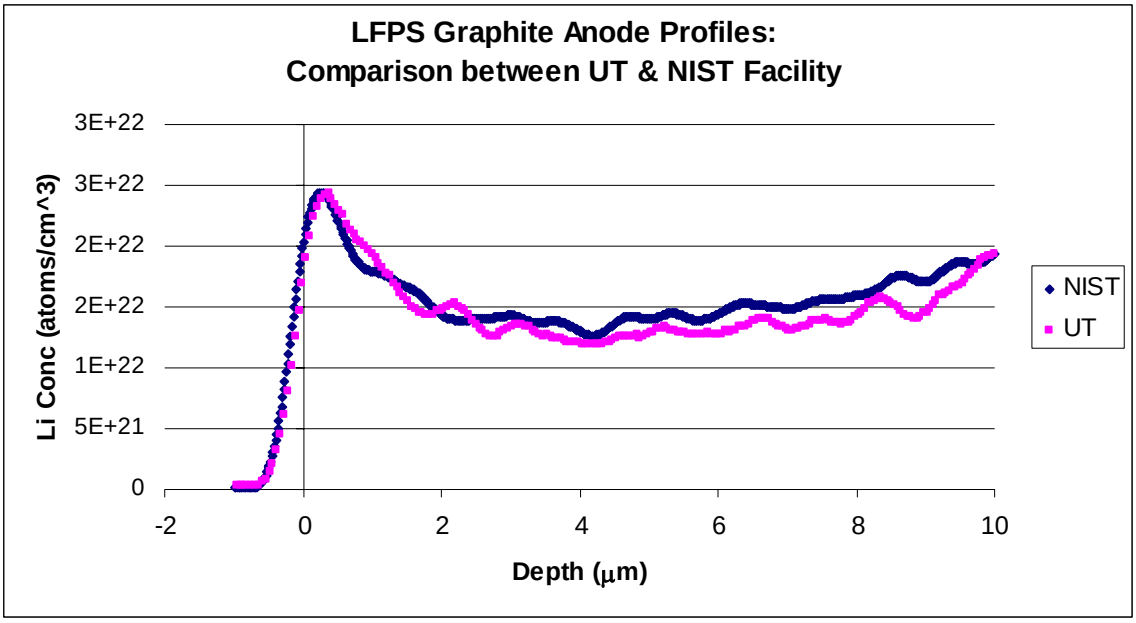

Figure 5.1: Graphite anode profile by UT and NIST NDP facilities.

The profiles are both profiles formed from the triton energy spectra. That is why the deeper 10 μm depth distribution can be shown here. The profiles are very similar in the first 3 μm but begin to diverge slightly after this point. However, the profiles both show similar shape in the distribution over the entire 10 μm of profiled depth. This is the first very important factor.

Secondly, the integrated concentrations of the profiles match reasonably well.

Table 5.1: This table shows the percent difference in total concentration (atoms cm^{-2}) measured by the UT-NDP and NIST-NDP systems. The values shown are those for the total concentrations over the specified depth of 10, 3, or 2 μm.

	10 μm (atoms cm^{-2})	% Diff	3 μm (atoms cm^{-2})	% Diff	2 μm (atoms cm^{-2})	% Diff
UT	1.53E+19	6.82%	5.56E+18	2.37%	4.21E+18	2.00%
NIST	1.64E+19		5.69E+18		4.29E+18	

Table 5.1 shows the values of percent difference between the UT and NIST profiles dependent upon how deep the total concentration is collected over. It is apparent that if one integrates the concentration over the entire 10 μm depth of the profile, then the percent difference is increased. The decreasing trend of the percent difference, shown in figure 5.2 is not unexpected.

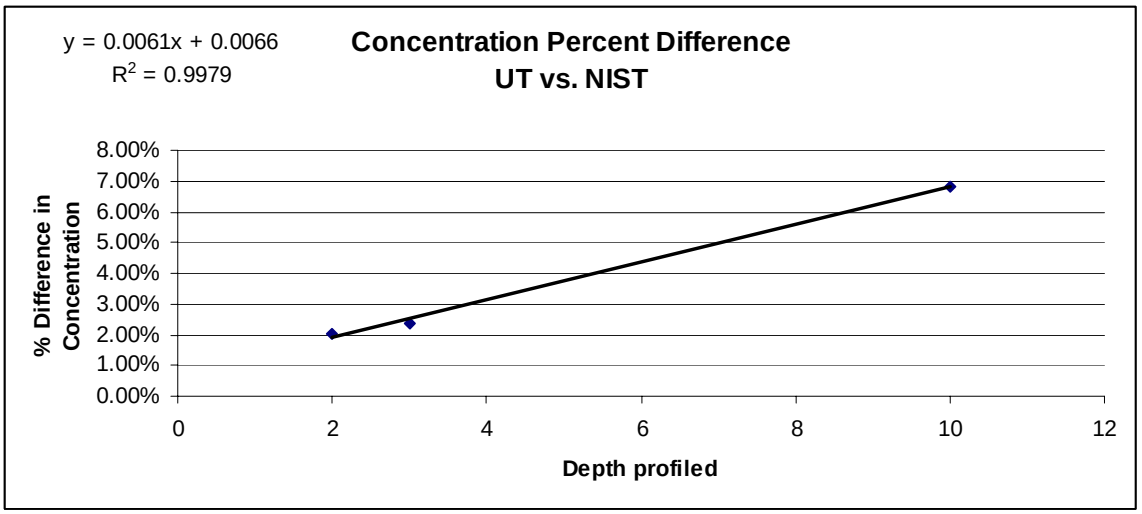

Figure 5.2: The percent difference in the total concentrations measured by the UT and NIST facilities increases with the total depth over which it is integrated.

Most likely, the reason for the increasing difference in concentration between the profiles is due to counting statistics. The percent difference between the profiles increases because the deeper channels have less counts than those representing the higher concentrations within the first 3 μm. Therefore the trend is a result of the decreased

counts at this depth, not of the systems' abilities. It is reasonable to assume that if each count were performed once again for a longer period, then the values of table 5.1 would be decreased.

However, the percent difference between the UT and NDP concentrations are easily within uncertainty for the 2 and 3 μm integrated concentration values. According to the slope of the trendline in figure 5.2, the percent difference between the two profiles will exceed the allowed uncertainty in concentration measurements at 4.34 μm.

Finally, the third successful feature of the profile comparison is the depth measurements. A zoomed in chart of the inflection points of the profiles from figure 5.1 is shown in figure 5.3.

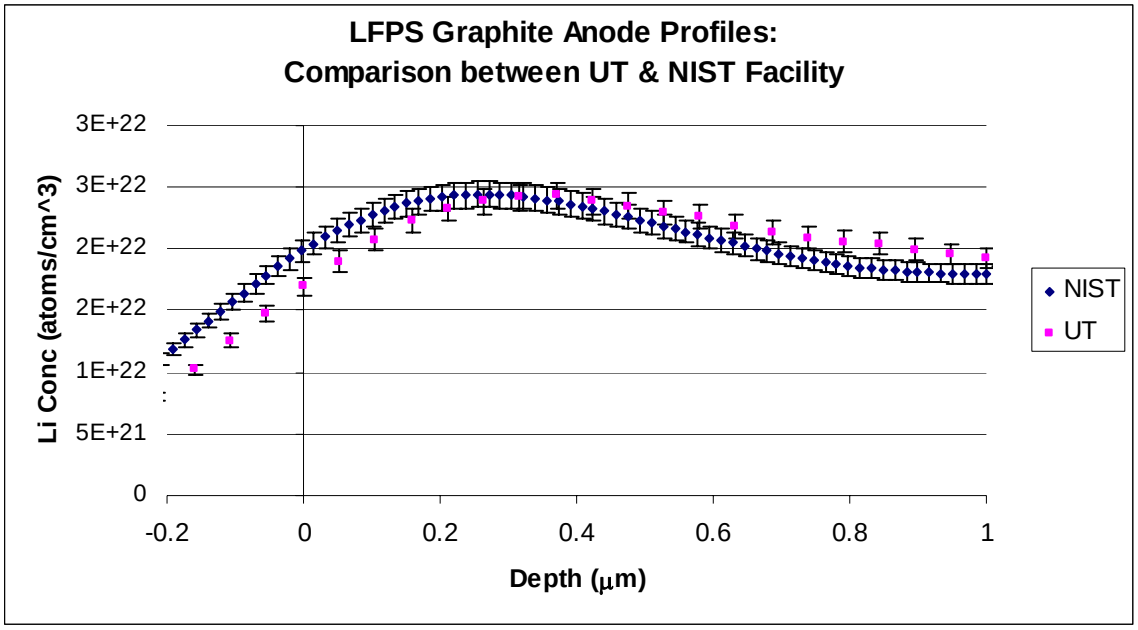

Figure 5.3: The inflection points of the UT and NIST profiles are well within the 0.444 μm depth resolution for the triton particle.

Figure 5.3 shows that the depths of each profile's inflection point are well within the 0.444 μm depth resolution of the triton particle in graphite. Depths of the inflection point determined for each profile are within 82 nm of one another. The difference

between the concentration measurements at these inflection points is 0.23% as listed in table 5.2.

Table 5.2: Differences between inflection points of the NDP and NIST profile.

	Depth of Maxima (μm)	Concentration (atoms cm^{-3})	Concentration % diff	Depth Difference (nm)
UT	0.3695	2.43E+22	0.23%	82
NIST	0.2881	2.44E+22		

The $LiNi_{1/3}Mn_{1/3}Co_{1/3}O_2$ cathode was also profiled at NIST with a Tennelec surface barrier detector. The NIST spectrum was counted for 40 minutes and 32 seconds to achieve an average of 358.15 counts per channel. The UT spectrum was counted for 12 hours and 18 minutes to achieve an average of 293.61 counts per channel. UT had an average count rate of 0.007 counts per channel per second while the NIST system had an average count rate of 0.147 counts per channel per second. That is a factor of 21 difference in count rate.

The samples were counted to reach reasonable statistics and determine if the percentage difference values from the previous benchmark sample could be decreased. Figure 5.4 shows the two profiles measured by each system. The profiles are very well matched to one another in terms of shape, concentration, and depth values. The energy broadening of the system also seems very similar indicating similar depth resolution.

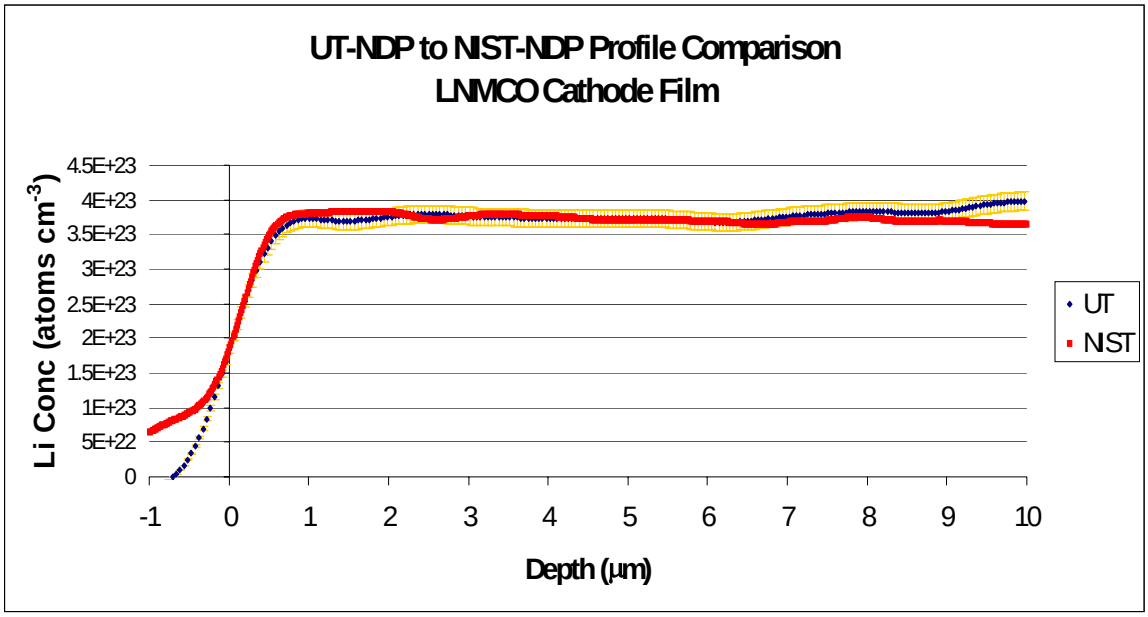

Figure 5.4: Comparison of NIST and UT NDP profiles of the LNMCO cathode.

The percent differences between the integrated concentration values of each profile over 10, 3, and 2 µm are shown in table 5.3. All of the percent differences are well within the allowed concentration error of 3.22%. The values from table 5.3 do not show a trend of increasing deviation as a function of depth as occurred in the anode sample. As a result, we can conclude that the trend seen for the anode sample was due to the decreased number of counts in the deeper regions, not due to any geometrical effects.

Table 5.3: Percent differences in total concentration (atoms cm^{-2}) measured by the UT-NDP and NIST-NDP systems. The values shown are those for the total concentrations over the specified depth of 10, 3, or 2 µm.

	10 micron (atoms/cm^2)	% Diff	3 micron (atoms/cm^2)	% Diff	2 micron (atoms/cm^2)	% Diff
UT	3.73E+20	0.61%	1.09E+20	1.83%	7.20E+19	1.69%
NIST	3.71E+20		1.11E+20		7.33E+19	

The depth values of each profile at the inflection point were 0.668 μm for UT and 0.591 μm for NIST. This is a difference of 77 nm. This value is also within the allowed error for depth.

The deviation in concentration seen in negative depth of the profile comparison is due to summing that occurs in the NIST-NDP system. The UT-NDP system does not see this phenomenon and this is why the concentration values for the UT profile decrease to zero and those for the NIST profile do not. There is no clear explanation for the deviation in values after 9 μm but this is most likely related to the alpha particle interference that begins at approximately 10.5 μm.

Conclusion

Benchmarking the UT-NDP profiling of electrode samples to the NIST-NDP system has been successful in three different, and significant areas: 1.) shape 2.) concentration, and 3.) depth.

First, the shapes of the distributions are the same. Second, the total concentrations determined from the profiles are within expected uncertainty and the difference may be significantly reduced with extended counting times. Differences between total concentrations of the profiles within 2 μm of the surface are less than 2% in the both cases. For the best case, the total concentrations over a 10 μm depth deviated only 0.61% from one another. Finally, the depth measurements of each profile were very similar. The depths of the inflection point of the profiles were separated by only 82 and 77 nm. Both values are well within the depth resolution of the triton particle the graphite and oxide materials. Depth resolution for the triton in graphite is 0.444 μm, and the triton resolution for the triton in the $LiNi_{1/3}Mn_{1/3}Co_{1/3}O_2$ cathode is 0.463 μm. Additionally, the concentration values associated with the inflection point of each profile were within 0.23%.

As a result, it is valid to confirm that the UT-NDP profiles of electrode materials are producing results similar to that of the NIST-NDP facility. This is a proud achievement for the UT-NDP facility since the NIST-NDP facility is a well-accredited profiling system that has been producing world-class profiles for more than 25 years.

UT-NDP Profiles And SIMS Profiles

A similar $LiFePSO_4$ (LFPS) graphite anode to that discussed in the previous section was profiled by the technique of secondary ion mass spectrometry (SIMS). Additionally, a cathode from the same $LiFePSO_4$ cell was also profiled with SIMS. The SIMS technique is a surface analytical technique used for gaining chemical information about the material. The SIMS technique sputters the surface of the sample with O^- or Cs^+ ions. These ions are accelerated towards the surface with potentials typically of a few keV. When the ions hit the surface they can produce secondary analyte ions that are then introduced into a mass spectrometry system. A depiction of the process is shown in figure 5.5.

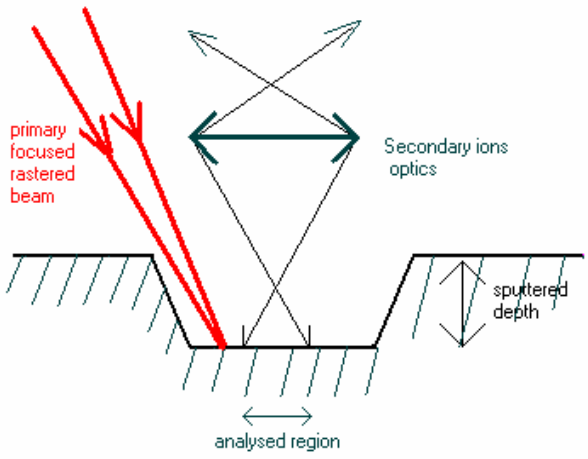

Figure 5.5: Illustration of the sputtering process for the SIMS technique [49].

SIMS has low elemental detection limits typically below 1 ppm. Determining the depth resolution of SIMS is a complicated matter due to artifacts that can arise depending on the sample type and uniformity. The depth is determined according to the sputtering rate, however this rate will vary will sample density. If the sample is not uniform then the sputtering rate will also not be uniform and accurate depth profiles become more difficult.

The samples were profiled with an Atomika 4500 Quadrupole SIMS system at Cerium Laboratories courtesy of Tim Hossain Ph.D. and Ted Neil Ph.D. The surfaces were sputtered with 5 keV O^{2+} ions and the mass spectrometry profiled the secondary positive ions of $^{6}Li^{+}$, $^{57}Fe^{+}$, and $^{12}C^{+}$. The raster size of the beam was 250 x 250 μm. The samples were analyzed at a 0 degree tilt.

The SIMS profile of the LFPS graphite anode is shown in figure 5.6. Only the shape of the distribution could be determined because the sputter rate was not known for the sample. Cerium Labs estimated that the crater depth might be greater than 0.5 μm. This would make the approximate sputtering rate to be 8.3 nm min^{-1}. However, Cerium Labs also stated that the sputtering rate for silicon is between 10 to 20 nm min^{-1}. Since graphite is less dense than silicon, it is reasonable to think that the sputtering rate would be higher than that for silicon. Therefore, the estimate of 8.3 nm min^{-1} may be greatly underestimated.

Since a lengthy discussion on the details of depth cannot accurately be presented due to the absence of a sputtering rate, then the comparison must be primarily based on distribution shape. The SIMS profile of the graphite sample in figure 5.6 has many similarities to the UT-NDP profile of the same sample in figure 5.7. The UT-NDP profile is displayed in log scale since this is the only way that the SIMS data was given. The most significant similarity is the concentration gradient near the surface. The gradient in the SIMS profile appears exponential in the log scale. Similarly the UT-NDP profile shows a dramatically increasing concentration near the surface as well.

The major difference between the two profiles is that the NDP profile appears to have a peak nearly 0.3 μm in from the surface. As previously mentioned, this is an artifact of the energy broadening of the system. The peak appears because counts that belong to the channels representing the first tens of nanometers of the sample depth are losing counts to channels that appear to be above the surface, in "negative depth". This is purely because counts that belong to channel *j* get spread to channel *i* since the system is not perfect. This effect can be accounted for by deconvolution methods, but this is generally not done due to complexity and the majority of analysis does not require it.

However, for the purposes of this comparison the counts that belong to the surface have been summed and then distributed to channels within the surface according to a Guassian distribution. The number of channels over which to distribute the counts is determined by the energy broadening of the system and the number of keV per channel. The validity of this method has been confirmed by using it to determine profiles of samples with a known distribution. An example of such a sample is the uniformly distributed concentration sample, SRM 93a. By this method, an estimated profile of an NDP profile with no energy broadening at the surface is shown in figure 5.8. However it should be restated that this is only an approximation.

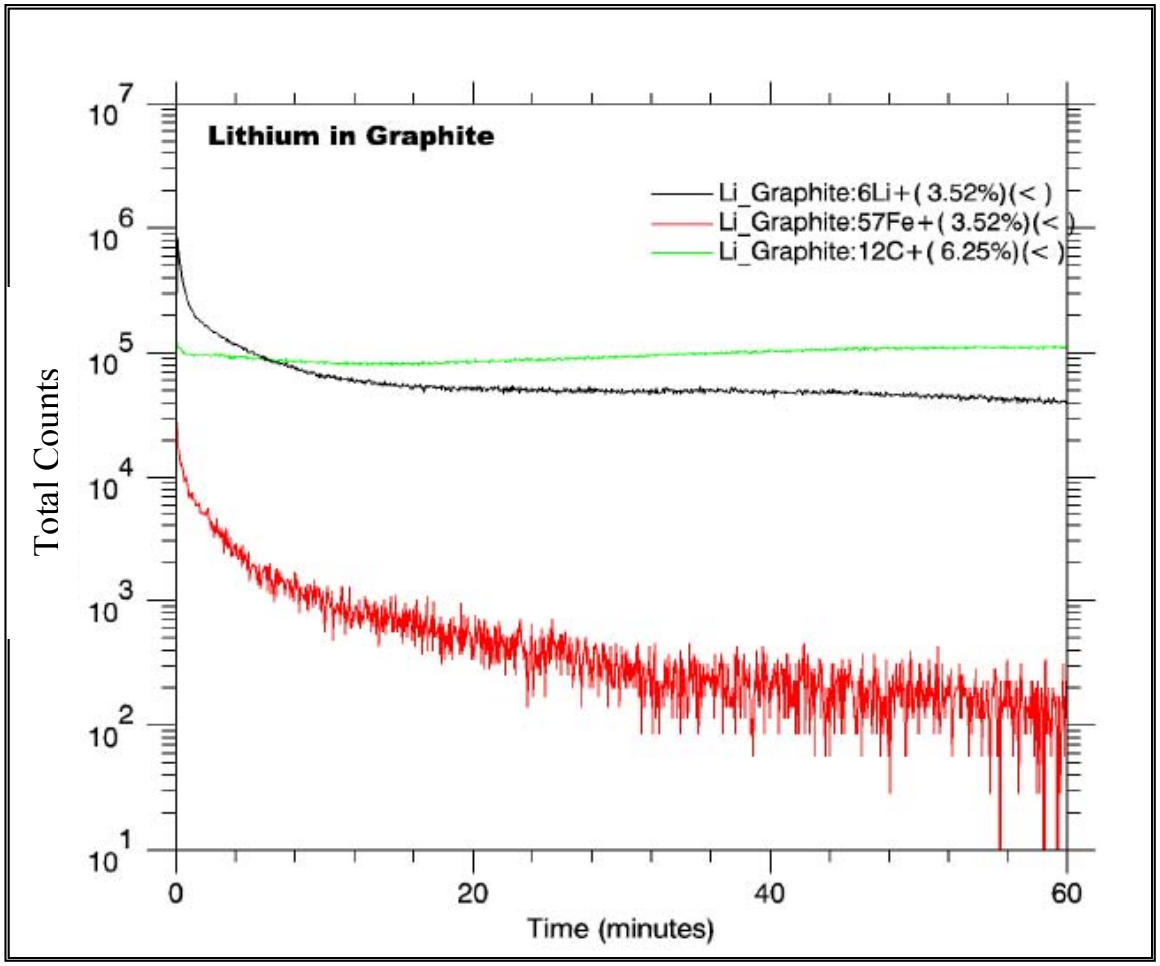

Figure 5.6: SIMS profile of an LFPS graphite anode. The estimated crater depth was greater than 0.5 μm.

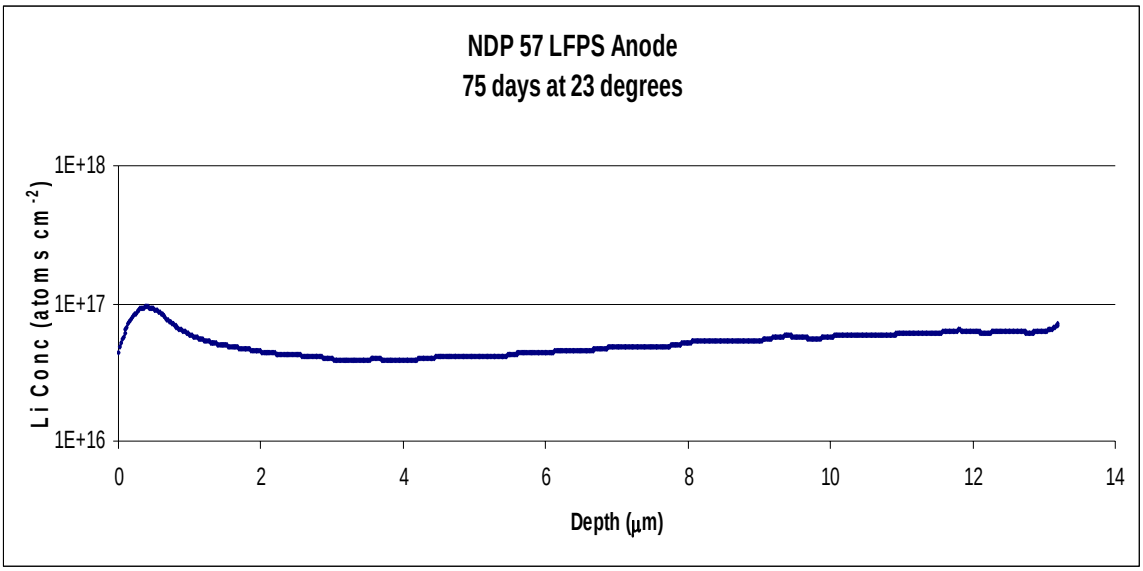

Figure 5.7: UT-NDP profile of an LFPS graphite anode. The profile is presented in log scale for easier visual comparison to the SIMS profile.

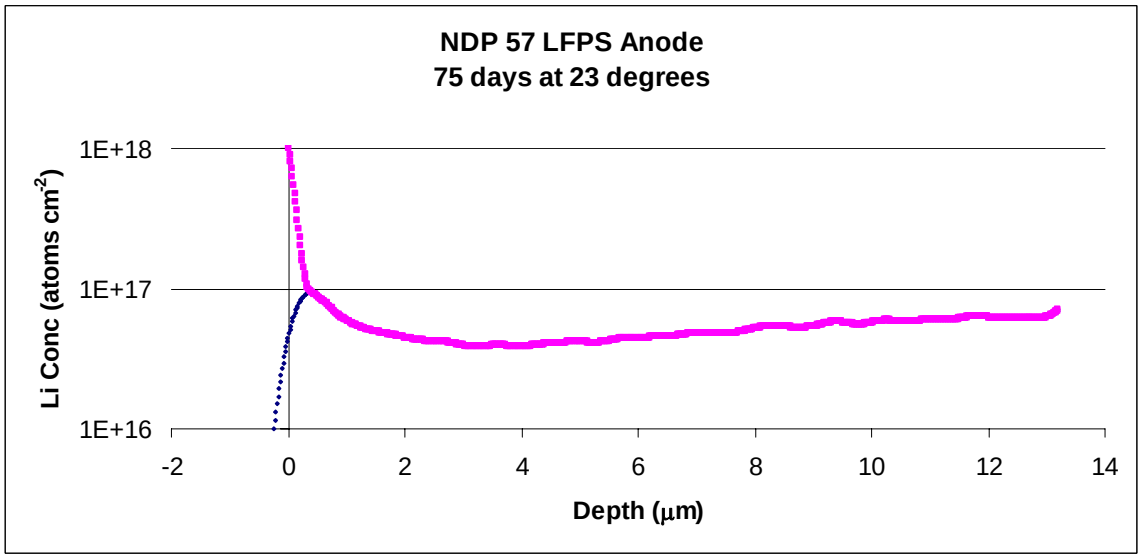

Figure 5.8: Estimate of an NDP profile with no energy broadening near the surface. The pink series represents the profile with no energy broadening. The blue series is the normal profile with energy broadening.

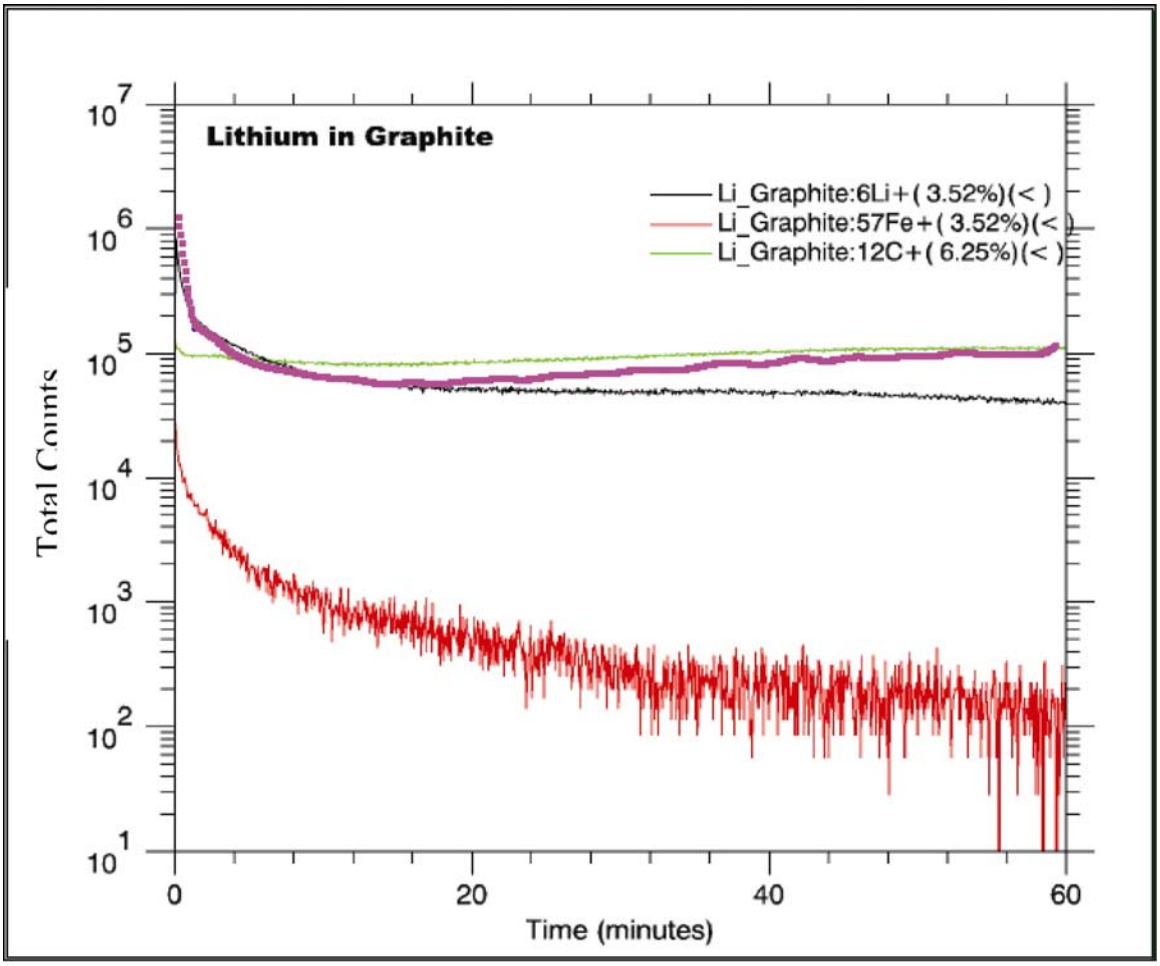

Figure 5.9: The pink distribution is the NDP profile overlapped onto the lithium distribution from the SIMS profile. The depth scales of the two profiles will most likely be different due to their different resolutions, but the exponential distribution is the same for both profiles.

It appears that redistributing the counts from above the surface produces a profile that is very similar in appearance to the SIMS profile. Both profiles have extreme concentration gradients near the surface that indicate a thin film containing lithium. Most likely, this is the presence of the solid electrolyte interface.

The second sample profiled with SIMS was a $LiFePSO_4$ cathode. The profile of the cathode is shown in figure 5.10. Similar to the previous sample a sputtering rate could not be determined.

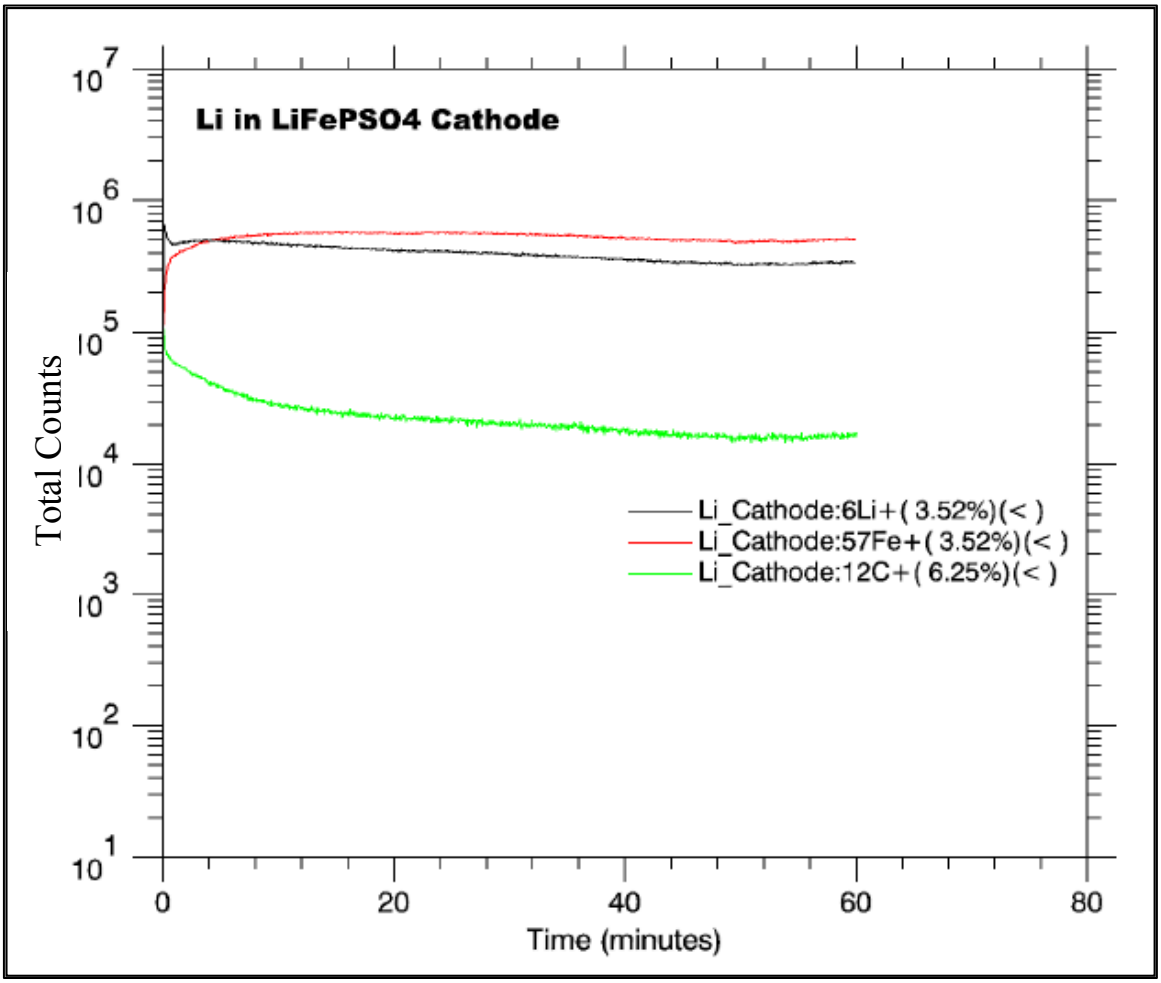

Figure 5.10: SIMS profile of a LFPS cathode.

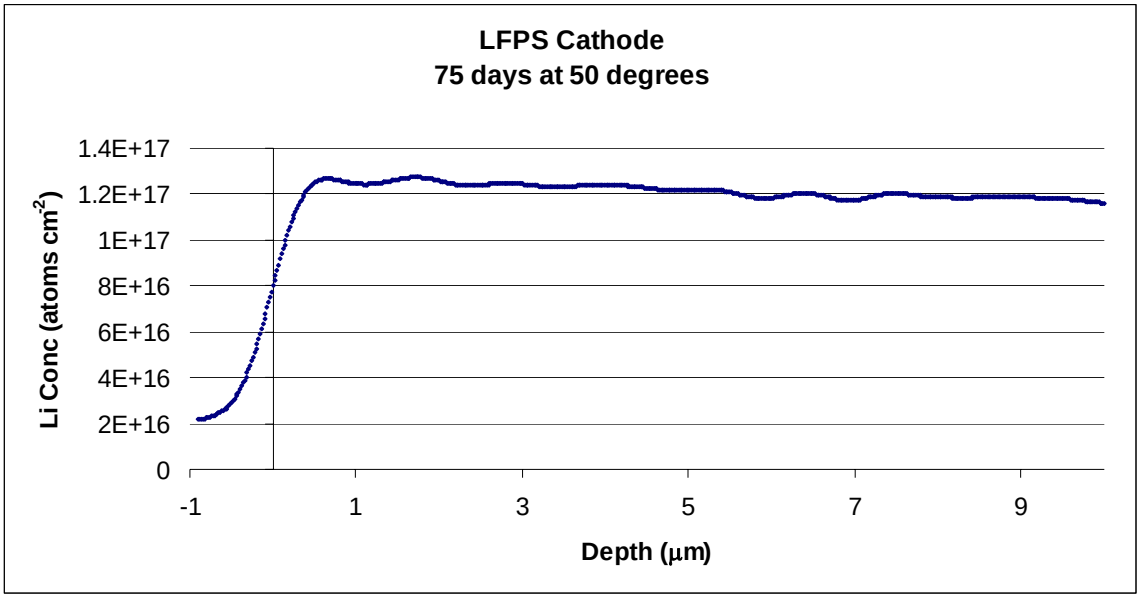

Figure 5.11: UT-NDP profile of the LFPS cathode that was also profiled by SIMS.

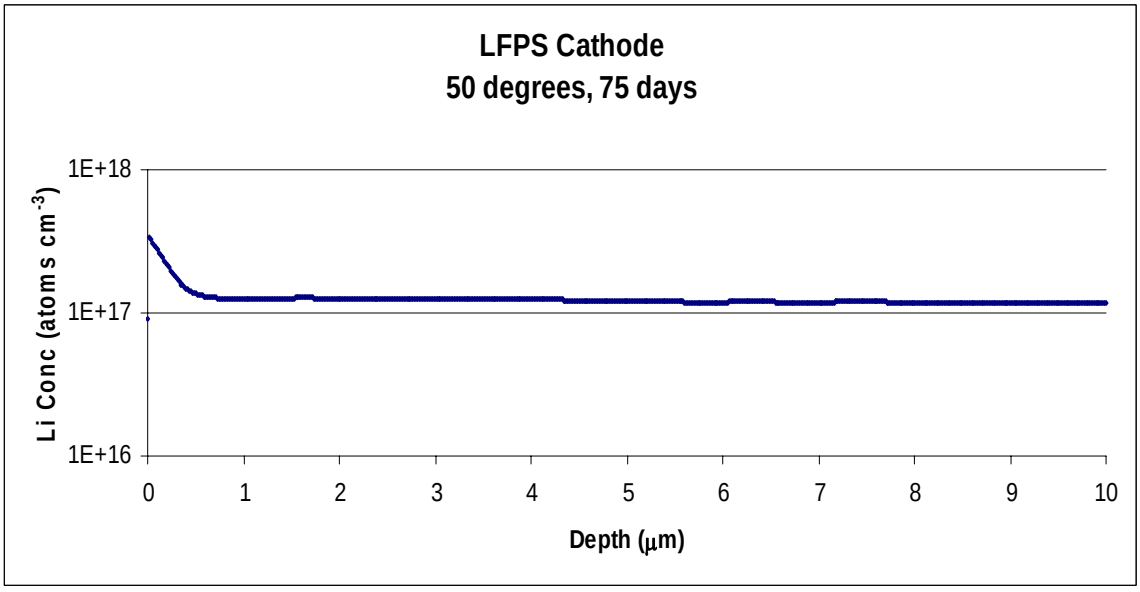

Figure 5.12: UT-NDP profile of LFPS cathode as estimated with no energy broadening at the surface. The profile is presented in log scale for better comparison with the SIMS profile.

Comparison of the UT-NDP profile and the SIMS profiles show that the shape of the distribution, or absence of any major features, is the same for both profiles. After the first 500 nm, both profiles show a uniform concentration distribution throughout the rest of the profiled depth. Once again, we see the contrast between the normal NDP profile and the SIMS profile at the surface due to energy broadening effects. Another profile with the energy broadening effects taken away is given in figure 5.12 to show that both profiles measure a concentration gradient very close to the surface.

Conclusion

Comparison of the NDP and SIMS techniques was difficult due to specific attributes of each technique. The SIMS technique was not able to determine a specific sputtering rate, and in return there is no way to accurately measure depth from the data given. The NDP technique broadens the energy in such a way that concentration near the surface gets spread out into depths "above" the surface and consequently causing specific features of the profile to disappear. However this effect can be remedied with knowledge of the system energy broadening, and the results of this correction have been shown.

By simple visual comparison of the SIMS data to that from the UT-NDP system, there are no significant differences between the profiles. Similar samples to those shown in this section have also been profiled with the NIST-NDP system and have produced the same results of the UT-NDP results shown here. Therefore it is accurate to claim that the profiles produced by the NDP and SIMS systems are valid representations of the lithium distributions within those samples.

Furthermore, it should also be stated that NDP has produced the profiles in this section that are very similar to those of SIMS, but without the limitations of an unknown sputtering rate, or the threat of fast migration. Fast migration is the primary reason why SIMS is not performed on samples such as the LFPS oxide sample. This is the threat of

inducing migration of the profiled ions due to the method of profiling. The low energy of incident neutrons in NDP results in a very low risk of this effect, however when using SIMS to profile materials that ions are very mobile in, such as an oxide, there is a high risk of ion migration. For this reason, SIMS profiles of such materials cannot have an extremely high confidence level in their credibility. This threat is not relevant for NDP.

Table 5.4: Advantages and disadvantages of NDP vs. SIMS observed from this study for profiling of lithium ion cells.

NDP		SIMS	
Advantages	Disadvantages	Advantages	Disadvantages
Non-destructive, no risk of fast ion migration, higher confidence in results	Lower depth resolution, longer count times (for UT system), energy broadening effects	High depth resolution, Wider ranges of profiled elements	Destructive, Possible fast ion migration, sputtering rate may vary (increases uncertainty in depth)

UT-NDP PROFILE AND MCNPX MODELS

A model of NDP was designed with the Monte Carlo n-Particle Code (MCNPX) to better understand the following:

- Is the UT-NDP facility producing accurate profiles?
- Will the graphitic composition of commercial anodes that are analyzed in areas of this research distort the profile and produce inaccurate surface results?

The MCNPX model designed to simulate NDP has a simple geometry with the detector face directly facing the sample. A thermal neutron beam with a 3 cm radius is

incident on the sample. The beam thermal neutron energy is uniform across the entire 3 cm radius of the beam. The beam, sample, and the detector are along the same axis. This is no problem since we will not see any noise contribution from the neutrons in our alpha tally at the detector. The beam size was chosen to cover the entire area of each sample that was modeled.

The geometry of the model can be seen in figure 5.13. The model includes a 100 μm thick silicon detector, the sample, the neutron beam, and a 72.1 cm tall aluminum cylinder that is the NDP chamber. The chamber is filled with an extremely low atmosphere of air. A void is modeled outside of the chamber. The MCNPX deck may be found in appendix A.

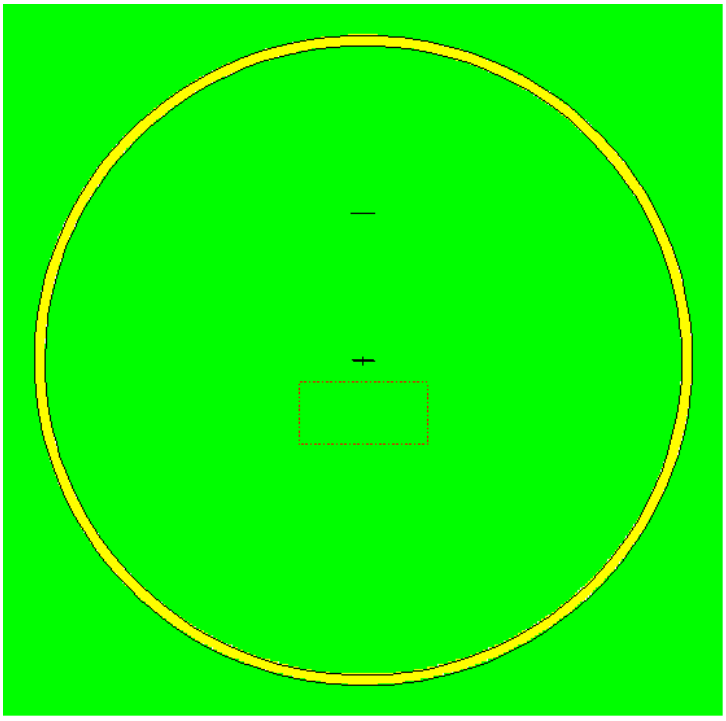

Figure 5.13: Geometry of the MCNPX model. The yellow circle is the top view of the NDP chamber. The origin of the neutron beam, the sample, and the detector are all along the same axis, seen vertically here.

The first model developed was a 2 μm thick borosilicate wafer with a uniform distribution of ^{10}B throughout the entire depth of the wafer. This sample was chosen because it is similar to the Standard Reference Material (SRM) 93a that is often used for an alpha energy calibration of the UT-NDP system. Profiling of this sample measures the energy spectra of two alpha particles emitted after neutron absorption. An alpha particle with 1471.76 keV is emitted 93.7% of the time while an alpha with 1775.87 keV is emitted the other 6.3%. The objective of modeling this sample was to compare the energy spectra from the model to that of a profile from the UT-NDP system.

A comparison of a spectrum produced by the MCNPX model to that of experimental data from the UT-NDP facility is shown in figure 5.14. The figure shows that the two spectra match well even at the data's vertical step in counts at 1471.76 keV that is a measure of detector resolution. The broadening that appears in the experimental data is a result of the energy broadening of the detector. The MCNPX spectrum shows that the model is accurately modeling the energy broadening of the UT-NDP system.

The ratio of counts from the primary and secondary alpha particles is similar within both spectra. Overall the similarities in energy and concentration measurements between the spectra show that the UT-NDP facility is producing credible charged particle measurements.

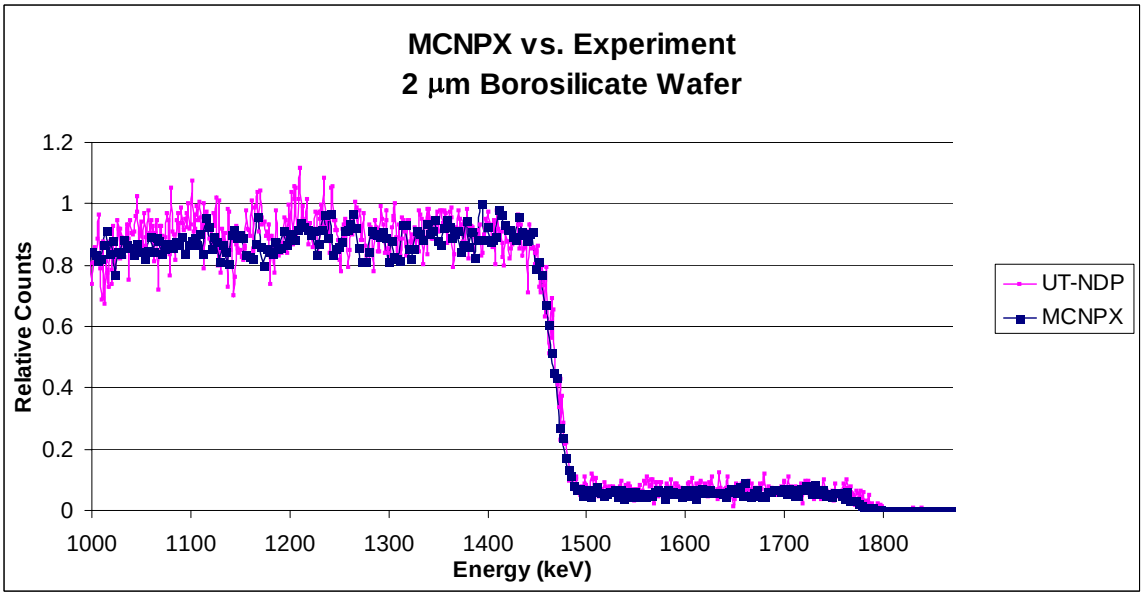

Figure 5.14: Comparison between alpha energy spectra of MCNPX model vs. that of experimental data from the UT-NDP facility. The spectra match well in terms of distribution shape as well as detector resolution.

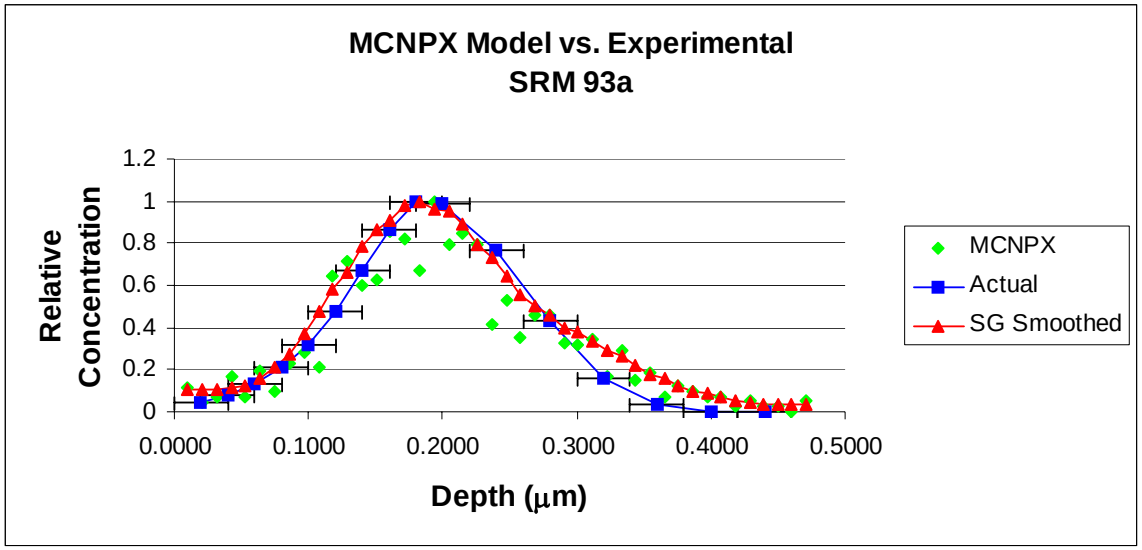

Figure 5.15: Comparison of MCNPX data, MCNPX smoothed data, and the actual depth profile of the sample. This figure shows that SG smoothing produces accurate profiles.

The second sample modeled was designed to mimic the SRM 2137. The SRM 2137 sample is a boron doped silicate sample that is often used for concentration calibration of the UT-NDP system. To model the non-uniform ^{10}B distribution throughout the sample, multiple sample cells were modeled that each share a surface. Each cell was 20 nm thick and contained a different ^{10}B content than the others. The depth profile formed from the MCNPX alpha energy spectrum and that from experimental data is shown in figure 5.15.

The figure shows data from the MCNPX energy spectrum tally, the actual distribution of the sample that was modeled, and the MCNPX data smoothed by Savitzky-Golay (SG) smoothing. Error bars representative of a typical 20 nm resolution are placed on the actual data to show that SG smoothing produces an accurate profile even without exceptional counting numbers. The average number of counts per channel for the MCNPX spectrum was 20.

The final sample to be discussed was a 2 μm thick graphite wafer doped with ^{10}B. The ^{10}B distribution is uniform across the entire depth of the wafer. This sample was modeled to determine if the graphitic matrix of the sample would distort the energy spectrum from the surface. What is expected is a similar energy spectrum to that of the SRM 93a, unless the graphite does have a negative effect. As shown in figure 5.16, the alpha energy spectrum from the graphitic wafer is very similar to that of the SRM 93a sample.

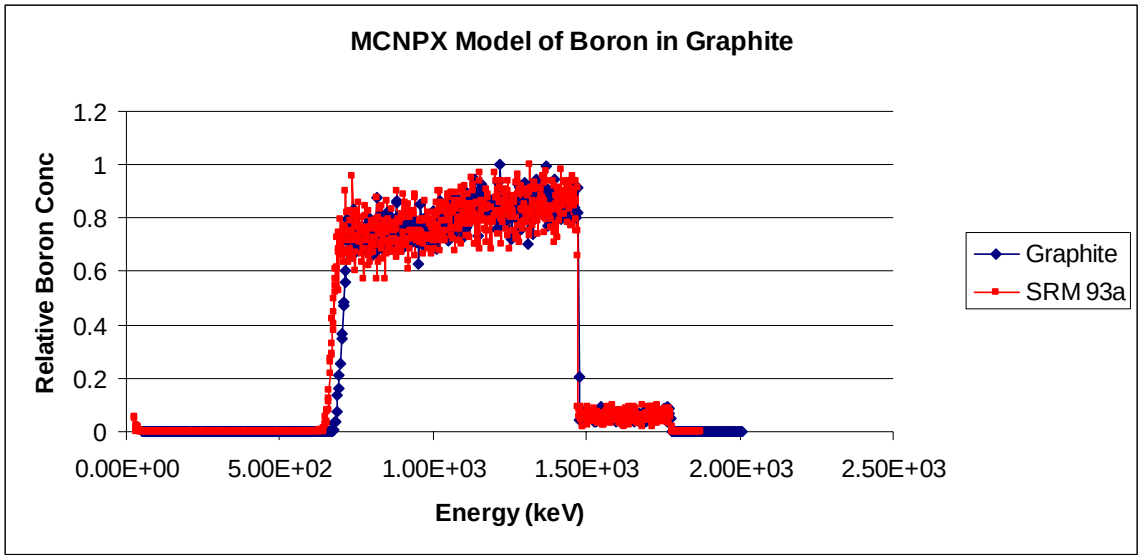

Figure 5.16: Comparison of the alpha energy spectra from MCNPX models of a graphite matrix and a silicate matrix that are doped with ^{10}B.

The two energy spectra share the same spread in surface energies of 2.1 keV. This suggests that the graphite matrix is not having a negative effect on the ability to obtain an accurate energy profile from the surface. The spectra shown will both produce uniform depth profiles across the entire depth of the sample. The disparity between the spectra at the low energy drop in counts is due to the differences of the sample matrices. The graphite counts drop off before the SRM 93a counts because the lower density of the graphite causes a smaller energy loss of the alpha particles across the entire thickness of the sample. This difference in the spectra is further validation of the model's accuracy.

The first derivatives of the SG smoothed data from the surface energy spreads of the graphite and SRM 93a samples are shown in figures 5.17 and 5.18. The energy spread is determined by finding the FWHM of the Pearson distributions fit to the derivatives. These models have helped to validate that NDP of the graphitic anode samples in this study will produce accurate profiles without surface distortions.

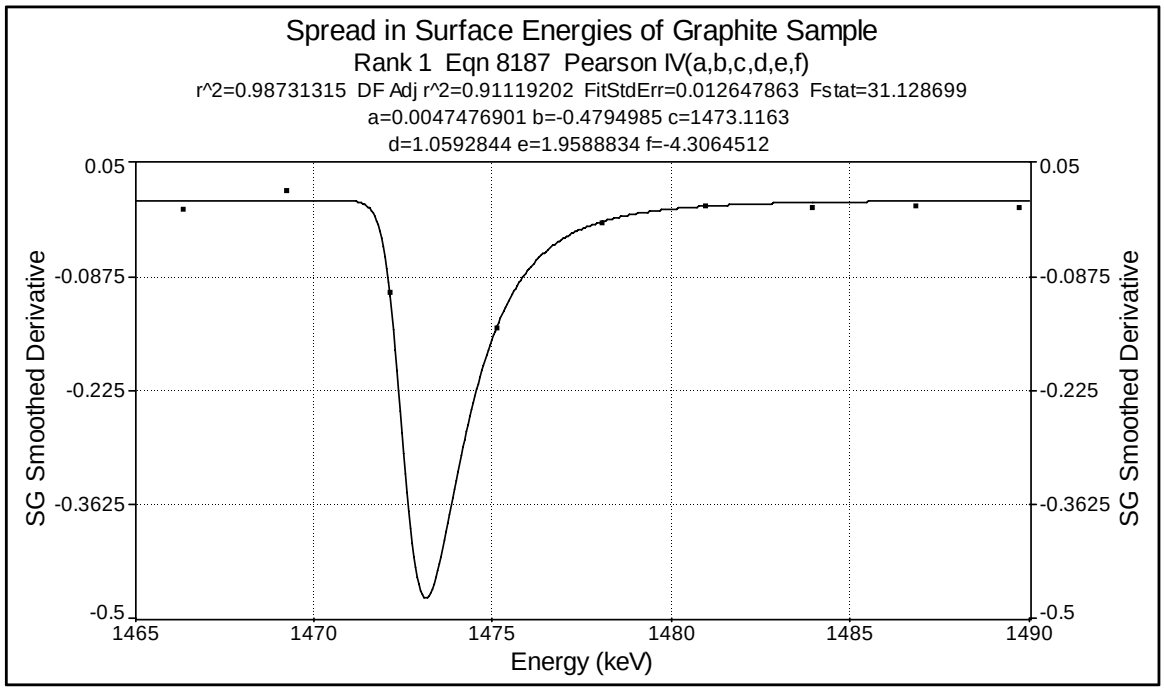

Figure 5.17: This is the first derivative of the surface energies from the graphite sample. The spread in surface energies is 2.1 keV.

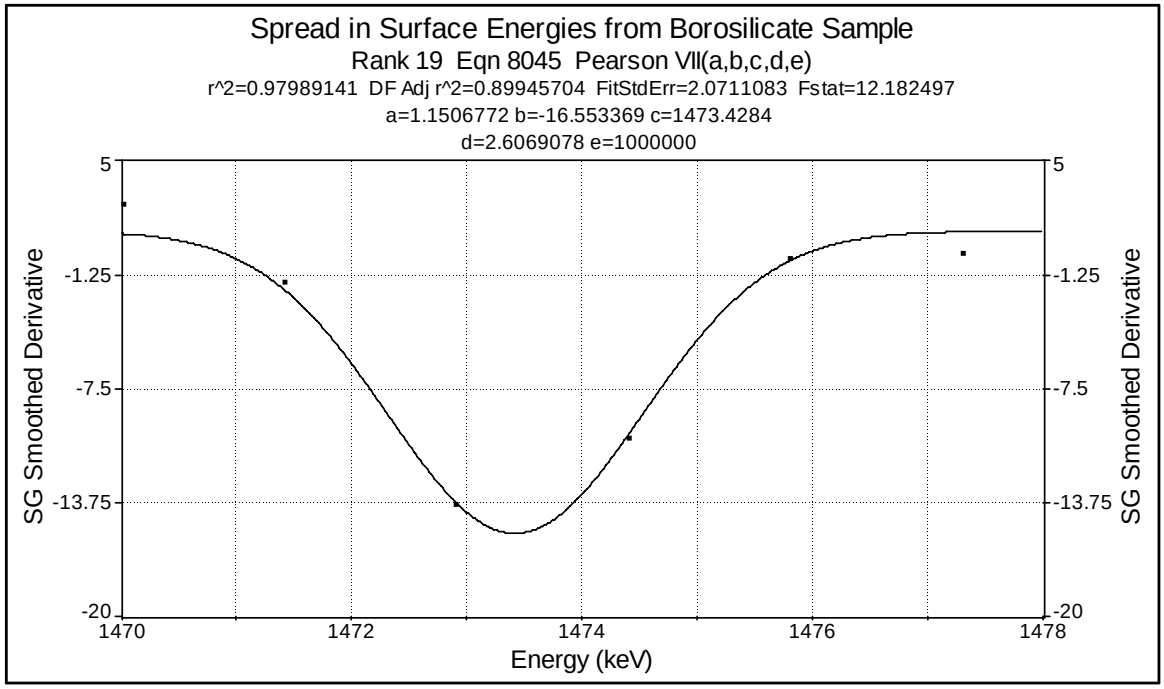

Figure 5.18: The first derivative of the surface energies from the SRM 93a sample. The spread in energies is 2.1 keV.

Conclusion

The MCNPX models were extremely useful for the following: benchmarking ratio of concentrations and shape of distributions for the UT-NDP facility, validating the SG smoothing method, and testing the surface profiling effects from graphite. One conclusion from analysis of the MCNPX models is that the UT-NDP facility is producing accurate profiles in terms of shape and concentration ratios. Furthermore, the SG smoothing technique was capable of producing depth profiles within error to the actual profile of the sample. Most importantly, the profile produced with the SG smoothing was done so with raw data having only 14% statistics in the number of counts. Yet, the SG method was still capable of producing an accurate profile. Finally, the MCNPX model was useful in evaluation of the absence of any negative surface effects created by using graphite as the sample material.

TRENDS AND REPLICATE DATA

Trends in the data and similar profiles of samples indicate that NDP does accurately profile the electrode samples with precision in both depth and concentration. Any type of stochastic or erratic behavior in the profiles of similar samples would suggest that false information is being gained. Over 40 profiles of cell electrodes were measured for this research and there are no signs of erratic data. These profiles and the trends created by their data will be discussed in detail in the next chapter, and the reader may consider this the final method of validation for the use of NDP towards lithium ion cell electrode research.

Chapter 6: NDP Applications to Lithium Ion Battery Electrodes

Application of NDP to battery electrodes exposed to varying conditions has allowed for the analysis of how the mobile lithium ions within that battery are behaving. Since a thorough investigation, as described in the previous chapter, has been conducted to determine the accuracy and repeatability of NDP measurements for these electrodes, one can be confident that the results are credible. Hopefully, the initial hypotheses that were confirmed and those that were rejected will act as an example of the new perspective that NDP offers. The advantage of NDP over other analytical techniques for this type of analysis should open new doors for its use as a unique tool in the electrochemical community.

The reader will see that the experimental methods of conditioning these cells have close similarities to those that a battery might experience through the use of a normal user. These methods have all been chosen due to their frequent appearances throughout lithium ion battery literature [3, 4, 11, 41].

STORAGE OF CELLS AT TEMPERATURE

Previous studies [4] into the degradation of the solid electrolyte interface (SEI) at various temperatures have attempted to quantitatively analyze the variation of the SEI at temperatures of 25, 40 and 60 ºC. The SEI has been found to degrade over time, and this effect is thought to be amplified by temperature [50]. As the SEI degrades it becomes thicker, the increase in thickness is produced by the activity of lithium in side reactions. As lithium is consumed in side reactions, this results in less lithium that is usable by the cell, and so the capacity of the cell decreases. Therefore, SEI breakdown may be the cause of the decrease in capacity retention seen in figure 6.1. Yoshida *et al.* have used the

techniques of focused ion beam (FIB), scanning electron microscope (SEM), and X-ray photoelectron spectroscopy to try and quantify the degradation of the SEI due to temperature. They were also investigating the proposal that the life of the lithium ion battery is degraded in proportion to the square root of the storage time (1/2 rule) [51] . There are two primary points of Yoshida *et al*'s work for the reader to take note of:

1. The Yoshida study investigated spinel $Li_{1.1}(Ni_{0.025}Ti_{0.025}Mg_{0.02})Mn_{1.83}O_4$ cells to analyze the SEI degradation. However, by choosing a cathode containing Mn, another mechanism for surface reactions other than just SEI formation is present. This mechanism occurs because trace amounts of water exist within the electrolyte. Reaction between water and the $LiPF_6$ salt in the electrolyte produce HF as a reaction product. HF dissolves the Mn of the cathode by the following reaction,

$$2Mn^{3+} \xrightarrow{H^+} Mn^{4+}(solid) + Mn^{2+}(solution) \qquad (6.1)$$

The Mn^{2+} cation is very mobile and can cross the separator towards the anode. The Mn^{2+} then acts as a poison to the anode by plating onto its surface. This type of Mn dissolution is believed to be a major cause of capacity fade [11, 52-54].

The authors were aware of the possibility of Mn plating onto the anode and took steps to measure its influence on their measurements. But it was left unclear if the Mn plating had a role in the SEI and capacity fade measurements by the group.

2. The group required two analytical techniques, focused ion beam (FIB) and X-ray photoelectron spectroscopy (XPS), to be used in tandem to determine an approximated thickness of the SEI layers. FIB analysis would

have required too much time to determine the thickness, and XPS cannot determine thickness of the SEI on its own. Therefore the group combined data from the techniques to provide SEI thickness. Their method of combining the technique was ambiguously described, at best. Their findings were that the SEI was initially 0.04 μm thick, and that this thickness increased to 0.45 μm after 392 days at 40ºC. Their results of SEI thickness increase are shown in figure 6.1 along with the correlating capacity decrease in figure 6.2.

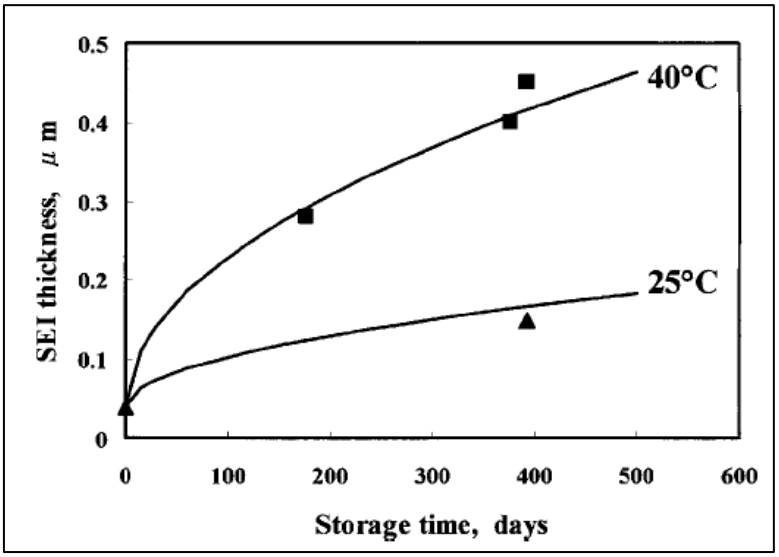

Figure 6.1: Yoshida *et al*'s values of SEI thickness as it varies with time and temperature [4].

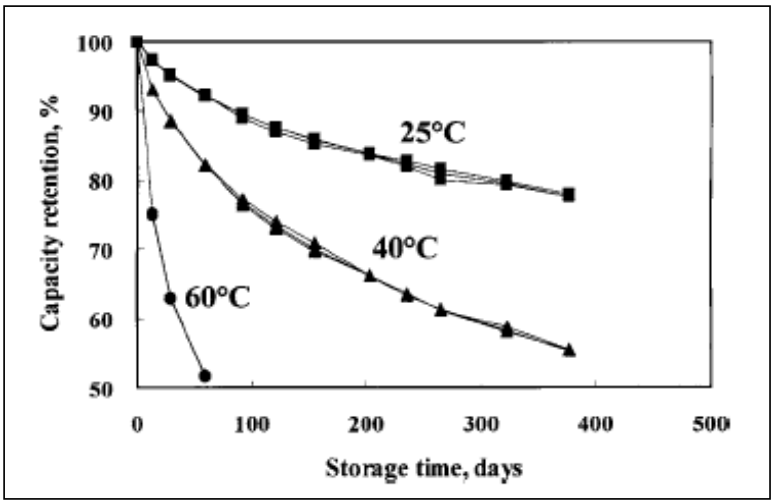

Figure 6.2: Yoshida's investigation into the decreasing capacity of batteries after storage in different temperatures shows significant effect of the temperature [4].

For this study, cells have been stored at 50 ºC for 75 and 140 days. The temperature of 50 ºC was chosen since it was found in prior studies [51, 55] to be sufficient for noticeable change in the SEI to be determined over storage time. The cathode compositions of the cells stored were $LiFePO_4$ (LFP) and $LiFePSO_4$ (LFPS) commercially manufactured cells.

Primary objectives of this section of the research are,

1. Show that NDP is capable of measuring SEI thickness without the necessity to combine two different analytical techniques as Yoshida *et al.* required.
2. Determine if SEI thickness is increased over time in lithium ion cells that do not contain Mn in the cathode. This will be the first direct relative concentration vs. depth measurements of the SEI known to the author. The absence of the Mn dissolution mechanism will help to validate or negate the trends determined by Yoshida's group and show that they are a direct result of SEI activity and not affected by Mn. Furthermore, any trends found will show that the results found in the Yoshida study are not limited to the spinel $Li_{1.1}(Ni_{0.025}Ti_{0.025}Mg_{0.02})Mn_{1.83}O_4$ cathodes.

Experimental

Commercially manufactured $LiFePO_4$ (LFP) and $LiFePSO_4$ (LFPS) batteries were purchased. The cells were 18650 type cylindrical cells with 1350 mAh capacity. The max cell voltage is 3.2 V. The LFP and LFPS cells are designed for high power applications such as for hybrid electric vehicles (HEV). If included in this type of application, these cells would be exposed to high temperatures that can affect the cell's performance over time. For this reason, these types of cells were chosen to investigate the behavior of the SEI after storage in 50ºC temperatures.

The graphite anodes were a mixture of synthetic graphite flakes (d_{50}= 22 μm) and mesocarbon microbeads (d_{50}= 10.2 μm). The anode composition consisted of 90 w% graphite and 10 w% poly(vinylidene fluoride) (PVDF) binder [56]. Calculation of the stopping power for these samples was based on this composition.

The batteries were stored in a 50ºC environment. The 50ºC environment was a drying oven kept at constant temperature over the entire period of storage. Storage times for the cells included 0, 75, and 140 days. At each time interval, cells were taken from their environment and disassembled according to the procedure previously described. Cathode and anode materials were taken from each cell and analyzed by NDP.

Performing NDP of these samples was by a large amount the most difficult for this research in terms of count time and analysis. Due to the low lithium concentration, count times for anode samples profiled with the UT-NDP system were approximately 60 hours of neutron flux at 950 kW. Since the UT reactor is only operational for 8 hours at a time, this equates to 1 and ½ weeks of counting at a minimum for each sample. The final two anode samples (140 days) were profiled at the NIST-NDP facility due to lack of reactor time at the UT-NDP facility. The NIST-NDP facility provided very good spectra and only required ~10 hours of count time for each sample.

Results

The energy spectra measured from the NDP of the anode samples were analyzed for their alpha profiles rather than the triton profiles as in the other sections of this report. The alpha profiles were used for analysis of the SEI due to the higher depth resolution of the alpha particle and also because the SEI is located on the surface of the anode, so a large maximum depth of profiling was not necessary. The depth resolution of the alpha in the graphite is ~84 nm close to the surface.

As shown in figure 6.3, the energy spectrum of the graphite anode provides data from the triton counts as well as the alpha counts. The counts from triton detection appear at the higher channels of the spectrum and then begin to combine with the alpha counts at the peak near the middle of the spectrum. Due to this interference of the triton counts with the alpha counts, analysis of the alpha counts required that the triton counts be filtered from the spectrum. Filtering could be done by determining an alpha energy spectrum from the depth profile of the triton counts, but this method would lose valuable information due to poor triton resolution. A second method is to use a 3 μm polyethylene film placed over the sample to shift the alpha spectrum to lower energies and allow the "originally" hidden behavior of the triton counts to be seen. The slope of the triton counts can be determined and used to filter the triton counts from spectra of the same sample recorded without the polyethylene film. The approximation of this method requires that only relative lithium concentrations be assigned to depth intervals, since assigning atomic concentration values could not be completely reliable. However, the method does provide accurate information about the shape of the distribution, and since the objective is depth determination, this is most important.

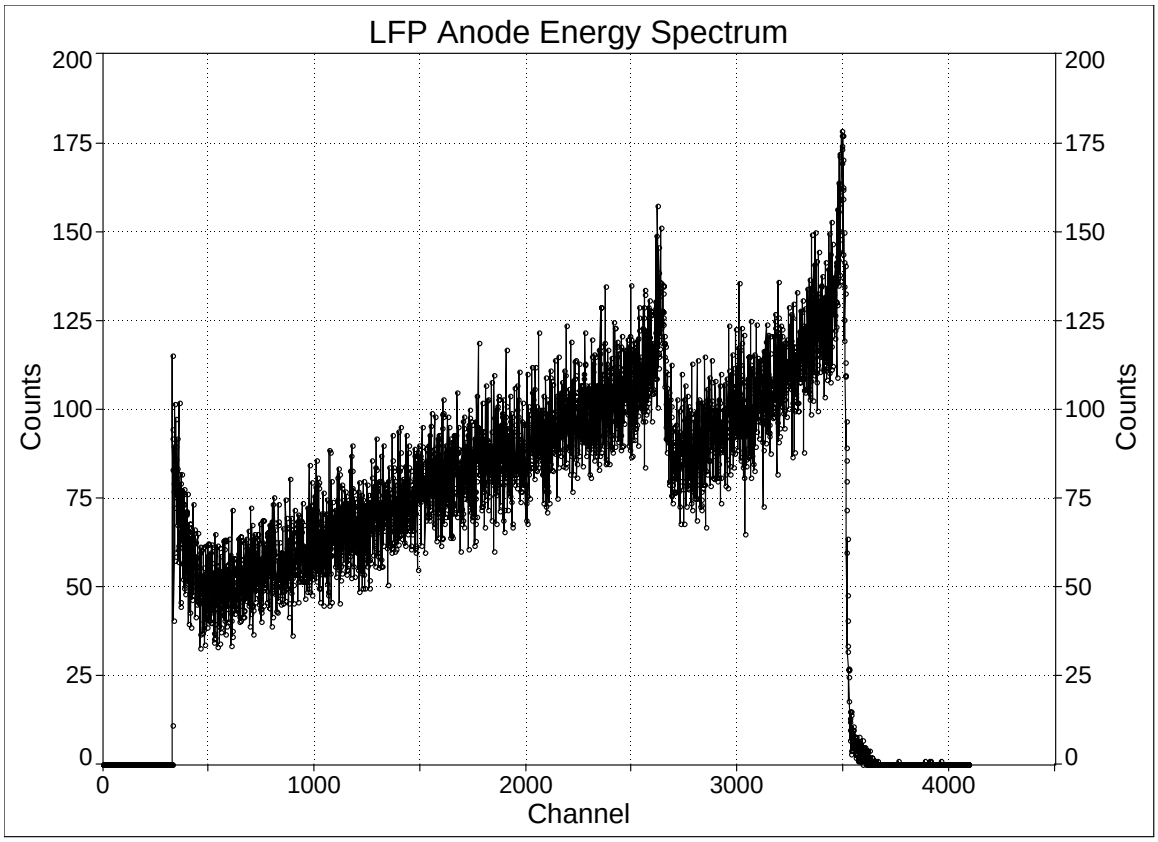

Figure 6.3: Energy spectrum of a graphite anode determined by NDP.

The profiles of the NDP analyzed graphite anodes from $LiFePO_4$ (LFP) and $LiFePSO_4$ (LFPS) cells are shown in figures 6.4 through 6.9. Anodes from each type of cell were analyzed at 0, 75, and 140 days for their SEI thickness. The thickness was determined to be the depth from the surface to the depth of the second zero of the first derivative for the smoothed data. The first zero of the derivative will belong to the maximum of the alpha profile, and the second zero marks the point at which a uniform concentration distribution is typically seen to begin. Only relative lithium concentrations are given due to the triton count filtering procedure.

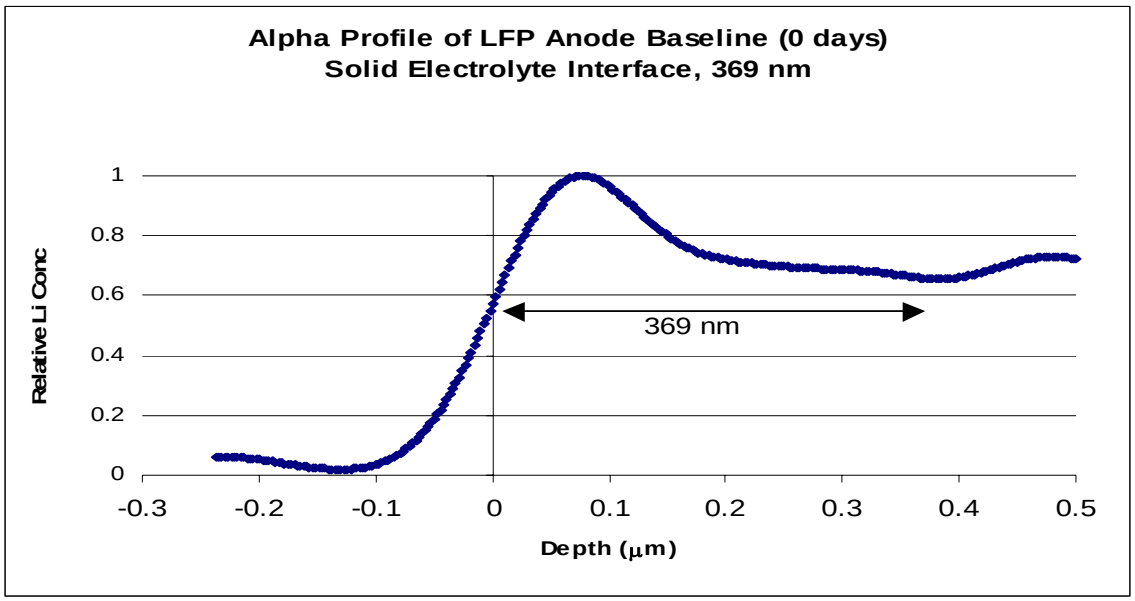

Figure 6.4: Depth profile of the SEI from an LFP anode after 0 days of storage.

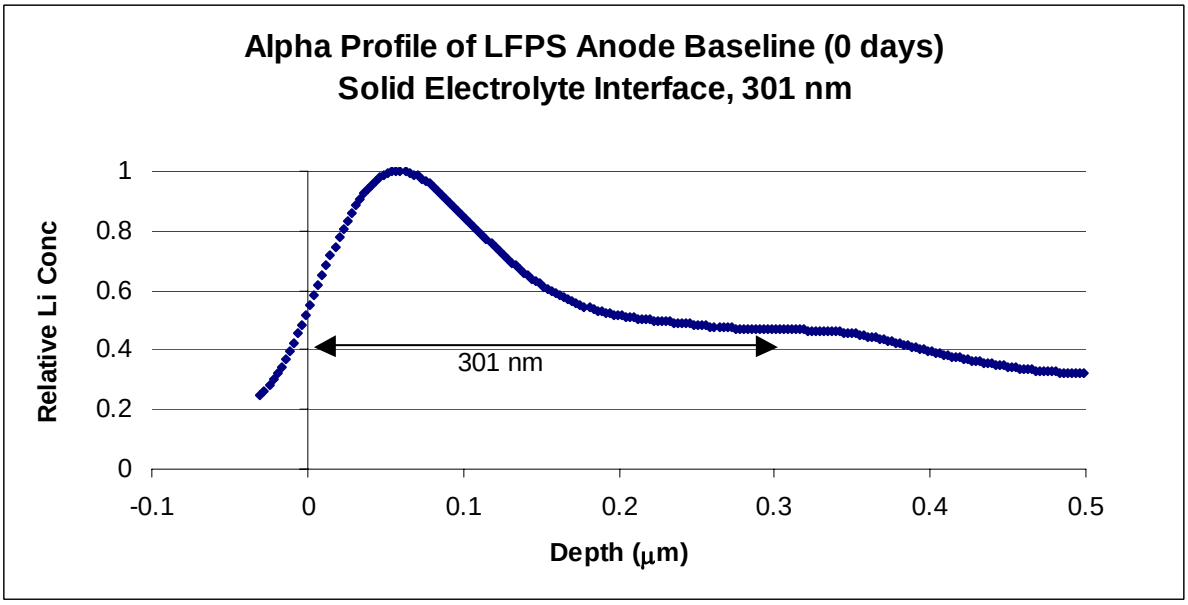

Figure 6.5: Depth profile of the SEI from an LFPS anode after 0 days of storage.

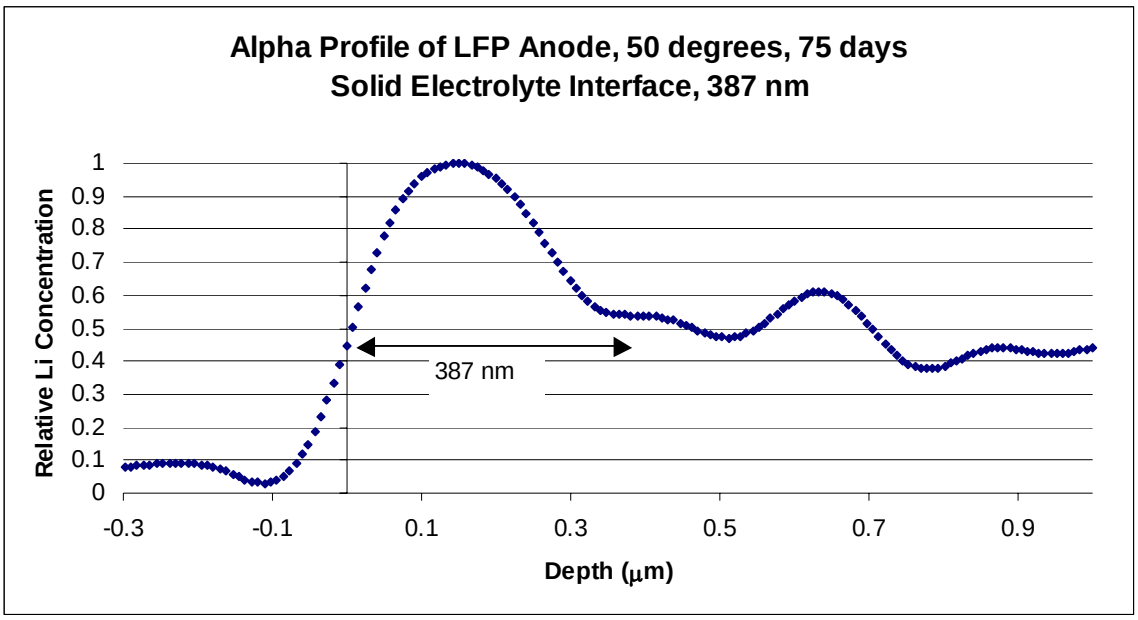

Figure 6.6: Depth profile of the SEI from an LFP anode after 75 days of storage at 50ºC.

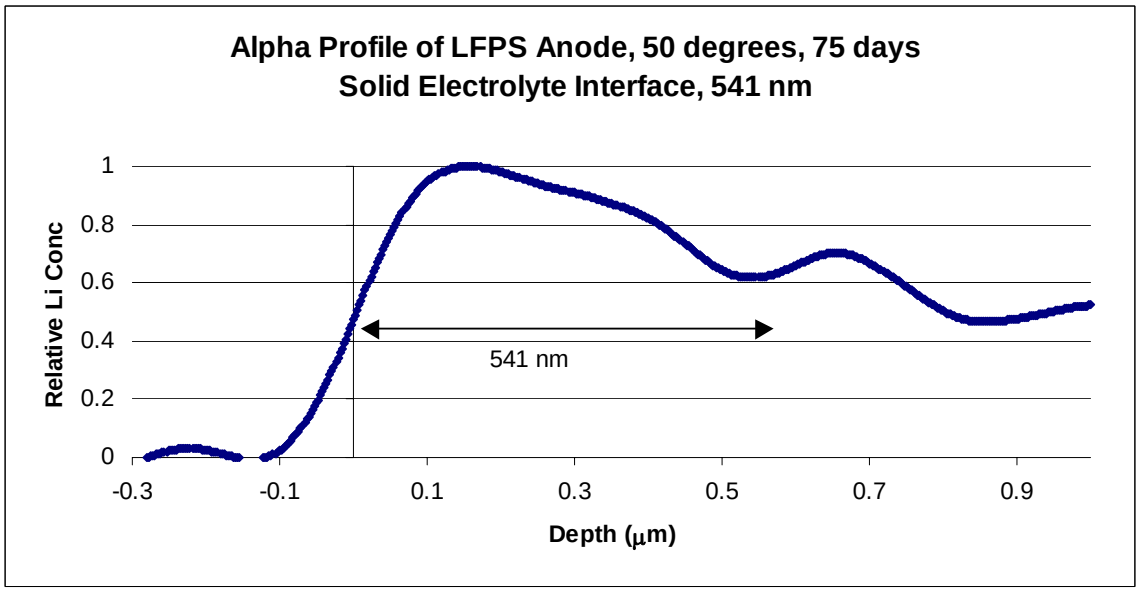

Figure 6.7: Depth profile of the SEI from an LFPS anode after 75 days of storage at 50ºC.

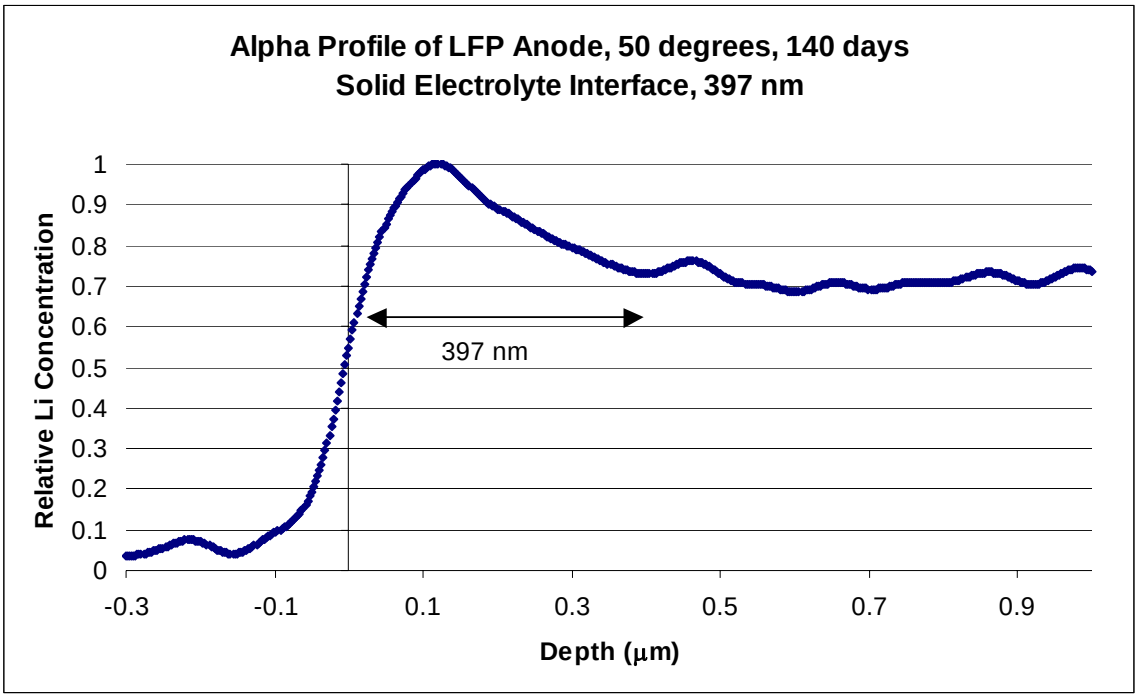

Figure 6.8: Depth profile of the SEI from an LFP anode after 140 days of storage at 50ºC.

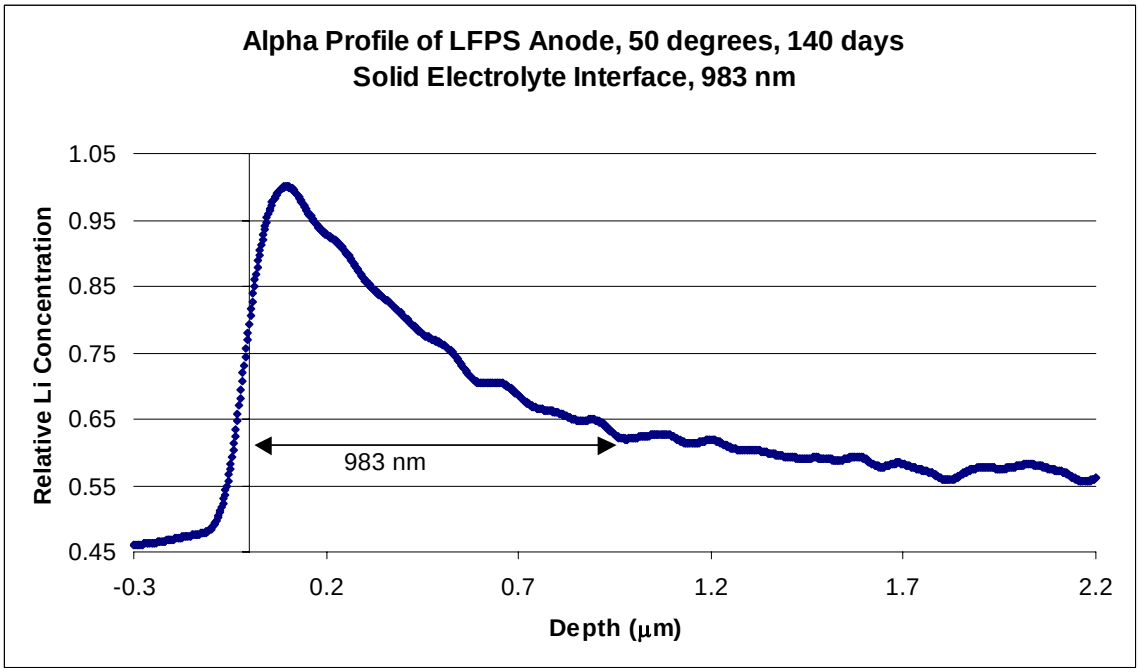

Figure 6.9: Depth profile of the SEI from an LFPS anode after 140 days of storage at 50ºC.

The results indicate that the SEI thickness was on the same hundreds of nanometer scale as found by Yoshida *et al.* for the spinel cell type. The determined values for each SEI thickness are listed in table 6.1.

Table 6.1: Values of SEI thickness as profiled from the anode of different cells types stored at 50ºC.

Cell Type	Days	0	75	140
LFP	SEI thickness (nm +/- 42)	369	387	397
LFPS	SEI thickness (nm +/- 42)	301	541	983

There is a clear trend of the SEI increasing in thickness as storage time increases. The trend is shown in figure 6.10. Both trends show a positive slope of SEI thickness as a function of storage time at 50ºC.

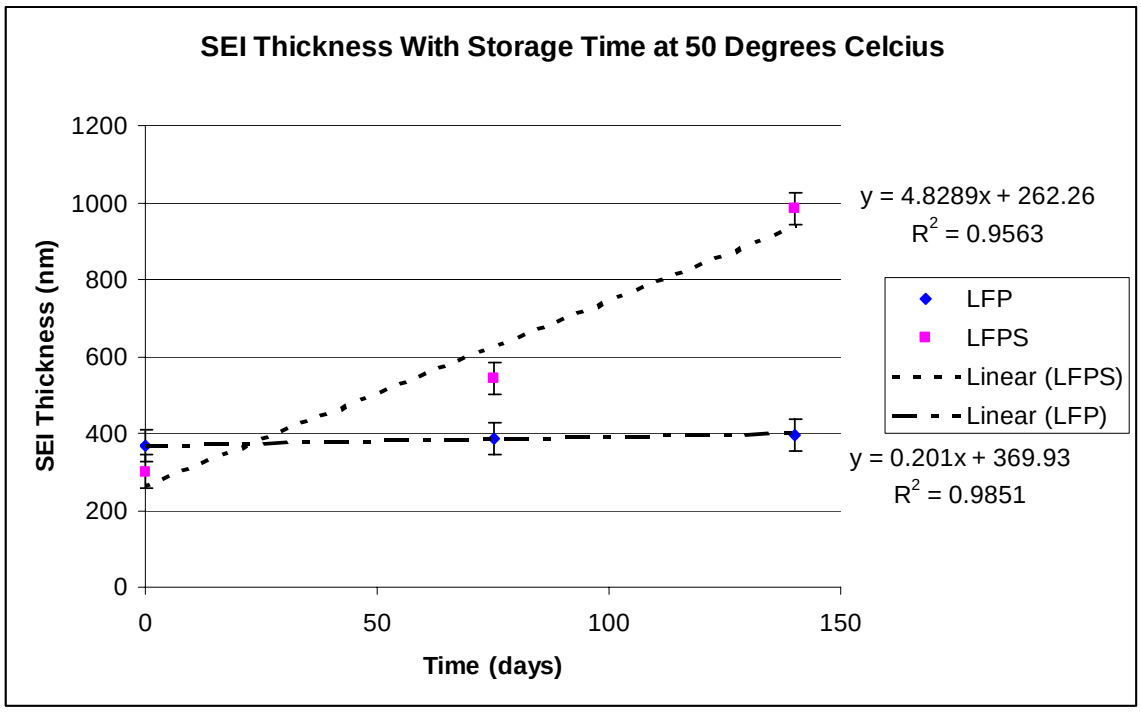

Figure 6.10: The trends of SEI growth in LFP versus LFPS anodes indicate that both trends have positive slope, but that the LFPS SEI thickness has a much greater rate of growth.

While both types of cell types show SEI growth, the rate of growth for the SEI of the LFPS cell is 4.8 nm per day while that for the LFP cell is 0.2 nm per day. The LFPS SEI growth rate is a factor of 21 times greater than that of the LFP cell. Both slopes of the trendlines from figure 6.10 are positive and show that the growth follows a linear relationship with time.

Conclusions

The higher rate of SEI growth for the LFPS type cell will correspond to higher capacity fade of the LFPS cell due to loss of lithium. Similar correlations are shown in figure 6.2 from the Yoshida study. This indicates that the LFPS cell is losing more capacity per day than the LFP cell due to side reactions involving lithium near the anode

surface. Therefore it is of the author's opinion that the LFP type cell would be more suitable, in terms of capacity fade from SEI growth, for an application involving high temperatures such as an HEV.

This research has determined the SEI thickness of lithium ion cell anodes with only the use of the NDP technique. The results have shown that the trend for the SEI thickness is to increase with storage time in a 50ºC environment. This will correspond to a capacity fade within the cell as well. The results found by this research correspond well to those found by the Yoshida *et al.* study, but the results of this study due not incorporate the approximations of combining techniques. This study has also determined SEI thickness directly while avoiding any conflicting mechanisms to anode plating such as Mn dissolution.

CELL CHARGE/DISCHARGE CYCLING

The normal use of lithium ion batteries includes the continuous discharging and charging of the cell. Each charge and discharge of a cell is a complete cycle. Even perfectly controlled cycling of a cell will still result in a decreasing performance of the cell. This fault is perhaps the most well known defect of the lithium ion battery. It is called *capacity fade*. A large variety of research is conducted to explore the main cause of capacity fade. Possible explanations for capacity fade include overcharging or self-discharging of the cell, passivation of the cell, and phase changes that occur within the cell [11].

The main focus of this research was the passivation of the cell and its dependence on cell cycling. Passivation occurs due to lithium plating on the surface of the electrode near the electrolyte. The SEI layer that has been previously discussed is a form of passivation. This electrode-electrolyte interface can be passivated if lithium concentrates near the surface and has side-reactions that remove its ability to migrate throughout the cell. The passivation of cells has been researched [4], and shown to be closely linked to capacity fade.

The objective of this experiment was to determine if lithium was concentrating near the surface (within the first 2 μm) of $LiFePO_4$ (LFP) cathodes and the more recently developed $LiNi_{1/3}Mn_{1/3}Co_{1/3}O_2$ (LNMCO) cathodes after cycling. According to electrochemists involved in this research (John B. Goodenough research group), the understanding in the electrochemical community and the initial hypothesis for this experiment was that no lithium concentration near the electrode-electrolyte surface should be seen for these cathode materials.

Experimental

LFP and LNMCO cells were made in the lab as previously described in the experimental methods chapter. The cells were coin cells with lithium anodes. The cells were cycled with a precision current with the Arbin battery cycler. During each cycle, the current, voltage, discharge and charge capacity, discharge and charge energy, and maximum achieved voltage were recorded for the cell. This would allow any deviation from the hypothesis to be correlated to a change in capacity of the cell.

After being made, the cells were cycled by the Arbin battery cycler for 1, 10, 50, or 100 cycles. The cells were then disassembled and analyzed by NDP. The cell's capacity will vary with cycle number. An example of this for an LNMCO cell is shown in figure 6.11.

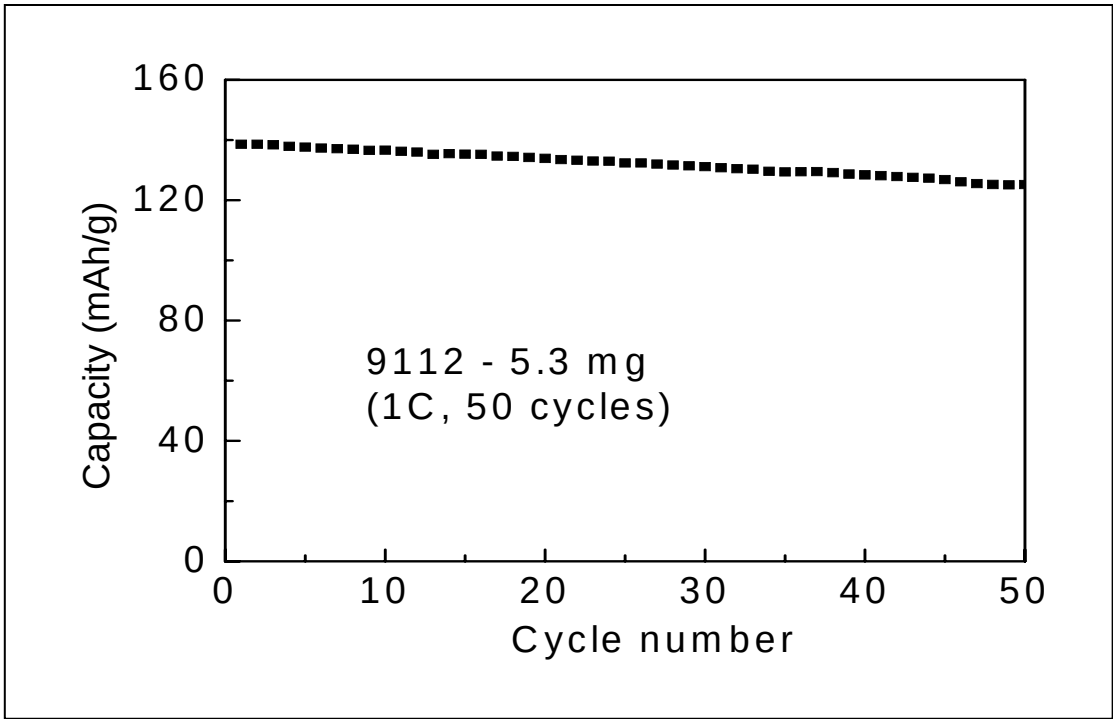

Figure 6.11: A cycled LNMCO cell. The graph shows the decreasing capacity of the cell as the number of cycles is increased.

Results

$LiNi_{1/3}Mn_{1/3}Co_{1/3}O_2$ (LNMCO) lab made cells were cycled 1, 10, and 50 times before being profiled with NDP. The cathodes were depth profiled for the lithium distribution of the first 10 μm from the electrode-electrolyte surface. The initial hypothesis was that lithium ions should uniformly diffuse and distribute the lithium concentration uniformly throughout the cathode. To test this hypothesis, the ratio of lithium within the first 2 μm compared to the total lithium concentration of the first 10 μm was determined. A uniform lithium distribution throughout the cathode would result in approximately 20% of the lithium being within the first 2 μm.

Depth profiles of the LNMCO cathodes are shown in figures 6.12 through 6.15. A baseline cathode that had not been cycled, or even built into a cell was first profiled to ensure that a uniform lithium distribution was initially present in the cells.

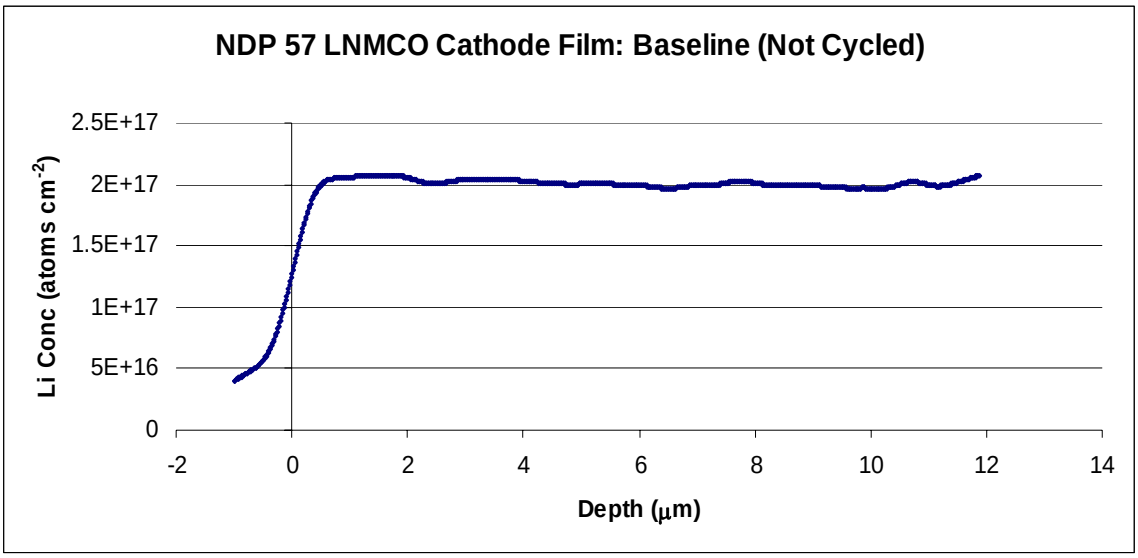

Figure 6.12: A baseline sample of the LNMCO cathode was profiled. The smooth profile shows that a uniform, and homogeneous, lithium distribution is present in the cathodes before the cells are cycled.

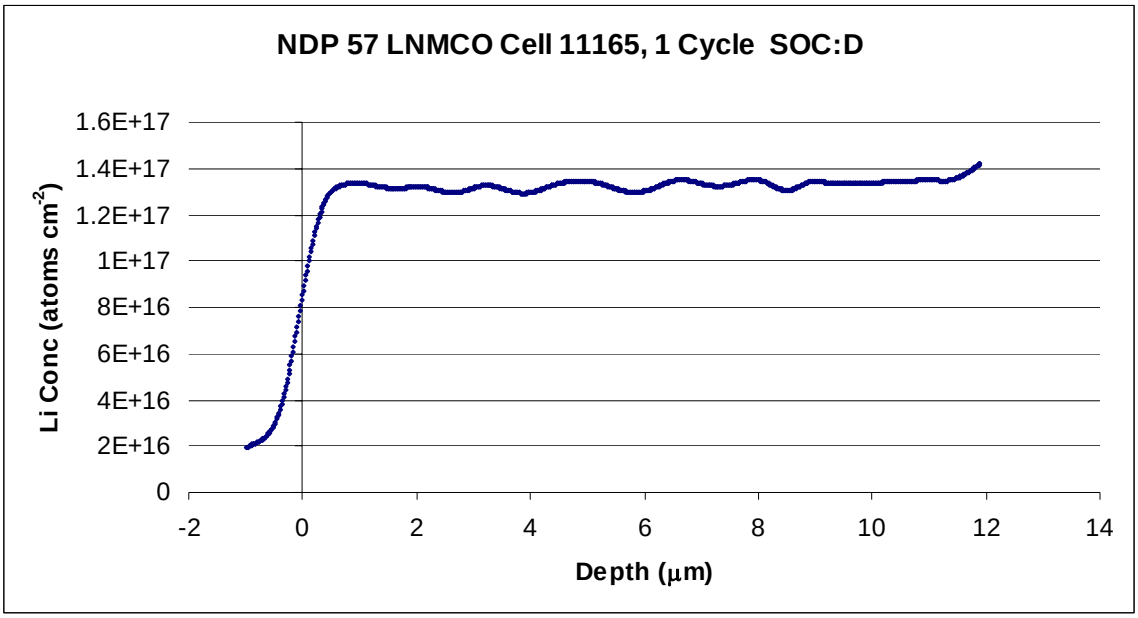

Figure 6.13: The profile of an LNMCO cathode that has been cycled once shows that a uniform lithium distribution is still present.

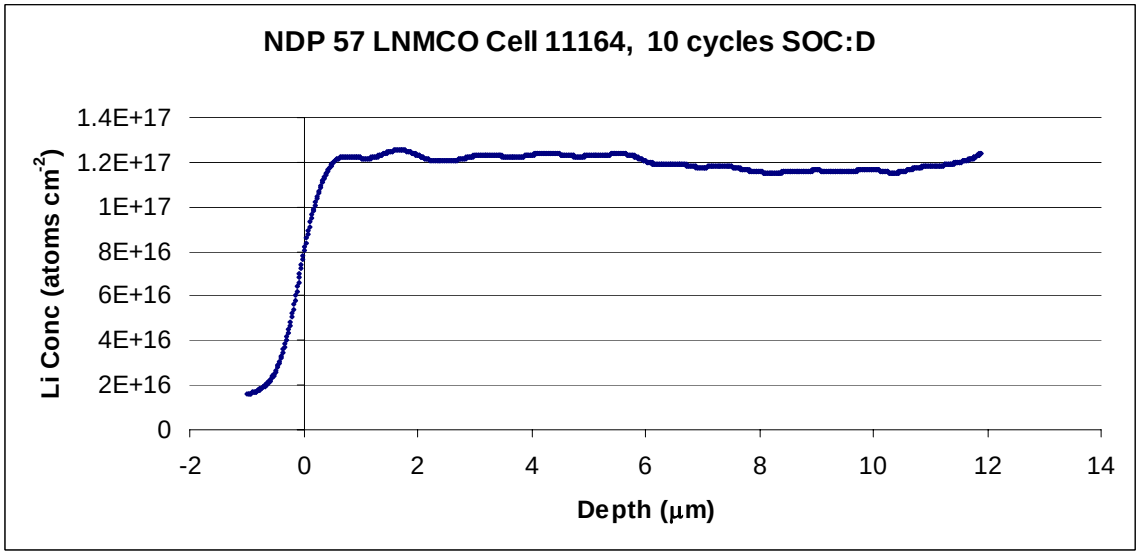

Figure 6.14: The lithium distribution is still uniform after 10 cell cycles.

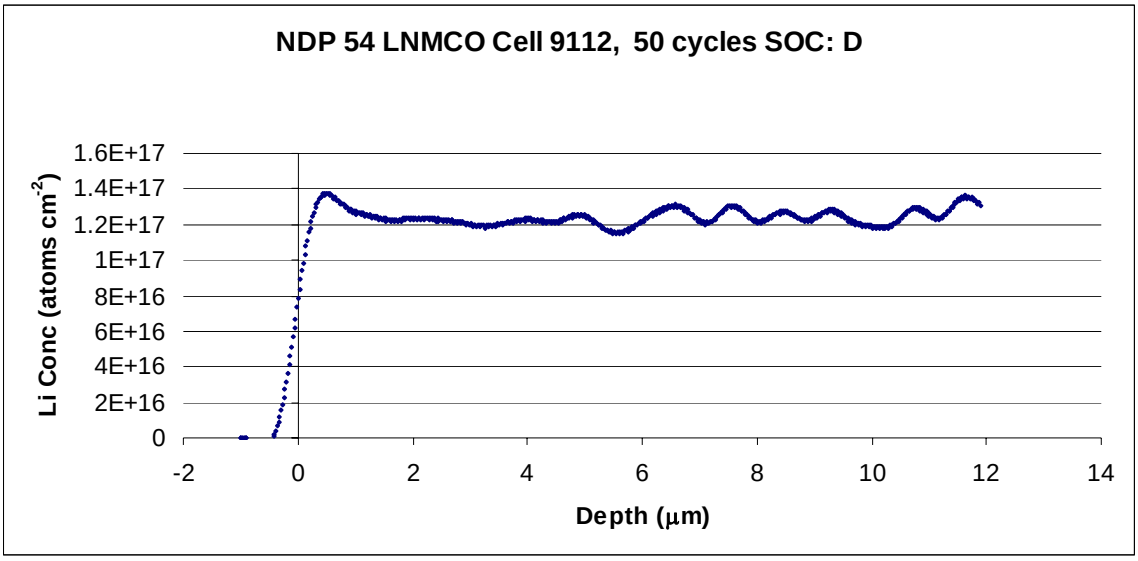

Figure 6.15: The LNMCO cathode has been cycled 50 times prior to this depth profile. Although capacity has decreased, the lithium concentration is still nearly uniform across the first 10 μm.

The baseline profile shows that the cathode films made in the lab did have initially uniform lithium distribution. Visual observation of the cathode profiles shows that no considerable changes in the lithium distribution occurs within the first 10 cycles of the cell. Some variation from the smooth profile of the baseline sample is shown from the profile of the cathode cycled 50 times as seen in figure 6.15. The bumps seen in the profile are likely not statistical, the reasons for the fluctuation in lithium distribution could include:

- The cathode film used in this cell was from a different film than the other cells (NDP 54 vs. NDP 57). Therefore, the mixing of this film may not have been performed as well as for the film of NDP 57. This could have produced a film with small variations in lithium distribution.
- The fluctuations in lithium concentration could be a result of the lithium being intercalated and deintercalated into the cathode material for 50 cycles. The

cycling process may have produced small structural changes to the cathode that have caused the lithium profile to fluctuate.

The lithium percentages within the first 2 μm of each cathode surface were compared in search of any correlation to the number of cycles. The results are shown in figure 6.16.

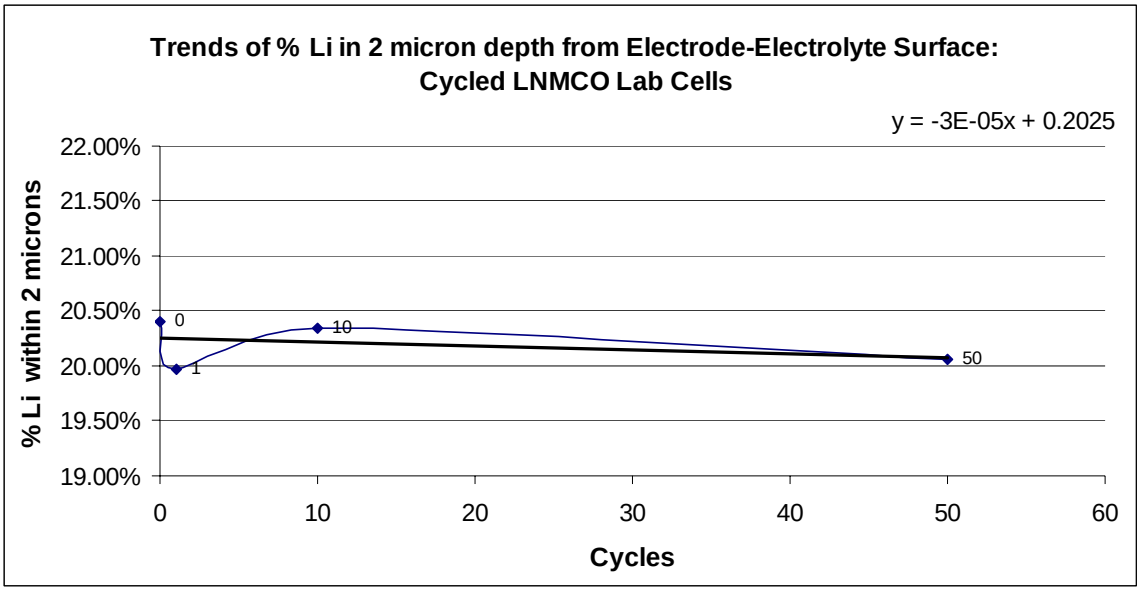

Figure 6.16: The trend shows no correlation of the lithium percentage within the first 2 μm of the surface with the increasing number of cycles.

Results show that there is not lithium buildup near the electrode-electrolyte surface as a result of cell cycling. The linear trendline fit to the data of figure 6.16 shows that no slope is present. Each value of lithium percentage in the first 2 μm deviates less than 0.41% from the predicted 20% value of the hypothesis. The maximum deviation was 0.41% and occurred in the baseline sample. The data shows that the hypothesis is verified for LNMCO cathodes. The lithium distribution remains uniform up to 50 cycles and there

is no positive slope in figure 6.16 to indicate that increasing the number of cycles would result in lithium buildup near the surface.

Lab made cells with $LiFePO_4$ (LFP) cathodes were cycled 1, 10, 50, and 100 times and then profiled to determine if lithium was concentrating within the first 2 μm of the electrode-electrolyte surface. Analysis of the profiles was performed in the same manner and just described for the $LiNi_{1/3}Mn_{1/3}Co_{1/3}O_2$ cathodes. The initial hypothesis for the $LiFePO_4$ cathodes was the same as that for the $LiNi_{1/3}Mn_{1/3}Co_{1/3}O_2$ cathodes; the lithium distribution should be uniform after cycling.

The profiles of the cathodes after cycling are shown in figures 6.17 through 6.20.

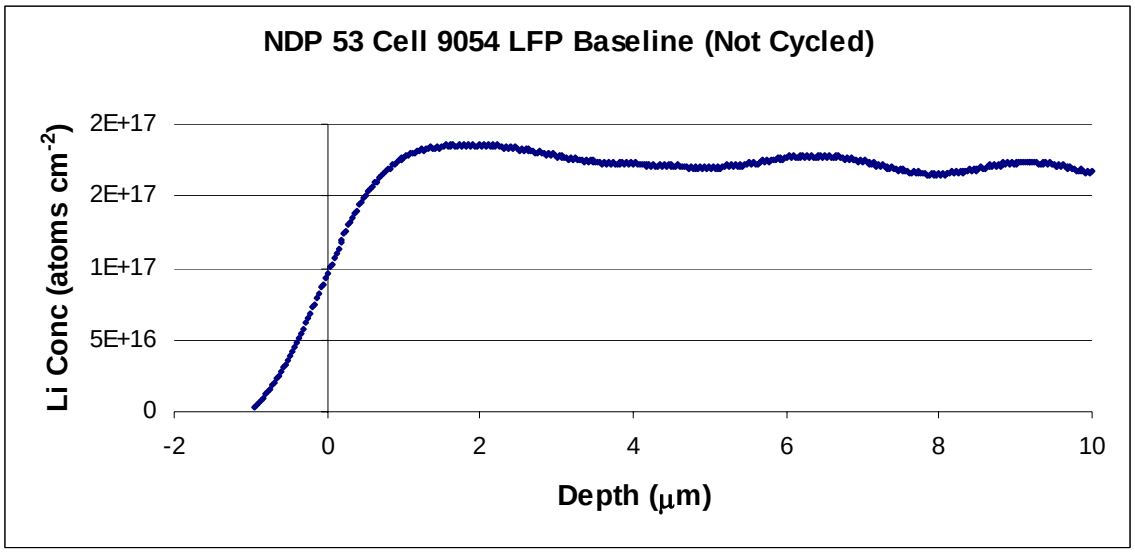

Figure 6.17: The baseline profile for the LFP cathodes shows that the lithium distribution is uniform throughout the cathode for the first 10 μm. The depth resolution of this profile is less resolved than that of the LNMCO cathodes due to the detector used.

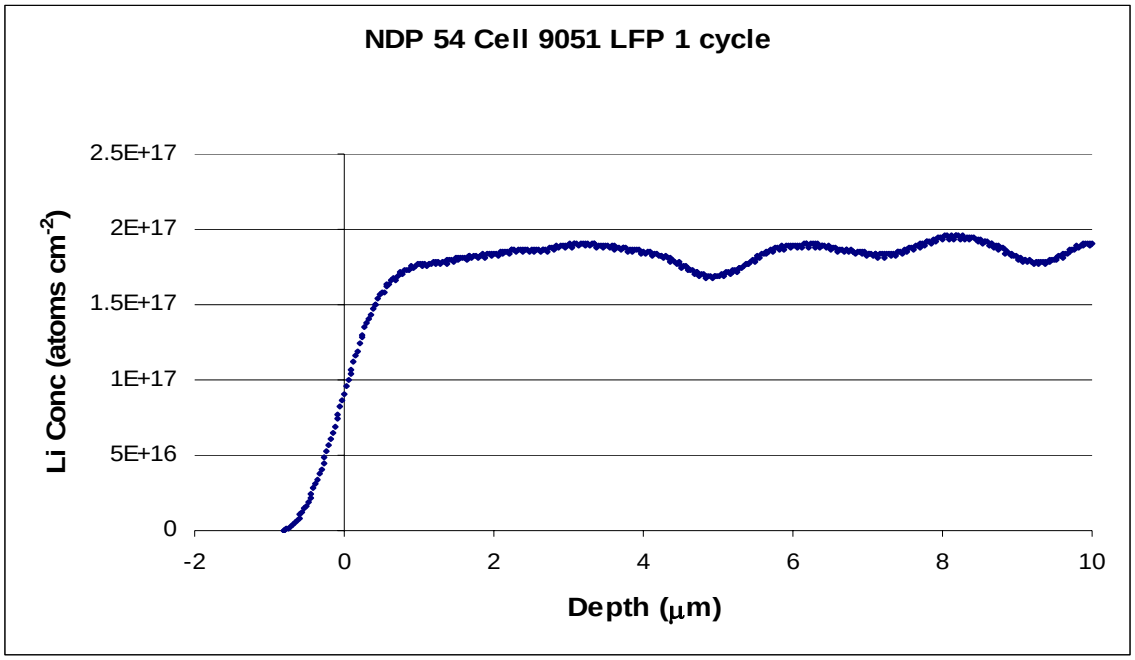

Figure 6.18: Profile of the LFP cathode after 1 cycle. Little difference is seen to occur in the lithium concentration distribution.

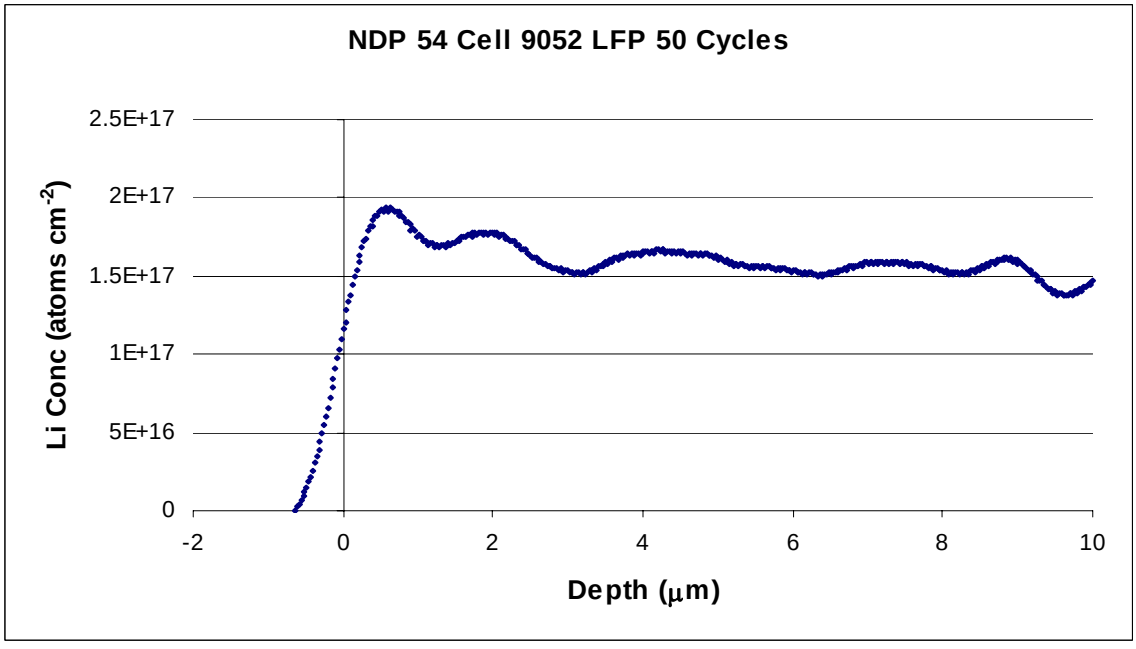

Figure 6.19: The profile of the LCP cathode cycled 50 times shows small lithium concentration fluctuations. The fluctuations are similar to those seen in the profile of the LNMCO cathode that was also cycled 50 times.

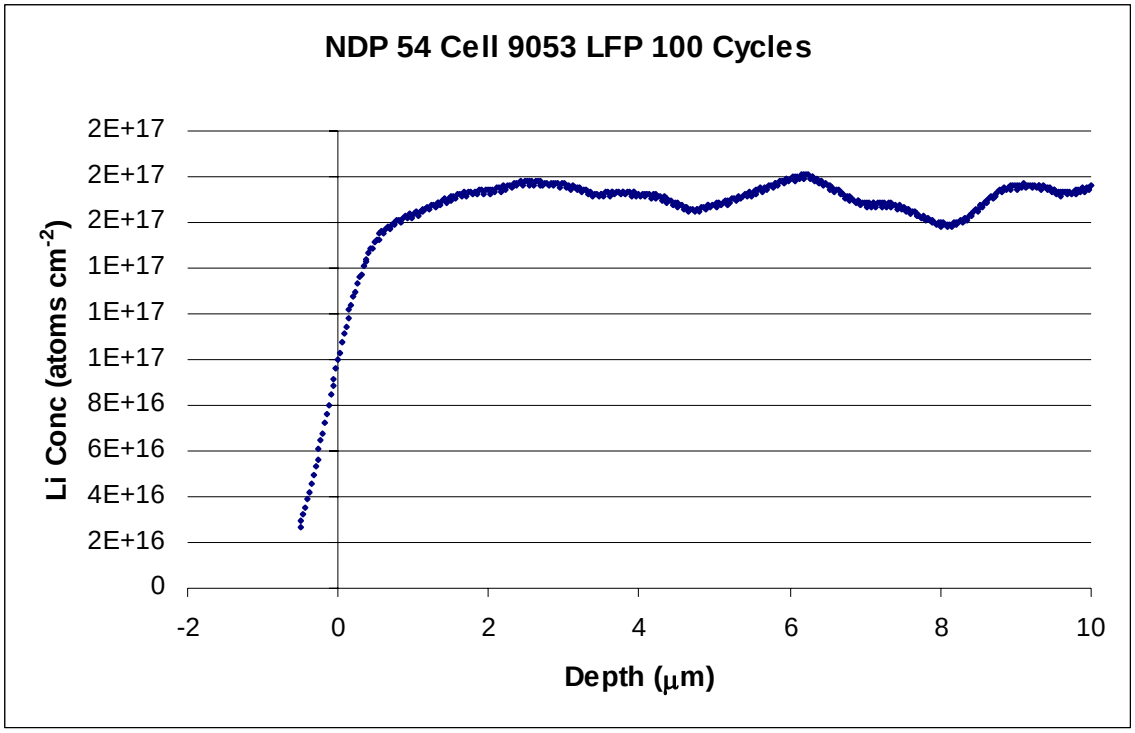

Figure 6.20: The profile of the LFP cathode after 100 cycles shows some fluctuation in the lithium concentration, but no drastic concentrating of the lithium near the surface is seen to occur.

Visual inspection of the profiles shows an increasing fluctuation in the lithium concentration as was also seen with the $LiNi_{1/3}Mn_{1/3}Co_{1/3}O_2$ cathodes. This lends credibility to the possibility that the lithium concentration fluctuations are the result of structural changes in the cathode due to cycling. Although these fluctuations are seen, there is no significant plating of lithium near the surface of the electrode as a function of cycling. The lithium distribution is uniform across the cathode as expected. Figure 6.21 shows the ratio of lithium within the first 2 μm to the value of all lithium in the 10 μm profiled depth.

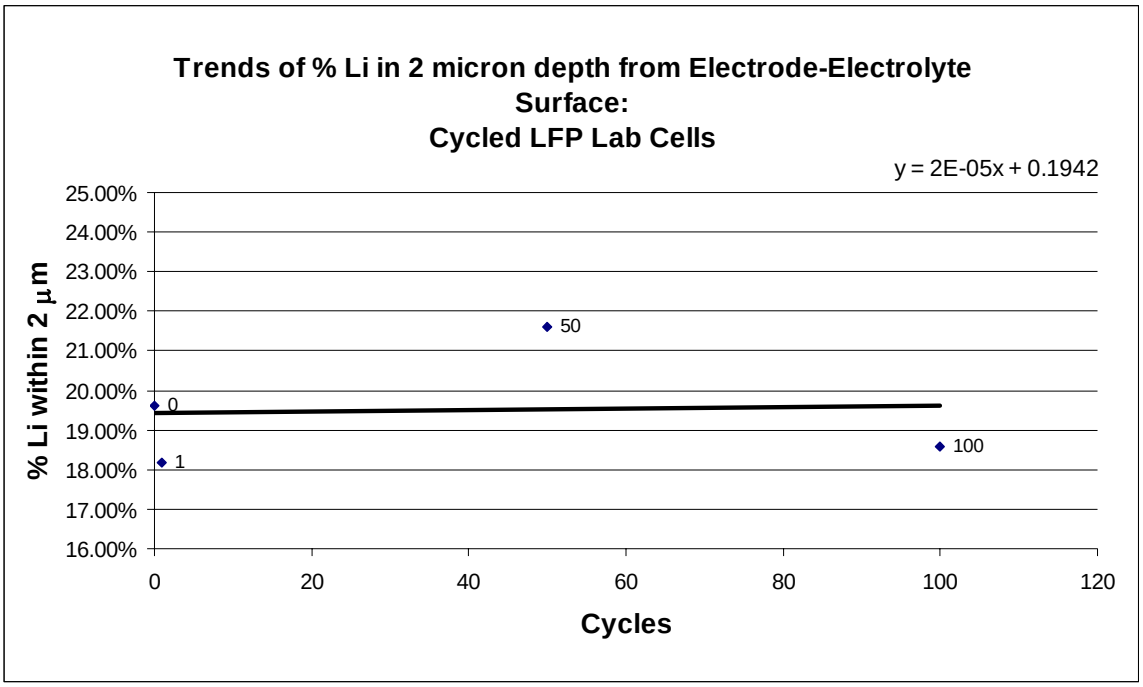

Figure 6.21: The data shows no positive slope, indicating that the lithium concentration in the LFP cathodes is not increasing near the surface.

All of the $LiFePO_4$ cathode profiles agree with the hypothesis that 20% of the lithium concentration in the first 10 µm would be present in the 2 µm near the electrode-electrolyte surface. The percentages of lithium within the first 2 µm for the $LiFePO_4$ are all approximately 20%. The maximum deviation from the 20% value was from the cathode cycled 1 time. This cathode deviated from the hypothesis by 1.82%.

Conclusions

Profiles of the $LiFePO_4$ and $LiNi_{1/3}Mn_{1/3}Co_{1/3}O_2$ cathodes after cycling show no sign of lithium concentrating near the electrode-electrolyte surface. Both plots of lithium

percentage vs. cycle number show no significant slope. This indicates that cycling is not a cause of lithium concentrating near the electrode-electrolyte surface.

This research has verified the initial hypothesis that lithium concentration near the surface does not occur as a result of cell cycling, and that the lithium distribution remains uniform throughout the cathode. All of the profiles of both cathode types show that the values of percentage of lithium within the first 2 μm of the profiled 10 μm depths were approximately 20%. This was the expected value from the hypothesis.

The increased fluctuation in lithium concentrations as the number of cycles increased was seen in both types of cathodes. This suggests that the fluctuations were not a symptom of mixing during the preparation of the cathode films. Instead it is more likely that structural changes within the cathode material do occur as a result of cycling and lead to the concentration fluctuations seen within the profiles. Further experimentation would be needed to determine the degree to which the fluctuations would change and to what extent these fluctuations may affect the performance of the cell.

While the data did not lead to any significant changes in lithium concentrations that may be a symptom of capacity fade, the agreement of the data with the hypothesis is further validation of NDP's application towards this type of research. The data lends credibility to any other significant findings by NDP towards this field in the future.

CHARGE/DISCHARGE RATE AND STATE OF CHARGE

It is well documented that the charge/discharge rate of a lithium ion cell can deteriorate the cell's performance [29, 41, 57-59]. Charging at higher rates has been determined to diminish the capacity of some cathode types by more than 18%. The rate that a cell is charged at is quoted in terms of *C* as follows in equation 6.1.

$$C = \frac{I}{Q_n} = \frac{\text{current}}{\text{nominal capacity}} \tag{6.1}$$

Therefore a cell discharged at a rate of τ will take $1/\tau$ hours to fully discharge. The lower the rate of discharge, the less degradation in cell performance is seen. To prevent harm to the battery, lithium ion cells are often charged/discharged at rates <1C. However, new high power applications such as hybrid electric vehicles (HEV) require cells that can be discharged at higher rates, between 1C and 5C, without having significant capacity fade.

Previous cathode types such as the $Li(Ni_{0.8}Co_{0.2})O_2$ have been developed in hopes of being used for high power applications. These cathodes were found to be unsatisfactory due to an impedance increase during the charging process of the cell. The impedance increase was caused by a phase segregation at the surface of the cathode and the development of a resistive $Li_xNi_{1-x}O$ film at the cathode surface [60]. The film is a result of the unstable tetravalent Ni^{4+} being reduced during the charging process.

To help mitigate the formation of the film on the cathode, the amount of Ni in the cathode is being decreased and the $LiNi_{1/3}Mn_{1/3}Co_{1/3}O_2$ is now being researched for high power applications. It is expected that the reduction in Ni and the stabilization of the crystal structure by the Mn^{4+} cations should prevent the phase segregation.

Prior research has shown that this cathode type can provide the necessary power requirements for HEV applications, but research into the cell's performance under

temperature, cycling, and charging conditions is still being performed. The research performed for this report has charged/discharged the $LiNi_{1/3}Mn_{1/3}Co_{1/3}O_2$ at various rates and profiled the cathodes in different states of charge to determine the following:

- Is a film containing Li present at the surface of the cathode?
- Is the Li distribution uniform throughout the cathode as expected?
- Are concentration fluctuations present that could indicate structural changes as a result of discharge rate?

Experiment

$LiNi_{1/3}Mn_{1/3}Co_{1/3}O_2$ cathodes were made in the lab and incorporated into coin cells with lithium anodes. The cells were charged/discharged at rates of 0.1C, 1C, 2C, and 4C to simulate the conditions that a cell might face under normal conditions as well as conditions that require increasingly higher power. Charging /discharging the cells at a rate of 0.1C took a total of 20 hours. The same cycle for 1C took 2 hours, 1 hour for 2C, and 30 minutes for the 4C rate.

In addition to the variation in rates, cells were also left in different states of charge (SOC) before disassembly. For each charging rate, one cell was disassembled in a discharged state, while another was disassembled in a charged state. This was done since the previous problems seen in the $Li(Ni_{0.8}Co_{0.2})O_2$ cathodes were due to a film formation during the charging process.

The cells were charged/discharged by a high precision current on an Arbin battery cycler. During each cycle, the cell's charge and discharge capacity, charge and discharge energy, maximum voltage, and current were monitored such that any significant findings could be matched to any obvious fluctuations during the conditioning of the cell.

After conditioning, the cells were disassembled according to the previously described procedure. The cathodes were removed and then profiled with NDP.

Results

The cathodes were profiled and analyzed in the same manner as previously discussed in the "Cell Cycling" section. Analysis was performed to determine if the lithium concentration was uniform and if any noticeable film containing lithium was formed at the electrode-electrolyte surface. The depth profiles for the cathodes are shown in figures 6.22 through 6.30. The title of each profile shows the rate it was charged/discharged at as well as the state of charge (SOC), where "C" means charged and "D" means discharged.

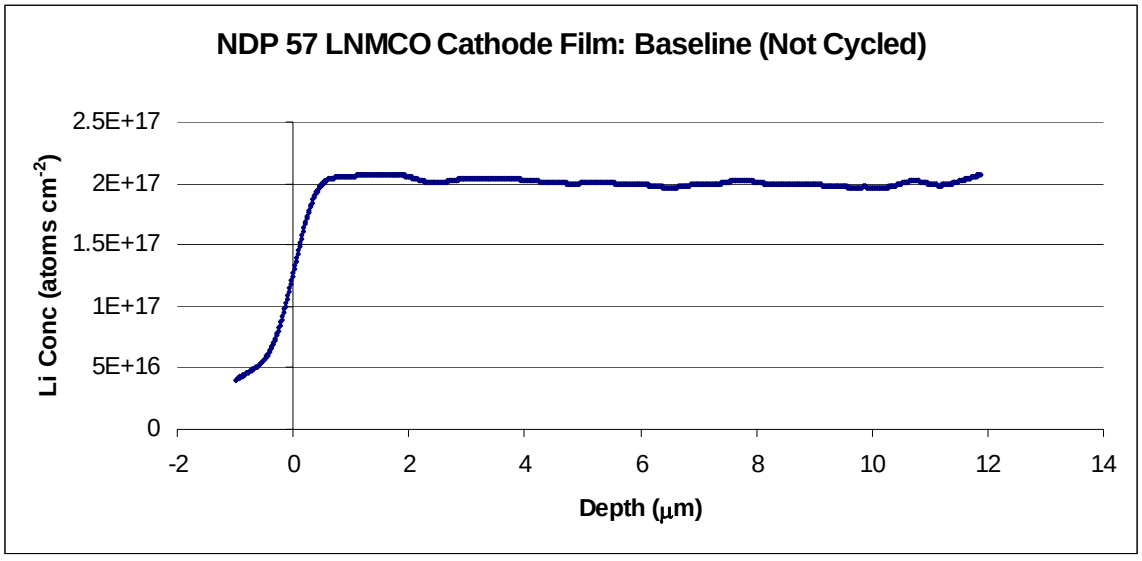

Figure 6.22: The baseline sample for the other profiles. This LNMCO cathode was never incorporated into a cell.

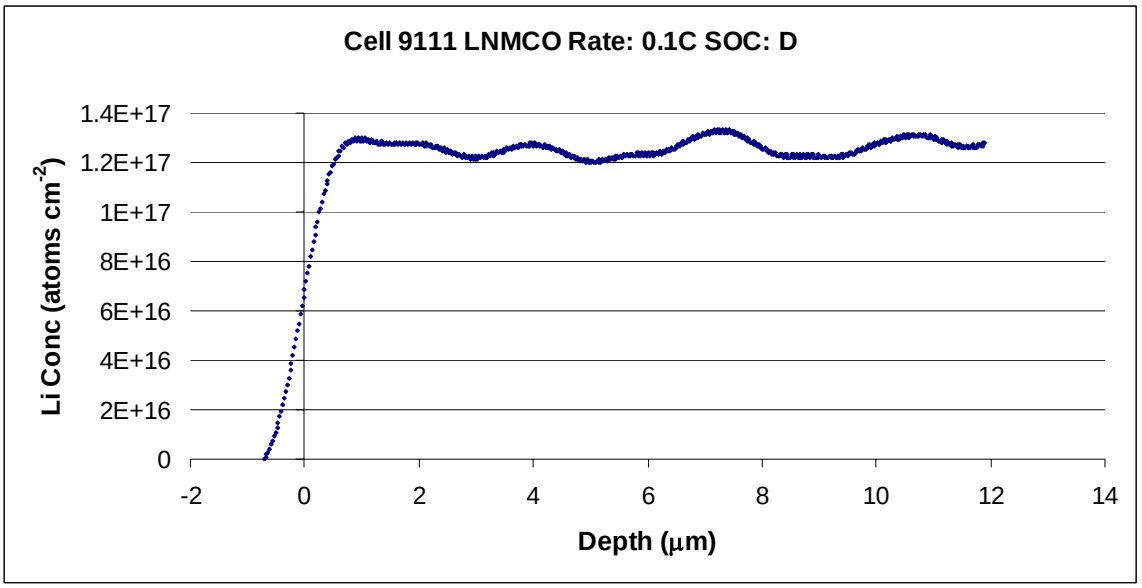

Figure 6.23: Depth profile of the LNMCO cathode charged/discharged at a rate of 0.1C.

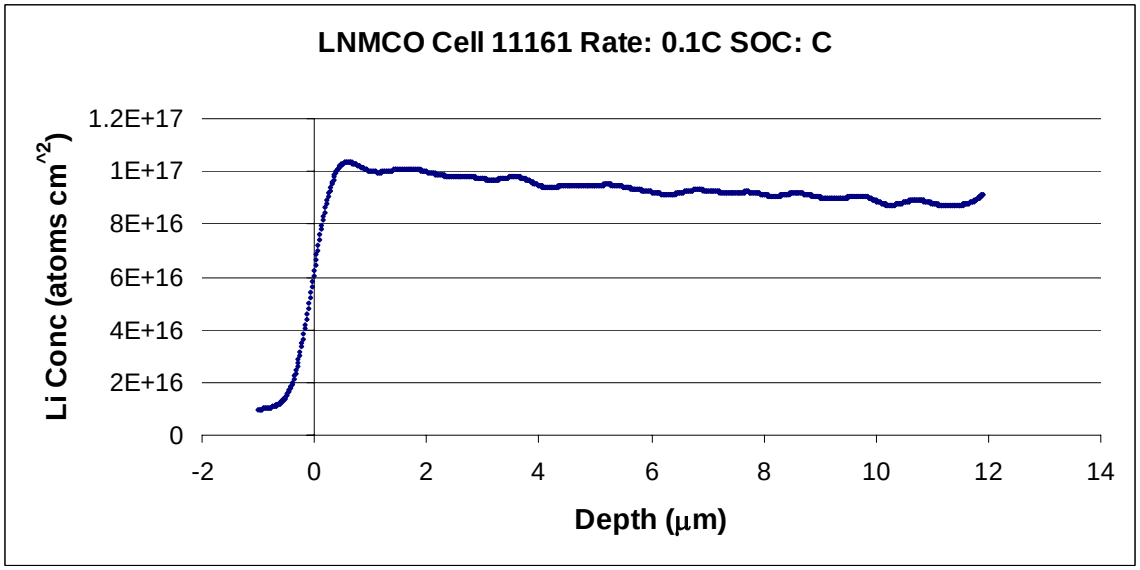

Figure 6.24: Depth profile of the LNMCO cathode charged at a rate of 0.1C. The charged profiles contain a slight slope to the lithium distribution as depth increases.

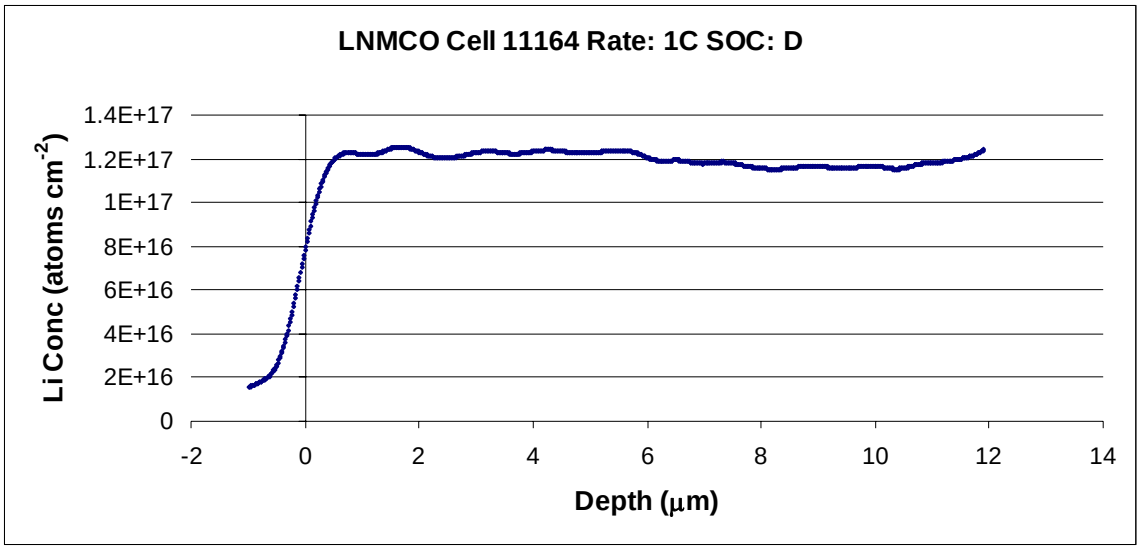

Figure 6.25: Depth profile of a LNMCO cathode charged/ discharged at a rate of 1C.

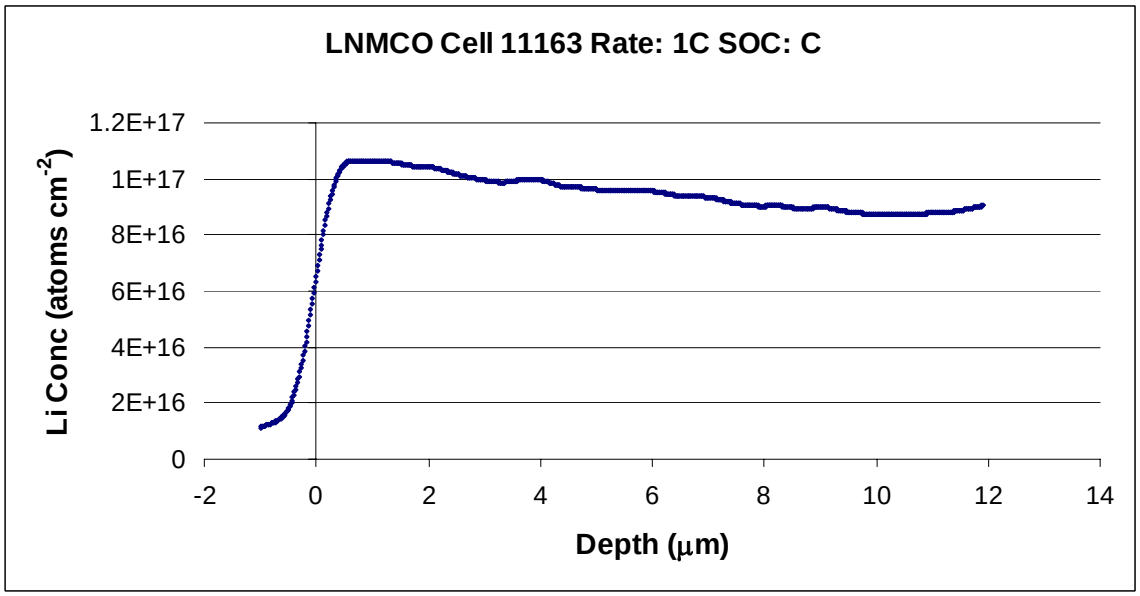

Figure 6.26: Depth profile of a LNMCO cathode charged at a rate of 1C. The slope in the lithium concentration has increased from that of the 0.1C charged cathode.

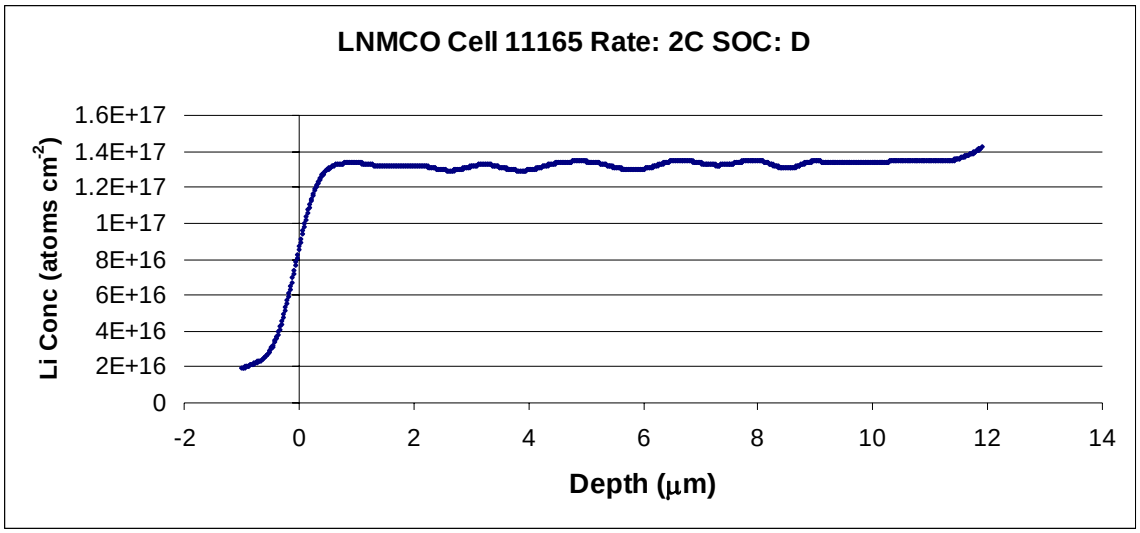

Figure 6.27: Depth profile of a LNMCO cathode charged/discharge at a rate of 2C. There is a uniform lithium concentration with relatively no slope in relation to depth.

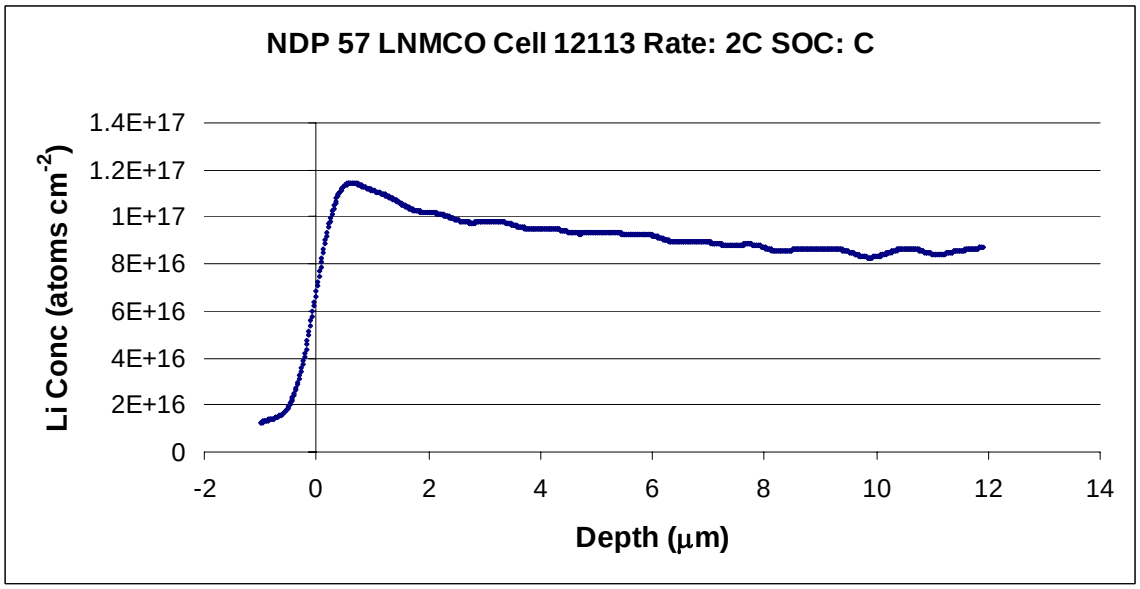

Figure 6.28: Depth profile of a LNMCO cathode charged at a rate of 2C. The slope in the lithium concentration as depth increases has increased from the 1C rate cathode.

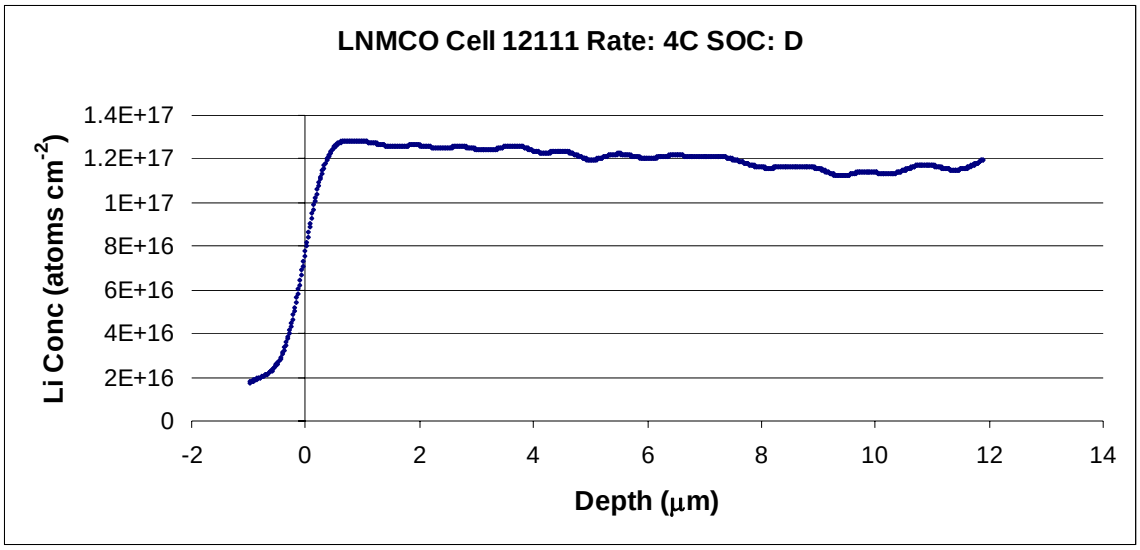

Figure 6.29: Depth profile of a LNMCO cathode charged/ discharged at a rate of 4C. This rate is at the far end of those typically required for high power applications.

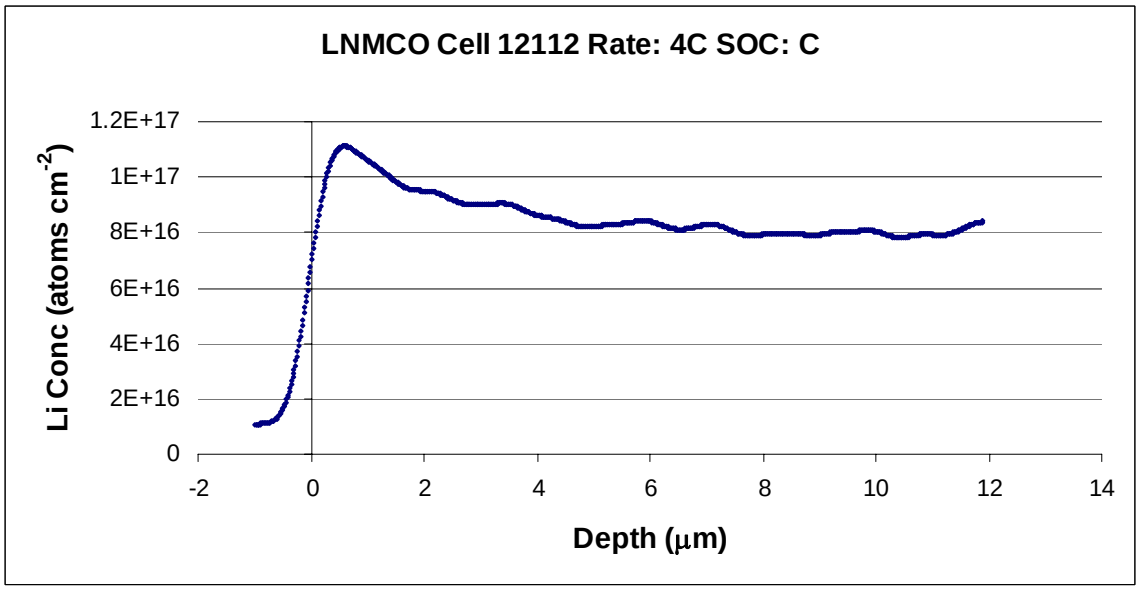

Figure 6.30: Depth profile of a LNMCO cathode charged at a rate of 4C. This lithium concentration is clearly no longer uniform within the first 10 μm of the cathode. The difference between the charged cathode and the discharged cathode distribution is significant.

The depth profiles indicate a clear tendency for lithium to concentrate near the electrode-electrolyte surface upon charging. The discharged cells show uniform lithium concentration distribution within the first 10 μm from the cathode surface. From visual inspection, it appears that the extent to which this effect occurs increases with the increasing charge/discharge rate of the system. Comparing the data shows that this trend is present as shown in figure 6.31.

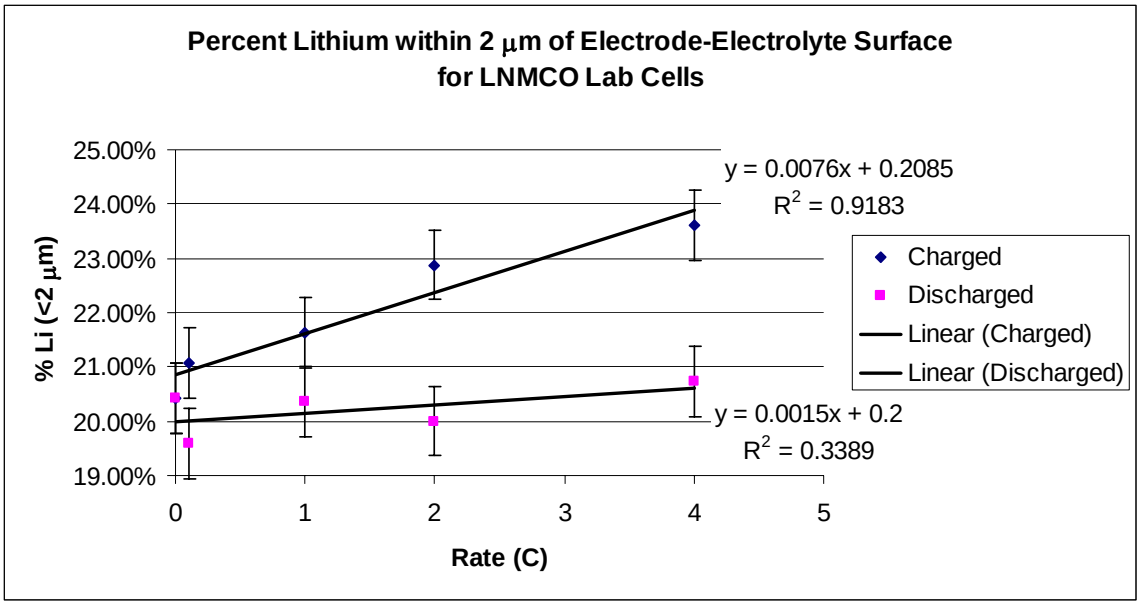

Figure 6.31: Trends indicate that the charge rate affects the degree to which lithium will concentrate near the electrode-electrolyte surface.

The discharged cathodes each have percentage of lithium concentration values within the first 2 μm of ~20% as should occur with a uniform distribution across 10 μm. The charged cathodes deviate from this expectation. The trendlines clearly show that the higher the charging rate, the more lithium there is concentrated within the first 2 μm of the electrode-electrolyte surface on the cathode. The slope of the charged cathode trendline is 0.0076, indicating that the effect shown will increase with increasing rate.

The difference in slope between the charged and uncharged ratios is outside of the error, indicating that the trends are real.

The increasing lithium concentration is likely due to the higher concentration of Li^+ ions moving out of the electrode-electrolyte surface during charging of the cell. Once the charge was completed those lithium ions no longer experienced a voltage to move them towards the anode. However, the assumption is that the Li^+ ions should then uniformly disperse throughout the cathode due to electrostatic repulsion. This is the same hypothesis that was proven to be true for cycled cells in a previous section of this report.

The profiles measured were done so after the cell had been in the charged state for several days; therefore it is not likely that the lithium did not have enough time for diffusion. The more likely explanation is that the diffusion gradient was not sufficient to overcome the activation energy to cause the Li^+ ions to diffuse.

Two of the three questions that were posed at the beginning of this section have been answered.

1. The lithium concentration does remain uniform throughout the first 10 μm of the discharged cathodes. The concentration is not uniform in the charged cathodes and this trend is enhanced with increasing charging rate.
2. There are no significant concentration fluctuations such as those seen in the cycled cells that may indicated structural changes occurring throughout the cathode.

The answer to the remaining question as to whether a film containing lithium is present on the cathode surface was determined by correcting the spectra for energy broadening. Performing a correction for energy broadening will provide a better idea of the Li^+ distribution at the surface. Figures 6.32 and 6.33 show the corrected spectra for the two extreme cases of 0.1C charged, and 4C charged cathodes.

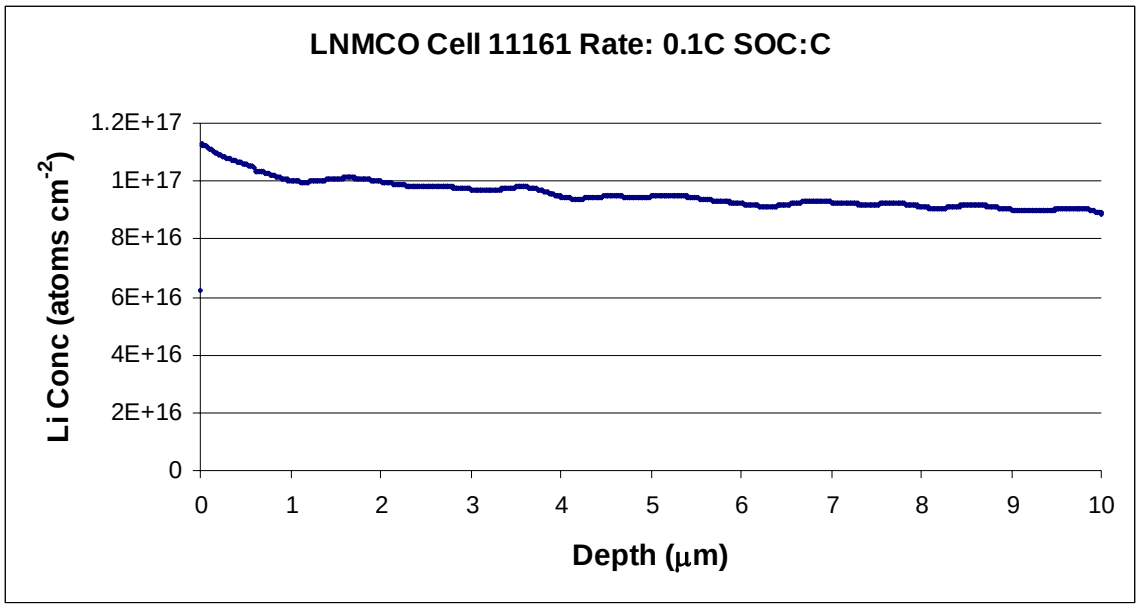

Figure 6.32: Energy broadening corrected depth profile of LNMCO cathode charged at 0.1C.

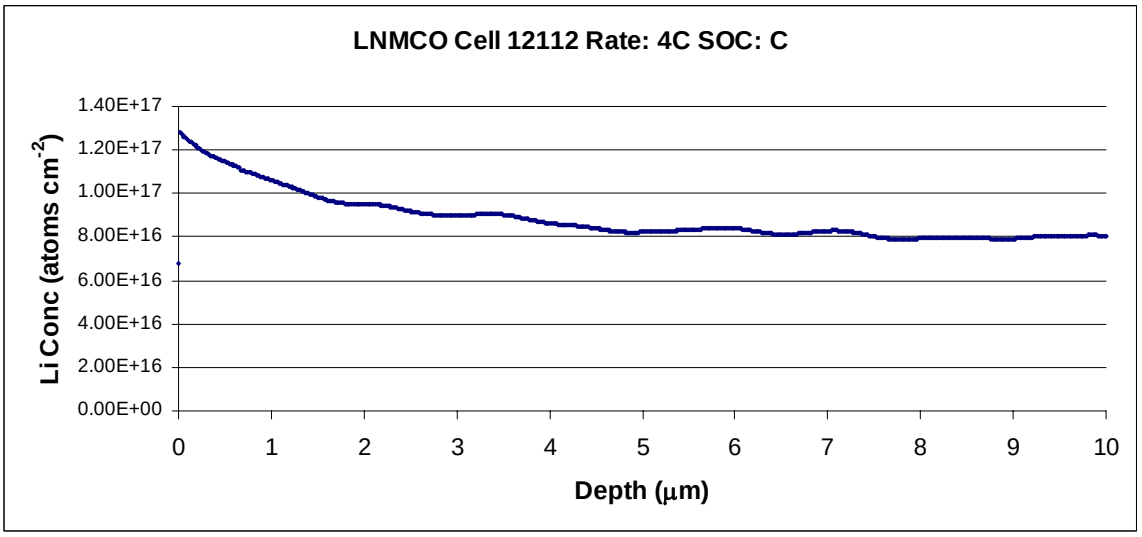

Figure 6.33: Energy broadening corrected depth profile of LNMCO cathode charged at 4C.

Figure 6.33 shows that there is an increased lithium concentration at the surface relative to the rest of the cathode. The increase in this concentration from the 0.1C cell to the 4C cell appears to be a result of large amounts of Li^+ ions moving towards the anode, not of film formation. Analyses of the alpha profiles of the above cathodes also show no signs of a thin film at the surface.

Therefore, the results of this profile agree with the initial hypothesis that no film is formed on the electrode-electrolyte surface of the cathode. While there is increased lithium concentration near the surface, this increase follows the trend specified by the slope in figure 6.31. So it is presumably a result of Li^+ migration towards the anode, and not of film formation. It is likely that reducing the amount of Ni^{4+} helped to prevent the film seen in the $Li(Ni_{0.8}Co_{0.2})O_2$ cathode.

Conclusion

Profiling of the cathodes answered the three questions posed at the beginning of this section.

1. Is a film containing Li present at the surface of the cathode?

   No noticeable film containing lithium was determined by NDP to be present on the electrode-electrolyte surface of the cathode. This was in agreement with the hypothesis. The results validate the expectation that the Mn^{4+} cations act to stabilize the $LiNi_{1/3}Mn_{1/3}Co_{1/3}O_2$ crystal structure and prevent phase segregation. No other profiling techniques have determined physical descriptions of the lithium distribution throughout these cathodes to validate the absence of the film.

2. Is the Li distribution uniform throughout the cathode as expected?

   The lithium distribution was uniform throughout the discharged electrodes. Each percentage value of lithium concentration within the first 2 μm was ~20% as

predicted. The lithium distribution was not uniform for the charged cathodes as lithium was found to concentrate near the surface. This effect increased with charging rate and the maximum measured value was 23.6% of the lithium within the first 2 μm. This occurred in the 4C charged cell.

The presence of lithium concentrating near the surface of the cathode was not in agreement with the hypothesis. This type of measurement opens doors for the possibility of NDP to become useful as a technique for the measurement of diffusion coefficients in these electrode materials. Further research will be required to see if the lithium concentration build-up that is occurring as a result of charge state and rate affects the cell performance and if it is "remembered" by the cathode, or if the lithium distribution will return to normal with another discharge of the cell.

When asked this question, John Goodenough Ph.D. believed that the cathode would not remember the effect. Goodenough's opinion was that the lithium distribution would return to a uniform distribution upon discharge of the cell. What has not been answered is if the effect measured is a sign of mass-transfer issues, and if this effect would eventually reach a point in which the structure of the cathode would be irreparably damaged. If so then this might help to indicate a limit of high power applications for the $LiNi_{1/3}Mn_{1/3}Co_{1/3}O_2$ cathode.

3. Are concentration fluctuations present that could indicate structural changes as a result of discharge rate?

There were no significant concentration fluctuations seen to occur throughout the cathode profiled depth as was seen in the cycled cells.

Chapter 7: Conclusions and Recommendations

Every objective accomplished by this research helped to supplement the credibility and utility of the NDP technique to the field of electrochemical research. Additionally, the UT-NDP facility was also legitimized through various benchmarking techniques. Ultimately, the research of this report accomplished the objectives set during the proposal. The objectives accomplished were as follows:

1. Validate the credibility of depth profiles measured with The University of Texas Neutron Depth Profiling facility by benchmarking results against: the NIST NDP facility, SIMS, and MCNPX models.
2. Perform a feasibility study on the ability of NDP to accurately profile the lithium distribution in electrode materials that have been removed from a battery operated under various conditions.
3. Develop a methodology for the separation, preparation, and handling of electrode materials from commercial and lab made lithium ion cells.
4. Analyze significant areas of lithium ion cell research to which NDP may be applied and profile various electrode samples to test existing hypotheses about Li^+ behavior in lithium ion cells. This includes:
    i. Interfacial analysis and profiling of lithium passivation layers formed on graphite anodes.
    ii. Analysis of lithium behavior in cathode materials to determine any contrast associated with charge/discharge rate, composition, cell cycling, or state of charge.

FEASIBILITY AND APPLICATION OF NDP TO ELECTRODE RESEARCH

This research has not only validated the profiling of electrodes by NDP, but has also validated the profiling of electrodes with the UT-NDP facility. The beginning of this research was focused on benchmarking the UT-NDP facility against other techniques and facilities such as the SIMS technique, and the NIST-NDP facility. Both benchmarks concluded that the UT-NDP facility was producing accurate profiles.

Comparison of depth profiles from the UT and NIST NDP systems showed that the two agreed in terms of shape, concentration, and depth measurements. The concentration differences in the NDP profiles between the NIST and UT systems were less than 2% at shallow depths in both samples and the peak concentrations shared a difference of only 0.23% in the best case. It was also shown that these differences can be substantially decreased with increased counting times. The differences were well within the allowed error for concentration, and so ultimately we can conclude that the systems determined the same concentrations.

Depth comparisons between the NIST and UT profiles were analyzed by comparing depth measurements of inflection points in the profiles. The differences between depth measurements of the two systems at the inflection point were only 83 and 77 nm. This value is well within the 444 nm and 463 nm depth resolution of the triton particle being measured. Accordingly, one can conclude that the depth measurements of both facilities agreed well with one another.

Analysis of NDP depth profiles from the UT facility compared to those determined by a SIMS facility showed that the profiles were in agreement. The comparison of these techniques was advantageous to explore the limitations of each technique including depth determination and energy broadening effects. However, the ultimate conclusion was that each technique determined profiles with similar shape distributions. Due to the lack of sputtering rate for the SIMS technique, complete

numerical comparison of concentrations at depths was not feasible, but the similarities in distributions were enough to see that both techniques had similar measurements.

Each of the previous experimental benchmarking methods was performed with a graphite anode and an oxide cathode that had been conditioned inside of an operating cell. Using these samples for benchmarking, all of the systems determined similar profiles for the electrodes. It is unlikely that all three systems, and two different techniques, would be inaccurate in similar fashions. Subsequently, one can conclude that NDP is a very capable technique for determining depth profiles of operated electrodes, and that the UT-NDP facility determined profiles within error to that of the NIST-NDP facility. Additionally, NDP has the ability to profile the electrodes without the risk of false information from fast ion migration, which is a limitation of the SIMS technique. Therefore one can be more confident in the results of an NDP measurement for this sample type than that of a SIMS measurement.

The SIMS technique is the most competitive to NDP in terms of maximum depth profiling capability, resolution, and the type of information gained. Other techniques that may be useful in this arena include focused ion beam (FIB), X-ray photoelectron spectroscopy (XPS), and elastic recoil detection (ERD) among some others. None of these techniques share the full capability of NDP towards electrode research. SIMS is limited by the threat of fast ion migration, ERD can cause deterioration of the surface and consequently limited depth resolution [10], and XPS technique has been found to not be sensitive enough to the lithium for accurate characterization. Additionally, NDP is non-destructive and is capable of analyzing the sample without significantly disturbing it. Therefore, not only is NDP a better technique for this type of surface profiling, but also there is no disadvantage towards the application of NDP in electrode research. It does not suffer from the listed limitations, and more importantly, it can be used in addition to other techniques for the same sample.

LITHIUM ION ELECTRODE RESEARCH

New insights into lithium ion cell electrodes have been revealed through this research. Though a vast literature search was performed, no other literature known to the author has clearly shown a relative concentration vs. depth profile of interfacial layers in operated lithium ion electrodes as this research has done. We have also shown that the initial assumptions of uniform concentration distributions throughout the electrodes were also not definitively true. In fact, that assumption is only correct for discharged cells, but charged cells do not follow this "rule". These results are but a few of the many that NDP can be used to determine in this area of research.

Each objective of this study looked at only a small portion of lithium ion cell research in hopes of analyzing where NDP may be more useful. Analysis was performed on the application of NDP to electrode research in areas such as interfacial studies including passivation layers, and the variation in lithium distribution according to cell cycling, charge/discharge rate, and state of charge. What was determined was that the reaches of NDP should be further extended in both areas, but particularly into the research of SEI layers on anode samples.

The use of NDP to research SEI layers on $LiFePO_4$ and $LiFePSO_4$ cell anodes was found to be a success and showed trends similar to that of previous work. The difference was that this report's results were accomplished with only one technique, as opposed to the two used by the previous research. The use of only one technique limits the opportunity for incorporation of error. NDP was also able to provide a relative concentration vs. depth profile that the other study did not. This research also analyzed cells that did not include the threat of other anode plating mechanisms that may disturb the profiling results.

Additionally, NDP was used to test the effect of cell cycling on the lithium distribution within $LiFePO_4$ and $LiNi_{1/3}Mn_{1/3}Co_{1/3}O_2$ cathodes. Ultimately this was a search for any Li^+ mobility issues or the signs of passivation layer changes. Profiles of the

$LiFePO_4$ and $LiNi_{1/3}Mn_{1/3}Co_{1/3}O_2$ cathodes after cycling show no sign of lithium concentrating near the electrode-electrolyte surface. This indicates that cycling is not a cause of lithium concentrating near the electrode-electrolyte surface. The findings of this research for this application agreed with the initial hypothesis that the concentration would be distributed uniformly throughout the electrode. The research verified that lithium concentration near the surface does not occur as a result of cell cycling, and that the lithium distribution remains uniform throughout the cathode. All of the profiles of both cathode types show that the values of percentage of lithium within the first 2 μm of the profiled 10 μm depths were approximately 20%. This was the expected value from the hypothesis.

Profiling of $LiNi_{1/3}Mn_{1/3}Co_{1/3}O_2$ cathodes that were charged/discharged at different current rates provided interesting insight into the lithium behavior for cells in different states of charge. NDP of cathodes from charged cells found that lithium does concentrate near the electrode-electrolyte surface, contrary to the hypothesis. The amount of lithium concentration is increased along with the rate of charge. It is known that charging at higher rates can lead to capacity fade, but further research will be needed to correlate the lithium concentration directly to capacity fade. However, this is another area of lithium ion cell research that NDP has proven to be a valuable asset.

RECOMMENDATIONS FOR FUTURE WORK

The most valuable area of lithium ion research that NDP can be a real asset to is the research into SEI variation. This research is not only limited to SEI variation with temperature, but rather a large amount of research is being performed on SEI variation according to cathode composition, electrolyte composition, and also on the formation processes of the SEI. The SEI is a necessary component of any lithium ion cell, however

the electrolyte components can drastically affect both the stability of the SEI as well as the cell's performance. NDP's ability to provide depth profiles will prove invaluable to those investigating the SEI behavior and its relation to the cell's performance.

Appendix A: MCNPX Deck

MCNPX deck

```
1-      Neutron Depth Profiling- Created by Scott Whitney 01/24/08.
2-      c Modified from Dustin Reinert's Code
3-      c Silicon Surface Barrier detector
4-         3     14  -2.33     -14 15 -3
5-      c Sample
6-         7     6   -2.46     -18
7-      C Chamber
8-         4     5   -2.7      -17 16
9-      c World inside chamber
10-        5     2   -1e-8     -20 #3 #4 #7
11-     c Cookie Cutter
12-        8     0           -1     $ Cookie Cutter
13-     c Outside world with no importance
14-        6     0           20
15-
16-     c Source
17-     C    1        py       -2.0  $ surface for origin of neutrons
18-        1       RCC      0 -4.0 0  0 3.0 0 3.0  $ Origin for neutron source
19-     C Detector
20-        3        cy       0.39  $ Silicon Surface barrier outer radius
21-        14       py       7.01  $ back of silicon
22-        15       py       7.00  $ front of silicon
23-     c Sample
24-        18       RCC      0 -0.0001 0  0 0.0002 0 0.5  $ Wafer that is 2 microns
25-     C Al chamber
26-        16       RCC      0 0 -38.1  0 0 72.1  15  $ 72.1 cm tall cylinder r=15
27-        17       RCC      0 0 -39.1  0 0 74.1  15.5 $ outside of cylinder
28-     c World
29-        20       so       200   $ world
30-
31-     MODE N H D T S A
32-     m14   14000.              1 $ Silicon
33-     m6    5010.00c             1 $ Boron
34-     m5    13000.             1 $ Aluminum
35-     m2    7000.            0.7 $Air
36-           8000.            0.3
37-     IMP:N,H,D,T,S,A 1 1 1 1 1 0
38-     C sdef ERG=2.5e-8 POS=0 -2.0 0 PAR=N
39-        SDEF  ERG=2.5e-8  VEC=0  1  0  NRM=+1  X=0  Y=-3.5  Z=0  CCC=8
DIR=1 RAD=D1 PAR=N
40-     si1 0 2
41-     sp1 0 1
42-     PHYS:N   100 0 0 -1 -1 0 1    $ allows light-ion recoil
```

```
 43-       PHYS:H   100 0 -1 J 0 J 1     $ allows light-ion recoil
 44-       PHYS:A   100 J J J 0
 45-       CUT:A    J 1e-6 J J           $ set lower energy limit for alpha
warning.  alpha       ecf raised to ecut_min(34) = 1.0000E-03
 46-       CUT:T    J 1e-6 J J           $ set lower energy limit for Triton
warning.  triton      ecf raised to ecut_min(32) = 1.0000E-03
 47-       CUT:H    J 1e-6 J J           $ set lower energy limit for proton
warning.  proton      ecf raised to ecut_min( 9) = 1.0000E-03
 51-       F122:A 15 T
 52-       F222:n 15 T
 53-       F8:A 3
 54-       FT8 GEB 0.030 0 0
 55-       E8 0 1e-6 1022I 3.0
 56-       E2 1e-6 1022I 3.0   $ Energy Binning
 57-       NPS 8.7e9
```

Appendix B: UT-NDP Experimental Facility and Spectral Analysis Operations Manual

1. **Sample Preparation**
    a. Select sample sizes that may easily fit onto aluminum mount plates.
    b. Each plate has a scored mark near the center that indicates where the center of the sample should be placed to be directly in the beam.
    c. Select an aperture size (this will determine the area of the sample analyzed), and use a punch to cut the aperture into a Teflon mask.
    d. Place the sample over the scored mark on the aluminum mount, then place the Teflon mask with the aperture over the sample. The mask can be secured with double-sided tape between the Teflon and the aluminum.
2. **Sample Mounting and Facility Set-up**
    a. The circular aluminum mount with 8 circles around the perimeter is the mounting plate. Each circle on the mounting plate has a numbered outline around it which tells which aluminum sample mount belongs to which circle, and also selects how the mount is positioned over the circle.
    b. Latch the aluminum sample mounts into their correct positions on the mounting plate. Ensure that each is securely mounted and does not move.
    c. Place sample mount onto rotary motor so that samples are aligned with neutron beam line. This is most easily performed with a laser level.
    d. Check motion of sample mount automated rotation to ensure that sample position coordinates are known. Move sample mount to align calibration standard with neutron beam.
    e. Select angle between the neutron beam and normal to the sample mount.
    f. Select angle between detector normal and sample normal.
    g. Select distance from sample to detector. This is typically set to subtend a solid angle of 0.1%, approximately 7 cm from sample with a 50 mm^2 detector.
    h. Close target chamber and align the small markings on the bottom of the chamber lid and top of chamber base just over the turbopump bellows. If this

is not aligned, you will experience high low energy background. Also, ensure that viewing window and ion gauge and covered to prevent light from entering the chamber.

i. Turn on Leybold Trivac roughing pump to pump the target chamber to a pressure of approximately 10 x 10^{-3} torr. This pressure should be monitored with the 275 Granville-Phillips Convection gauge controller. This will take ~6 hours.

j. Turn on Turbotronik NT10 Turbopump and pump the system to 5 x 10^{-6} torr. Remember to turn on the fan on the bottom of the turbopump. This will take ~1 to 3 hours. The pressure is measured with the ion gauge and is controlled and monitored by a 307 Granville-Phillips Vacuum Gauge controller.

3. Facility Operation

a. Open manual lead shutter, then flip switch to open mechanical neutron shutter. At this point the beam port area cannot be entered.

b. Check vacuum levels with ion gauge controller. If level is 5 x 10^{-6} torr then increase the bias voltage to the detector slowly to the desired voltage.

c. Monitor the pulse and detector noise with an oscilloscope in parallel.

d. Open the GENIE software, and open detector "Si".

e. Select acquisition characteristics on the Genie program.

f. Once reactor has achieved desired power, begin acquisition simultaneously while pressing start on the neutron counter.

g. Once the count is finished, save the spectrum.

h. The sample mount can be moved with the Velmex 90 Controller on the CPU.

i. Open the controller. Select "motor 1" for the X-axis. Select "steps" for the increment. Do not select any more motors. Bring controller online.

j. Select 1037 steps. Set movement at 200 steps per second. Press the positive arrow once to move 1037 steps to the next sample. The positive direction moves the sample mount number by +1.

4. Post Shutdown

a. After sample counting is completed and reactor is shutdown, close neutron and lead shutter.

b. Turn off bias voltage to detector.

c. Turn off turbopump and fan. Let this spin down for at least 1 hour.

d. Turn off roughing pump.

e. Open gas purge valve beneath NDP chamber.

f. Slowly open valve to gas tank outside of beam port 2 chamber. Watch the convection gauge controller to be sure pressure is not rising by more than 5 torr increments.

g. Close tank valve once convection gauge reaches 700 torr.

h. Close gas purge valve beneath chamber.

i. Open chamber lid with winch.

j. Remove samples and begin again.

5. **Spectrum Analysis**

a. Open SRIM 2006 program and select “Stopping range tables”.

b. Select sample composition and ion energies, then calculate stopping power data.

c. Fit this data to a function with Tablecurve 2D . This is *S(E)*.

d. Find a function for the integral of the inverse of *S(E).* We will call this the path length function, *x(E)*. It will be used after energy calibration.

e. Evaluate the spectra of the energy calibration standards used for each type of ion being analyzed.

f. Savitzky-Golay smooth the data and evaluate the first derivative of the smoothed function to determine energy calibration points. This process is better described in the dissertation.

g. Use the determined fractional channels to calibrate your spectra from this detector set-up.

h. Depth analysis is determine by using the path length function, *x(E)*, in conjunction with the calibrated energy spectrum.

i. Concentration analysis is performed by the comparator method with calibration standards. A more detailed description of this analysis is described in the spectrum analysis section of this dissertation.

References

1. Lamaze, G.P., et al., *In Situ Measurement of Lithium Movement in Thin Film Electrochromic Coatings Using Cold Neutron Depth Profiling.* Surface and Interface Analysis, 1999. **27**: p. 4.
2. Lamaze, G.P., et al., *Analysis of lithium transport in electrochromic multilayer films by neutron depth profiling.* Surface and Interface Analysis, 2000. **29**: p. 5.
3. Ning, G., B. Haran, and B. Popov, *Capcity fade study of lithium-ion batteries cycled at high discharge rates.* Journal of Power Sources, 2003. **117**: p. 10.
4. Yoshida, T., M. Takahashi, and S. Morikawa, *Degradation mechanism and life prediction of lithium-ion batteries.* Journal of the Electrochemical Society, 2006. **153**(3): p. 6.
5. Downing, R.G., G.P. Lamaze, and J.K. Langland, *Neutron Depth Profiling: Overview and Description of NIST Facilities.* J. Res. Natl. Inst. Stand. Technol., 1993. **98**: p. 109.
6. Ziegler, J.F., G.W. Cole, and J.E.E. Baglin, *Technique for determining concentration profiles of boron impurities in substrates.* Journal of Applied Physics, 1972. **43**(9): p. 3809-3815.
7. Muller, K., R. Henkelmann, and H. Boroffka, *The Determination of low dose boron implanted concentration profiles in silicon by the (n, alpha) reaction.* Nuclear instruments and Methods, 1975. **129**: p. 557-559.

8. Biersack, J.P., et al., *The use of neutron induced reactions for light element profiling and lattice localization.* Nuclear instruments and Methods, 1978. **149**: p. 93-97.

9. Cervena, J., et al., *The use of the neutron induced reaction for boron profiling in Si.* Nuclear instruments and Methods, 1981. **188**: p. 185-189.

10. Krings, L.H.M., et al., *Lithium depth profiling in thin electrochromic WO3 films.* Journal of Vacuum Science Technology, 1998. **17**(1).

11. Arora, P. and R.E. White, *Capacity fade mechanisms and side reaction in Lithium-ion batteries.* Journal of the Electrochemical Society, 1998. **145**(10): p. 21.

12. Mizushima, K., et al., *Li/sub x/CoO/sub 2/ (0<x?1): a new cathode material for batteries of high energy density.* Solid State Ionics, 1981. **3-4**: p. 4.

13. *Handbook of Battery Materials*, ed. J. Besenhard. 1999, Weinheim: Wiley-VCH.

14. Avery, N. and K. Black, *Kinetic Analysis of capacity fade in lithium/coke half-cells.* Journal of Power Sources, 1997. **68**: p. 4.

15. Premanand, R., et al., *Studies on Capacity Fade of Spinel-Based Li-Ion Batteries.* Journal of the Electrochemical Society, 2002. **149**(1): p. 7.

16. Downing, R.G. and G.P. Lamaze, *Near-surface profiling of semiconductor materials using neutron depth profiling.* Semiconductor Science and Technology, 1995. **10**: p. 1423-1431.

17. Downing, R.G., *NDP Reactions of Interests*. 2008: Gaithersburg, Maryland.

18. Shultis, J.K. and R.E. Faw, *Radiation Shielding*. 2000, La Grange Park, Illinois: American Nuclear Society.

19. Williams, W.S.C., *Nuclear and Particle Physics*. 1991, Oxford Science: New York.

20. Ziegler, J.F., *Ion Implantation Science and Technology*. Second ed. 1988, San Diego: Academic Press Inc.

21. Bichsel, H., D.E. Groom, and S.R. Klein, *Passage of Particles Through Matter*. 2006, University of Washington. p. 34.

22. Ziegler, J.F., J.P. Biersack, and U. Littmark, *The Stopping and Range of Ions in Solids*. 2003, New York: Pergamon Press.

23. Ziegler, J.F., J.P. Biersack, and U. Littmark, *The Stopping and Range of Ions in Matter*. 1985, Pergamon: New York, New York.

24. Vlack, L.H.V., *Elements of Materials Science and Engineering*. Sixth ed. 1989: Addison-Wesley.

25. Whitney, S.M., *Light-Element Neutron Depth Profiling*, in *Mechanical Engineering*. 2006, The University of Texas at Austin: Austin, TX.

26. *Hyperphysics*. [cited; Available from: www.hyperphysics.com.

27. Smith, R.J., *Circuits, Devices and Systems*. Fourth ed. 1984: John Wiley and Sons.

28. Manthiram, A., *Battery Applications*. 2007, The University of Texas at Austin: Austin, Texas. p. 13.

29. Pistoia, G., *Lithium Batteries: New Materials, Developments and Perspectives*, ed. G. Pistoia. 1994, Amsterdam: Elsevier.

30. Choi, S., *Soft Chemistry Synthesis and Structure-Property Relationships of Lithium-Ion Battery Cathodes*, in *Mechanical Engineering* 2001, The University of Texas at Austin: Austin, TX.

31. Manthiram, A., *Lithium Ion Batteries*. 2007, The University of Texas at Austin: Austin, TX.

32. Thackeray, M.M., et al., *Lithium insertion into manganese spinels.* Materials Research Bulletin, 1983. **18**(4): p. 12.

33. Linden, D., *Handbook of Batteries*. 2nd ed. 1995, New York, New York: McGraw-Hill.

34. Nazri, G.A. and G. Pistoia, *Lithium Batteries: Science and Technology*. 2004, Dordrecht, Netherlands: Kluwer Academic Publishers.

35. Peled, E., *The Electrochemical behavior of alkali and alkaline earth metals in nonaqueous battery systems- The Solid Electrolyte Interphase Model.* Journal of the Electrochemical Society, 1979. **126**(12).

36. Leroy, S., et al., *Surface film formation on a graphite electrode in Li-Ion batteries: AFM and XPS study.* Surface and Interface Analysis, 2005. **37**: p. 8.

37. Aurbach, D., et al., Journal of Physical Chemistry B, 1997. **101**.

38. Aurbach, D., et al., Electrochimical Acta, 1999. **45**.

39. Unlu, K. and B.W. Wehring, *Neutron Depth profiling at the University of Texas.* Nuclear instruments and Methods in Physics Research A, 1994. **353**: p. 402-405.

40. Adib, M., et al., *Neutron Transmission of Single-Crystal Sapphire Crystals.* Czechoslovak Journal of Physics, 2005. **55**(5).

41. Zhang, S.S., K. Xu, and T.R. Jow, *Study of the charging process of a LiCoO/sub 2/ -based Li-ion battery.* Journal of Power Sources, 2006. **160**: p. 5.

42. Savitzky, A. and M. Golay, *Smoothing and Differentiation of Data by Simplified Least Squares Procedures.* Analytical Chemistry, 1964. **36**(8): p. 12.

43. Welsh, J.F., *The Development and Evaluation of Recoil-Nucleus Time-of-Flight Neutron Depth Profiling*, in *Chemistry*. 1996, Texas A&M University: College Station, TX.

44. Ortec, E.G., *Optimizing Noise and Energy Resolution of SSB Detectors*. 2007. p. 5.

45. Bohr, N., in *Phil. Magazine*. 1915. p. 581.

46. Bohr, N., in *Mat. Fys. Medd.* 1948. p. 8.

47. Maki, J.T., R.F. Fleming, and D.H. Vincent, *Deconvolution of Neutron Depth Profiling Spectra.* Nuclear instruments and Methods in Physics Research, 1986. **B17**: p. 147-155.

48. Biegalski, S.R., *Quality Assurance and Quality Control in the Elemental Analysis of Airborne Partilces*, in *Elemental Analysis of Airborne Particles*, S. Landsberger and M. Creatchman, Editors. 1999, Gordon and Breach Science Publishers.

49. Probion. *SIMS*. 2008 [cited; Available from: http://www.probion.fr/depth_resolution.php.

50. Galobardes, F., C. Wang, and M. Madou, *Investigation on the solid electrolyte interface formed on pyrolyzed photoresist carbon anodes for C-MEMS lithium ion batteries.* Diamond & Related Materials, 2006. **15**.

51. Yoshida, H., et al., *Capacity Loss Mechanism of Space Lithium-Ion cells and its Life Estimation Method.* Electrochemistry, 2003. **71**(12): p. 6.

52. Blyr, A., et al., Journal of the Electrochemical Society, 1998. **145**.

53. Tsunekawa, H., et al., Journal of the Electrochemical Society, 2002. **149**.

54. Wohlfahrt-Mehrens, M., C. Vogler, and J. Garche, Journal of Power Sources, 2004. **127**.

55. Wentao, L. and B. Lucht, *Inhibition of solid electrolyte interface formation on cathode particles for lithium-ion batteries.* Journal of Power Sources, 2007. **168**: p. 6.

56. Fu, L.J., *Surface Modifications of electrode materials for lithium ion batteries.* Solid State Sciences, 2006. **8**: p. 15.

57. Spotnitz, R., *Simulation of capacity fade in lithium-ion batteries.* Journal of Power Sources, 2003. **113**: p. 9.

58. Yan, L., H. Yang, and L. Qing-guo, *Influence of discharge rate on cycling performance of lithium-ion battery.* Chinese Journal of Power Sources, 2006. **30**(6): p. 3.

59. Sikha, G., et al., *Comparison of the capacity fade of Sony US 18650 cells charged with different protocols.* Journal of Power Sources, 2003. **122**: p. 11.

60. Belharouak, I., et al., *Li(Ni/sub 1/3/Co/sub 1/3/Mn/sub 1/3/O/sub 2/ as a suitable cathode for high power applications.* Journal of Power Sources, 2003. **123**: p. 6.

Vita

Scott Michael Whitney was born on September 24, 1982 in Pensacola, Florida. Scott is married to Crystal, a chemist who is also involved with nuclear research. He is the son of proud parents Daniel and Carol June Whitney. Scott spent the majority of his childhood playing various sports and pursuing different interests that included astronomy, physics, and even journalism. When he and his family moved to San Antonio, Scott attended Samuel Clemens High School where he was fortunate to have a few influential classes such as astronomy and physics that helped to shape his aspirations for college.

Scott entered the Physics undergraduate program at The University of Texas at Austin in 2000. Additionally, he was also accepted into the Emerging Scholars Program for Mathematics. This was a selective program designed to go beyond the typical math skills taught at the undergraduate level. Scott successfully completed the program and continued throughout the rest of his undergraduate career while always staying at the top of his class in the physics program. He received University Honor's and Dean's List awards for every semester of his undergraduate schooling. He also had the opportunity to participate in a 2003 summer research program for Dr. Heinzen of the UT physics department in Atomic and Molecular Physics. Other undergraduate research that Scott participated in includes a non-linear dynamics physics research program at Peking University in Beijing, China in the winter of 2003. It was after returning from this research that he began research for Dr. Biegalski in the nuclear program and the Mechanical Engineering department at UT.

Scott entered the graduate program of the UT Mechanical Engineering department in January of 2005 after graduating with High Honors from the undergraduate physics program. Upon entering the program, Scott was selected as a recipient of the Thrust 2000 fellowship from the UT engineering department. He was also later selected to receive the 2005 American Nuclear Society engineering scholarship.

Scott dedicated his Master's research to the assembly and advancement of a Neutron Depth Profiling facility on beam port 2 of the TRIGA research reactor at UT. During this time he also assisted in the design for a fast neutron Prompt-Gamma Activation Analysis facility for beam port 4 of the reactor. He also attended a selective course at Lawrence Livermore National Lab on non-proliferation and national security.

During his Master’s and Doctoral studies Scott is thankful to have been supported by the DOE INIE program.

Permanent Address

11805 Argonne Forest Trl. #B

Austin, TX 78759

This dissertation was typed by the author.